THE EFFECTS OF PORE CONNECTIVITY ON THE PERMEABILITY OF COQUINAS (CARBONATE ROCKS) FROM THE MORRO DO CHAVES FORMATION, SERGIPE-ALAGOAS BASIN, BRAZIL

Maira da Costa de Oliveira Lima Santo

Tese de Doutorado apresentada ao Programa de Pós-graduação em Engenharia Civil, COPPE, da Universidade Federal do Rio de Janeiro, como parte dos requisitos necessários à obtenção do título de Doutor em Engenharia Civil.

Orientadores: Paulo Couto

Leonardo Fonseca Borghi de Almeida

Amir Raoof

Rio de Janeiro

Novembro de 2020

THE EFFECTS OF PORE CONNECTIVITY ON THE PERMEABILITY OF COQUINAS (CARBONATE ROCKS) FROM THE MORRO DO CHAVES FORMATION, SERGIPE-ALAGOAS BASIN, BRAZIL

Maira da Costa de Oliveira Lima Santo

TESE SUBMETIDA AO CORPO DOCENTE DO INSTITUTO ALBERTO LUIZ COIMBRA DE PÓS-GRADUAÇÃO E PESQUISA DE ENGENHARIA DA UNIVERSIDADE FEDERAL DO RIO DE JANEIRO COMO PARTE DOS REQUISITOS NECESSÁRIOS PARA A OBTENÇÃO DO GRAU DE DOUTOR EM CIÊNCIAS EM ENGENHARIA CIVIL.

Orientadores: Paulo Couto
Leonardo Fonseca Borghi de Almeida
Amir Raoof

Aprovada por: Prof. José Luis Drummond Alves
Dr. Elizabeth May Braga Dulley Pontedeiro
Prof. Rodrigo Bagueira de Vasconcellos Azeredo
Prof. Martinus Theodorus van Genuchten

RIO DE JANEIRO, RJ-BRASIL
NOVEMBRO DE 2020

Santo, Maira da Costa de Oliveira Lima

The effects of pore connectivity on the permeability of coquinas (carbonate rocks) from the Morro do Chaves Formation, Sergipe-Alagoas Basin, Brazil / Maira da Costa de Oliveira Lima Santo. – Rio de Janeiro: UFRJ/COPPE, 2020.

XIX, 154: il.; 29,7 cm.

Orientador(es): Paulo Couto

Leonardo Fonseca Borghi de Almeida

Amir Raoof

Tese (doutorado) – UFRJ/ COPPE/ Programa de Engenharia Civil, 2020.

Referências Bibliográficas: p. 140-154.

1. Conectividade. 2. Permeabilidade. 3. Coquinas. 4. RMN. 5. Microtomografia raio-X. I. Couto, Paulo *et al*. II. Universidade Federal do Rio de Janeiro, COPPE, Programa de Engenharia Civil. III. Título.

I dedicate this work to my parents Cheila and Jair,

with love and gratitude,

to my husband Vlamir

who shares all my happy and sad moments,

and to my little daughter Clara,

my best part; the light of my life

“The period of greatest gain in knowledge and experience is the most difficult period in someone's life.”

– Dalai Lama

ACKNOWLEDGEMENTS

First of all, I would like to thank my advisors, Paulo Couto, Leonardo Borghi, and Amir Raoof. At the beginning of my PhD, Leonardo gave the opportunity to be part of the Pre-Sal project, and I had financial support to start my studies. After few months, I could join the Wagex project and became part the Modeling Group. Before starting my Ph.D, I already dreamed of studying more about modeling, but I would never imagine being part of a group on this subject. I feel fulfilled. Thank you very much, Paulo and Leonardo, for your friendship and support. Amir met me during my PhD studies, and guided me to the PNM world. I could learn a lot from your knowledge. Thanks to his guidance and friendship Thank you very much, Amir.

I would like to thank also my PhD committee. Thank you very much, Prof. José Drummond, for our great discussions during the project meetings, data analysis, and for your friendship. Thank you very much Prof. Rodrigo Bagueira, for your support since the beginning of my post-graduation. Once an advisor always an advisor.

I would like to thank Betty May and Rien, for been like my parents during the last two years. You helped with my studies, took my doubts, and supported me every time I needed. I will never forget all that you did for me. Your friendship was all the difference in my life. Thank you.

A special acknowledgment to Prof. Patrick Corbett, for the early discussions of my studies. Your support was the basis of my PhD research. Thanks for your ideas and fruitful discussions.

I would like to thank for Prof. Ricardo Tadeu, Alessandra, Olga, and Caio from LIN, for your help with the μCT acquisition.

My gratitude goes to the UFFLAR team: Prof. Rodrigo Bagueira, Afrânio, Michael and Pedro for helping me with the saturation and NMR experiments, and the great discussions. I also thank Prof. Giovanni Stael, Silvia Bermudez and Luis Jacobo from the National Observatory for their support with the experimental part.

A special acknowledgment also to Austin Boyd and Edmilson Rios for all their support during my research. Thanks for sharing your knowledge about petrophysics.

I would like to thank for Marcelo Mendes, Bruno Valle, Julia Favoreto, Helisson Santos, Lucas Rocha, Marcos Nunes, Aristides Orlandi and the entire LAGESED team.

My gratitude also goes to Dr. Frances Abbotts, and Jacyra Monteiro, from Shell, for all their support during my research. I would like to thank Shell for the financial support. Special acknowledgements to CNPq for their financial support.

These last years I was lucky to meet wonderful people: Tatiana Lipovetsky, Wiliam Godoy, Lorena Martins, Fernanda Hoerlle, Mateus Ramirez and Barbara Esteves. Without your friendship and help I could not have finished this stage of my life. No words to discribe how thankful I am to all.

I would like to thank Denise Nunes, Felipe Eller, Adriano Rocha, Carlos Jr., Thiago Saraiva, Thaís Silveira, Santiago Drexler, Carol Dias, Rivaldo, Rodrigo Bayão, Paulo Moreira, Natália Dias, and all LRAP team. Thank you for everything.

Finally, I must thank all of my family. My mother-in-law, father-in-law, sisters-in-law, brothers-in-law, nephew and niece, I have no words to thank you all for your support and love throughout these years. Most important in all this have been my husband, Vlamir, my daughter Clara and my parents, Cheila and Jair. Without your support and love, I could not have finished this journey. You have been with me since the beginning, sharing the good and the more difficult moments. And did put up with my bad humor, and at times even my tears. Thanks for everything, Family!

Resumo da Tese apresentada à COPPE/UFRJ como parte dos requisitos necessários para a obtenção do grau de Doutor em Ciências (D.Sc.).

OS EFEITOS DA CONECTIVIDADE DOS POROS NA PERMEABILIDADE EM COQUINAS (ROCHAS CARBONÁTICAS), DA FORMAÇÃO MORRO DO CHAVES, BACIA SERGIPE-ALAGOAS, BRASIL

Maira da Costa de Oliveira Lima Santo

Novembro/2020

Orientadores: Paulo Couto
Leonardo Fonseca Borghi de Almeida
Amir Raoof

Programa: Engenharia Civil

A heterogeneidade do sistema poroso de rochas carbonáticas se manifesta pela presença de diferentes tipos, tamanhos e formatos de poros resultantes de sedimentação e ações diagenéticas. Essas complexidades aumentam as incertezas na estimativa das propriedades hidráulicas, pois podem ocorrer diferentes valores de permeabilidade para amostras com porosidades semelhantes. Esta pesquisa utilizou amostras de coquinas extraídas de um testemunho contínuo de sondagem da Formação Morro do Chaves, sendo consideradas análogas a uma das fácies dos reservatórios carbonáticos do pré-sal brasileiro. Este estudo tem como objetivo melhorar predição de permeabilidade, otimizando as equações de estimativa de permeabilidade e analisando a influência da conectividade no fluxo do sistema poroso. Para isto, rock types foram desenvolvidos baseados na petrofísica de rotina. Diferentes técnicas petrofisicas e estatística foram utilizados para confirmar as similaridades entre amostras nos agrupamentos. O estudo de conectividade foi feito a partir de imagens microtomográficas de amostras com porosidade similar e diferentes permeabilidade. As imagens 3D mostraram que a interligação do sistema poroso favorece o escoamento, assim como tortuosidade e estreitamente das gargantas impactam o fluxo a nível da amostra. A permeabilidade das coquinas foram analisadas a partir dos modelos de Kenyon e Timur-Coates. As constantes dessas equações foram otimizadas usando regressão linear múltipla, com o objetivo de adequar essas equações.

Abstract of Thesis presented to COPPE/UFRJ as a partial fulfillment of the requirements for the degree of Doctor of Science (D.Sc.)

THE EFFECTS OF PORE CONNECTIVITY ON THE PERMEABILITY OF COQUINAS (CARBONATE ROCKS) FROM THE MORRO DO CHAVES FORMATION, SERGIPE-ALAGOAS BASIN, BRAZIL

Maira da Costa de Oliveira Lima Santo

November/2020

Advisor: Paulo Couto

Leonardo Fonseca Borghi de Almeida

Amir Raoof

Department: Civil Engineering

The heterogeneity of the pore structure of carbonate rocks is manifested by different types, sizes and shapes of pores resulting from sedimentation and diagenetic actions. These complexities increase uncertainties in the estimated hydraulic properties since different permeability values can occur for samples having similar porosities. Investigations were carried out using coquinas taken from a continuous core extracted from the Morro do Chaves Formation, which is considered an analogue of Brazilian pre-salt carbonate oil reservoirs. The aim was to improve permeability predictions and to analyze the influence of pore connectivity on fluid flow within the pore system. For this purpose, rock types were developed based on routine core analysis. Different petrophysical and statistical techniques were used to confirm similarities between the samples in the clusters. The connectivity study was carried out using microtomographic images of samples having similar porosities but different permeabilities. The 3D images showed that the interconnection of the pore system favored flow within the pores, with the tortuosity and narrowing of the pore throats also impacting the permeability of the pore system. Permeabilities of the coquinas were further analyzed using the Kenyon and Timur-Coates models. Multiple linear regression techniques were used to optimize the various constants in these equations.

CONTENTS

LIST OF FIGURES

LIST OF TABLES

LIST OF SYMBOLS AND ABBREVIATIONS

A	-	Cross-sectional area
C	-	Pore conductance
C_p	-	Capillary pressure
g	-	Gravity acceleration
g_{ij}	-	Conductance of the cylindrically shaped
h	-	Distance
i	-	Hydraulic gradient
k	-	Permeability
k_{abs}	-	Absolut permeability
k_{ef}	-	Effective permability
K_{Macro}	-	Permeability from macropores
K_{rel}	-	Relative permeability
K_{Sdr}	-	Kenyon permeability
K_{Tim}	-	Timur-Coates permeability
N_i	-	Coordination number of pore *i*
p	-	Pressure
p_{ij}	-	Pressure at pore body
P_c	-	Capillary pressure
PC1	-	Principal components 1
PC2	-	Principal components 2
PC3	-	Principal components 3
Q	-	Volumetric flow rate
Q_{ij}	-	Volumetric flow rate inside the pore throat
Q_{ij}^{n}	-	Non-wetting fluid volumetric flow rate between pores *i* and *j*
Q_{ij}^{w}	-	Wetting fluid volumetric flow rate between pores *i* and *j*
Q_{tot}	-	Total volumetric flow rate throughout the pore network
R_t	-	Radius of the pore throats
R1	-	Radius of curvature used in the Young-Laplace equation
R2	-	Radius of curvature used in the Young-Laplace equation
R_{ij}	-	Radius of the pore throat which connects pores *i* and *j*

R_s	-	Resistance force against fluid flow within the pore in the *s* direction
S	-	Surface
s_i^α	-	Saturation of phase α in the body *i*
S_{wi}	-	Irreducible saturation
t	-	Time
T_1	-	Longitudinal relaxation time
$T_{1Logmean}$	-	Longitudinal relaxation time mean
T_2	-	Transverse relaxation time
$T_{2Logmean}$	-	Transverse relaxation time mean
T_{2D}	-	Diffusional relaxation
Ts	-	Bulk volume relaxation
v	-	Velocity vector
V	-	Volume
V_g	-	Grains volume
V_p	-	Pore volume
V_f	-	Total volume of the liquid phase
$\overline{v}$	-	Average velocity of a fluid in the pore

GREEK SYMBOLS

η	-	Dynamic viscosity of fluid
θ	-	Contact angle
ϑ	-	Linear attenuation coefficient
λ_1, λ_2	-	Parameters associated to the *F* generating function
μ	-	Dynamic viscosity of fluid
ρ	-	Density of fluid
ρ_1	-	Superficial relaxitvity
τ	-	Tortuosity
ϕ	-	Porosity

ABBREVIATIONS

ANP	-	Agência Nacional do Petróleo
BVI	-	Bound volume irreducible
CPMG	-	Carr-Purcell-Meiboom-Gil
FID	-	Free Induction Decay
FFI	-	Free Fluid Index
KCL	-	Potassium Chloride
MICP	-	Mercury Pressure Capillry Pressure
MicroCT	-	X-ray Microtomography
MLR	-	Multiple Linear Regression
PCA	-	Principal Components Analysis
PNM	-	Pore-Network Modelling
RT	-	Rock Type
NMR	-	Nuclear Magnetic Resonance
ROI	-	Region of Interest
SE	-	Southeast
SI	-	International System of Units

1 INTRODUCTION

1.1 Context

Studies of oil and gas exploration involve many scientific disciplines, including the geology of oil reservoirs, paleontology, stratigraphy, sedimentology, petrophysics, geochemistry and geophysics, as well as mechanical, electrical, drilling and production engineering (Triggia et al., 2001). In terms of the oil production process, petrophysics is the science that studies the physical, electrical, and mechanical properties of rocks and fluids (Chen and Pagan, 2013), with a primary aim being to increase oil recovery. Within this context, the petrophysics of carbonate rocks has received much interest since the discovery of the pre-salt oil-bearing reservoirs by Petrobras in 2007. Rocks of these reservoirs were formed by lake shales rich in organic matter and deposited in low blocks from failures during rifting some 131 to 120 million years ago (Chang et al., 2008; Estrella et al., 2008). The pre-salt is composed of the Campos and Santos basins, with the reservoirs consisting of three main types of rocks: limestones with coquinas (Chang et al, 2008), microbialitic limestones in the upper portion of the rift, which were produced and accumulated in lakes connected to the oceans (Riccomini et al., 2012, Estrella et al., 2008; Doborek, 2012), and fractured volcanic rocks in the lower portion of the rift (Chang et al., 2008).

Studies in petroleum geology are often carried out using exposed (outcropped) near-surface rocks, referred to as analogues. They are very similar to the subsurface rocks and offer the main characteristics of reservoirs in the subsurface. This allows one to determine many physical parameters, such as the geometric shapes of rock bodies, and their porosity and permeability among other petrophysical parameters. These parameters can be compared with information obtained from drilled samples or logging. Also, even with samples from the pre-salt formations, several difficulties may arise regarding laboratory studies. For example, the waiting time for the formal release of such samples is sometimes relatively long, while it is often challenging to carry out specific analyses with the pre-salt samples because of their fragile nature. This favors the use of analogues in petrophysical studies.

This research used coquinas as one type of rock analogues to those existing in the pre-salt oil reservoirs. Coquinas are known to be hybrid carbonate rocks in that they are formed not exclusively by shells and/or fragments, but also contain significant amounts

of siliciclastic material (Tavares, 2004). Such rocks typically have a complex pore system, with pores ranging from micropores to larger vugs, thus making it difficult to estimate specific petrophysical properties such as permeability.

1.2 Objectives

This work uses different petrophysical techniques, both basic and advanced, to better understand coquina samples contained in a particular core (02-SMC-2-AL) from the Morro do Chaves Formation in the Sergipe-Alagoas Basin in north-east Brazil. While rocks of this type pose a challenge due to the complex composition and heterogeneity of their pore system, understanding their petrophysical properties is of great value for improving oil exploration of the Brazilian pre-salt.

The main objective of this study is to predict the permeability of coquina samples by improving predictive equations found in current literature and, to understand how the pores connectivity influences this prediction. To carry out this research, several secondary objectives were necessary:

I) to improve rock typing using data from routine core analyses (notably porosity and permeability) using similarity confirmation responses from transversal relaxation times (T_2) obtained with nuclear magnetic resonance (NMR) relaxometry;

II) to correlate pore size distributions obtained using NMR with pore radii derived using mercury injection capillary pressure (MICP) techniques. The correlations will be used to calibrate pore segmentations in digitized X-ray microtomography images;

III) to statistically analyze the results obtained using pore-scale models of the pore system, and to understand how and why samples having the same porosity can show significant differences in their permeability;

IV) to understand how the pore size distribution of different rock types influences fluid flow in the samples. For this, principal component analysis (PCA) techniques are used to facilitate visualization of the main patterns and to highlight differences and similarities of the different properties.

V) To accomplished the above objectives using a series of experimental and computational studies, notably routine core analyses, NMR, MICP,

centrifugation to determine irreducible saturation, X-ray microtomography, pore network modeling, thin sections, diffraction X-ray, and statistical analysis of the results. Results should improve our ability to evaluate the permeability of coquinas, which will facilitate better descriptions and exploration of Brazilian pre-salt oil reservoirs.

1.3 Methodology

Aiming to achieve the main objectives of this research, a workflow was elaborated (Fig. 1) to optimize available time and available resources, and organize expected results.

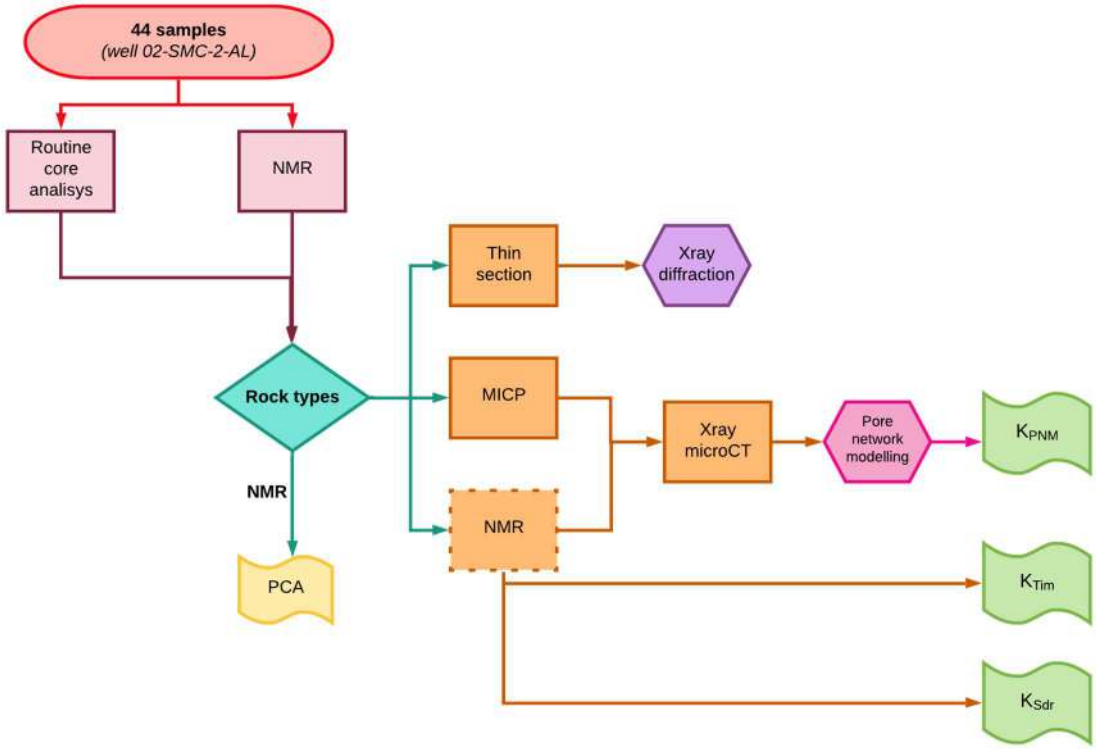

Figure 1-1. Research workflow to predict the permeability from rock types

As can be seen in Figure 1.1, we used in this study 44 samples of coquinas taken from core 02-SMC-2-AL belonging to the Morro do Chaves. After their selection, routine core analyses were performed. The routine results were used to separate the samples into clusters (rock types) by permeability range so as to understand the differences among the petrophysical characteristics of these rocks. With the rock types defined, the next step was to confirm similarities of the samples within their group by using NMR data. Thin section and X-ray diffraction analyses were used to understand why the curves of certain samples had different shapes.

Information from estimated pore radii is essential to understand fluid flow in the porous medium. For this purpose, some samples were selected with similar porosities but different permeabilities. MICP techniques were then used to determine radii of the pore throats. This made it possible to observe the effects of pore throats on flow among different rock types and differences among samples within the same group. Based on MICP data, permeabilities were estimated with the Winland equation (1980), known as R_{35}, using linear regression to determine the required coefficients.

Based on the optimization of the NMR and MICP curves, it was possible to transform T_2 values from NMR signals into pore radii, thus facilitating the calibration of the pore segmentation of microCT images. The starting point to quantify the pore systems of samples is the skeletonization of the pore space, such that the pore bodies and connected pore throats are defined. Results of the pore throats and pore bodies are then statically analyzed, as well as the coordination number of the pore bodies, thus describing the connections within the samples. Permeabilities are then estimated by modeling of the pore systems using numerical simulations with a pore network model (PNM).

The permeability can be estimated also using NMR, which is the only technique suitable for such measurements during logging. Several equations from the literature are used by the oil industry for this purpose. In this research, two equations were tested: the Kenyon (K_{Sdr}) and Timur-Coates (K_{Tim}) equations. For this several parameters are required: some are obtained directly from the NMR experiments (such as $T_{2Logmean}$ in the K_{Sdr} equation), while others require additional information, such as the value of irreducible saturation (S_{wi}) to define an essential parameter (effective saturation) in the equation for K_{Tim}.

Analyzing the influence of pore size within the developed clusters is one of the objectives of this research. This analysis was done using multivariate statistics. Principal component analyses (PCA) were used to demonstrate how pore size and other attributes are more or less relevant within each rock type. These studies also used results from the NMR and MICP experiments.

1.4 Thesis Organization

Chapter 2 presents a bibliographic review of the main topics studied in this research. Characterizations of the Sergipe Alagoas basin, of which the Morro do Chaves formation is part, and the coquinas are explained to provide a geological context of the samples used

in this work. Part of this chapter is intended to define the concepts of the petrophysical parameters, as well as the experimental techniques that were used.

Chapter 3 describes the rock samples that were used, as well as of all of the laboratory methods and measurements for each experimental step. This information is considered of special relevance to the development of this work.

Chapter 4 presents the result of the various steps indicated in the workflow as described in Section 1.3, together with analyses and discussions relevant to the study.

Chapter 5 presents the conclusions of the research, as well as suggestions for future work.

Finally, bibliographical references are presented in chapter 6.

2 THEORETICAL FRAMEWORK

This chapter presents an overview of the main concepts used in the research. The concepts regarding the geology of the samples are presented first, including the structural geology and stratigraphy of the Morro do Chaves Formation, as well as the characterization of coquinas. This is followed by a discussion of the petrophysical properties, such as porosity and permeability, and the macroscopic characterization of rock types. Concluding the chapter are the various experimental techniques used for the research, such as nuclear magnetic resonance (NMR), mercury intrusion capillary pressure (MICP) measurements, porous media modelling, and a review of multivariate statistics such as principle component analysis (PCA).

2.1 Geological Setting

It is necessary to first present a theoretical basis of the main terms discussed in the present work.

2.1.1 Sergipe-Alagoas Basin

The Sergipe-Alagoas Basin is located in northeastern of Brazil. The basin comprises a narrow strip between 20 and 50 km wide and 350 km long, with a 45° NE orientation extending from 9° to 11°30' south latitude and 35°30' to 37° 00' west longitude (Figure 2.1). The basin occupies an area of approximately 32,760 km², covering parts of Sergipe and Alagoas states, as well as a small portion of Pernambuco, with one-third emerging and two-thirds being submerged up to a 3,000 m isobath (ANP, 2009). The Sergipe-Alagoas basin is bounded to the north by Maragogi High, and to the south by the Vaza-Barris Fault System, which separate the Sergipe-Alagoas basin from the Pernambuco-Paraíba and Jacuípe basins.

Figure 2-1. Location of the Sergipe-Alagoas basin in northeastern Brazil (modified from AZAMBUJA *et al*., 1998).

The Sergipe and Alagoas basins differ in terms of their structural and stratigraphic characteristics (FEIJÓ, 1994) (Figures 2.2 and 2.3). The western side, with its Precambrian crystalline basement, is marked by distensional fault systems and associated structures. The internal boundary between the sub-basins is given by Japoatã-Penedo High, along the São Francisco River. However, CAMPOS NETO *et al*. (2007) considered elevation only as a divider of the emerged part, encompassing the shallow water parts, with no continuity below the Eo-alagoas hinge line block as geological evidence in deep waters is lacking.

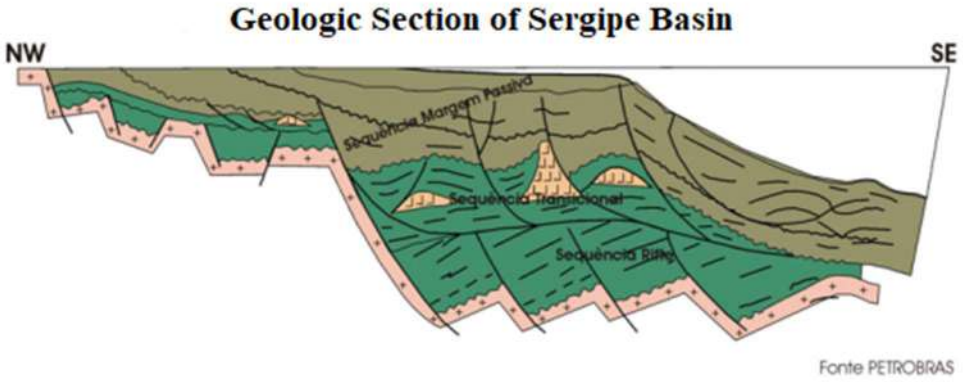

Figure 2-2. Geological section from the Sergipe basin (from Petrobras)

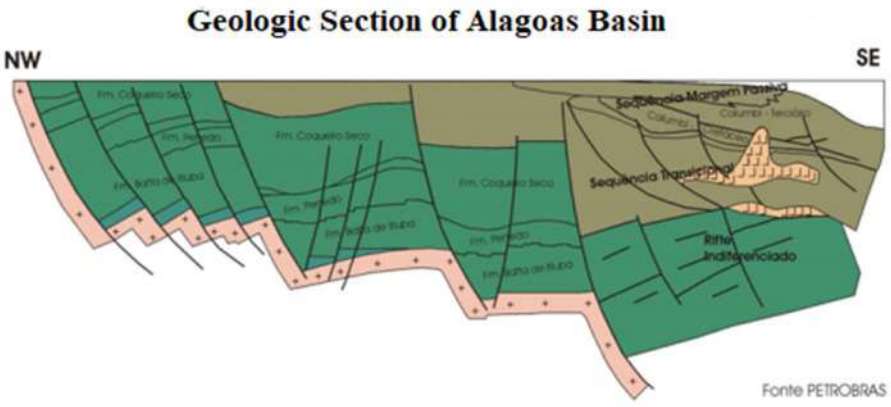

Figure 2-3. Geological section from the Alagoas basin (from Petrobras)

2.1.2 Structural Framework and Tectonic Evolution

The Sergipe-Alagoas basin is located along the eastern Brazilian continental margin. Its sedimentary deposits reflect the various tectonic phases caused by the breakup of Western Gondwana. Its origin is explained by models of continental drift, tectonic plates, and the formation and expansion of the ocean floor (CAINELLI & MORIAK, 1999; MORIAK, 2003; MORIAK, 2012; ASMUS, 1982; CHANG *et al*., 1990). These models explain the separation of the South American and African plates, the formation of the Atlantic Ocean, and the construction of continental margins. They developed during three main crustal phases: crustal uplift, fracturing, and tension separation (ASMUS, 1982). The Sergipe-Alagoas basin is subdivided into four tectonic compartments separated by large faults, and differentiated by their depths: basement surface, sedimentary cover nature, faulting intensity, and gravimetric anomaly patterns.

SZATMARI & MILANI (1999) considered that, at early Eo-cretaceous, Africa was subject to a counterclockwise rotation relative to South America during continental separation, which induced a rotation of the Sergipana microplate. However, due to a divergent transcurrent failure pattern (NE-SO oriented) along the eastern part of the microplate, that movement was slow, thereby generating N-S orientation hemigrabens in echelon. During this evolution, on the north side of the microplate, a positive pop-up structure developed, causing uplift and erosion. At Late Eo-cretaceous, between the Aptian and Albian ages, these transient faults were reactivated. Normal faults with hinge lines towards the basin developed to define the newly created continental margin. A SE directional movement occurred of the microplate at the end of the rift phase due to the

action of the Vaza-Barris sinister fault. During the Albian, there was a definitive separation of the plates and drift of the continents, thereby initiating a thermal subsidence of the drift phase, associated with sedimentary overload and salt tectonics (halokinetic movements).

2.1.3 Stratigraphy

The Sergipe-Alagoas basin exhibits the most complete sedimentary succession of all basins located along the eastern Brazilian coast. Its sedimentary record shows five different tectonic-stratigraphic phases: Paleozoic, the Pre-Rift phase, the Rift phase, the Post-Rift phase, and the Drift phase. However, since both sedimentary filling and the tectonic style of the basin vary from Sergipe to Alagoas, two stratigraphic charts could be constructed as shown in Figures 2.4 and 2.5 (CAMPOS NETO *et al*., 2007).

According to CAMPOS NETO *et al*. (2007), the tectonic-stratigraphic phases correspond to five supersequences in the basin:

- The first supersequence corresponds to the Paleozoic phase represented by the Igreja Nova Group, which encompasses the Batinga (sub-aqueous glacial environment) and Aracaré formations (coastal environment, desert and delta) (Permo-Carboniferous age);
- The second supersequence corresponds to a Pre-Rift Jurrasic phase and encompasses the Candeeiro (fluvio-deltaic sandstones), Bananeiras (shallow lake systems) and Serraria formations (sandstones reworked by eolic river systems) (Early Jurassic age);
- The third supersequence corresponds to the Rift phase and encompasses the Feliz Deserto (lake-deltaic system), Rio Pitanga (fanglomerates deposits), Penedo (anastomosed river system), Barra de Itiúba (fine delta-lacustrine sandstones and shales), Coqueiro Seco (alluvial-delta system), Morro do Chaves (coquinas), and Maceió (sandstones, shales evaporites and calcirudites from alluvial-deltatic fans and sabkha environment) formations (Neocomian to Early Aptian age);
- The fourth supersequence corresponds to the Post-Rift phase and encompasses the Muribeca Formation, including the Carmópolis (alluvial-deltaic sandstones), Ibura (microbial carbonates, evaporites and shales) and Oiteirinhos (shales and calcilutites) members (Neo-Alagoas age);

- The fifth supersequence corresponds to the Drift phase characterized by the deposition of a carbonate platform represented by the transgressive Riachuelo formation (Albian age). Above this formation, a carbonate ramp was deposited, formed by fine-grained sediments represented by the Contiguiba Formation (Neocenomanian-Coniacian time). At Late Coniacian, there was a drop in sea level, leading to the deposition of siliciclastic of the Calumbi and Marituba formations and bioclastic calcarenites of the Mosquiteiro Formation. In the Pliocene, a regressive event related to the global eustatic fall caused the deposition of coastal sediments from the Barreiras Formation.

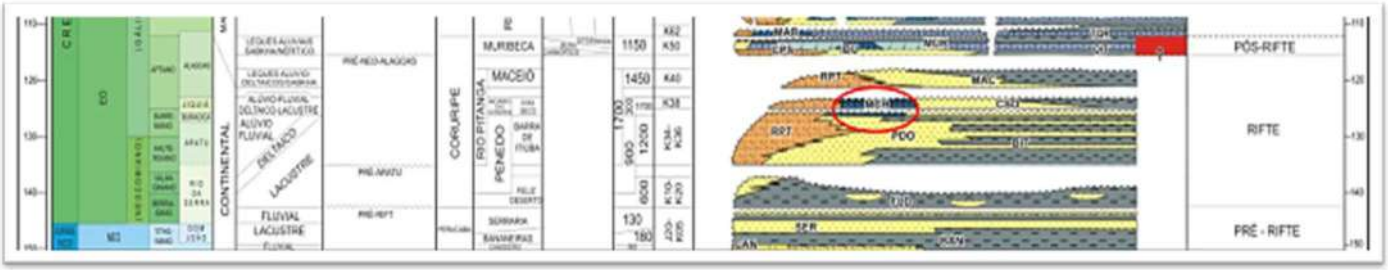

Figure 2-4. Stratigraphic chart of the Sergipe sub-basin, highlighting the Morro do Chaves Formation (CAMPOS NETO et al., 2007)

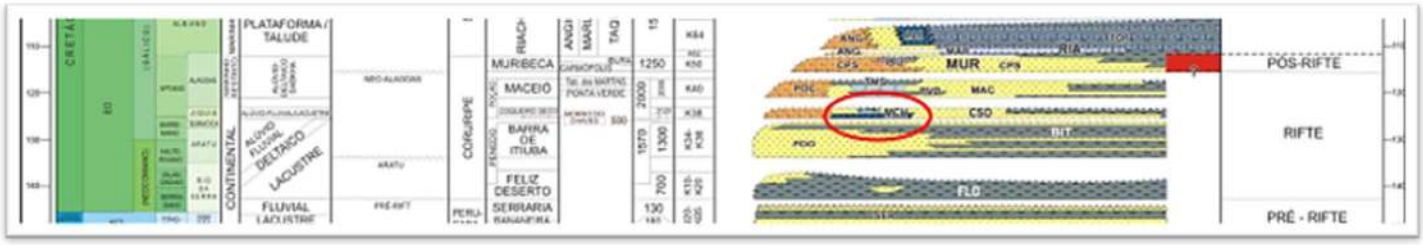

Figure 2-5. Stratigraphic chart of the Alagoas sub-basin, highlighting the Morro do Chaves Formation (CAMPOS NETO et al., 2007)

2.1.4 The Morro do Chaves Formation

According to AZAMBUJA *et al*. (1998), the Morro do Chaves Formation is defined as a carbonate succession (Jiquié age), having a thickness that varies between 50 and 350 m. The formation was formed by the accumulation of coquinas (shells of bivalve mollusks and shales from lacustrine environments, interspersed with siliciclastic rocks from the Coqueiro Seco and Rio Pitanga formations. The formation is composed of fan-deltas facies associated with the fault edge to the northeast of the basin, presenting

conglomerates reworked by waves, sandstones interspersed with bivalves, of thick layers of coquinas, and lake shales (Figure 2.6).

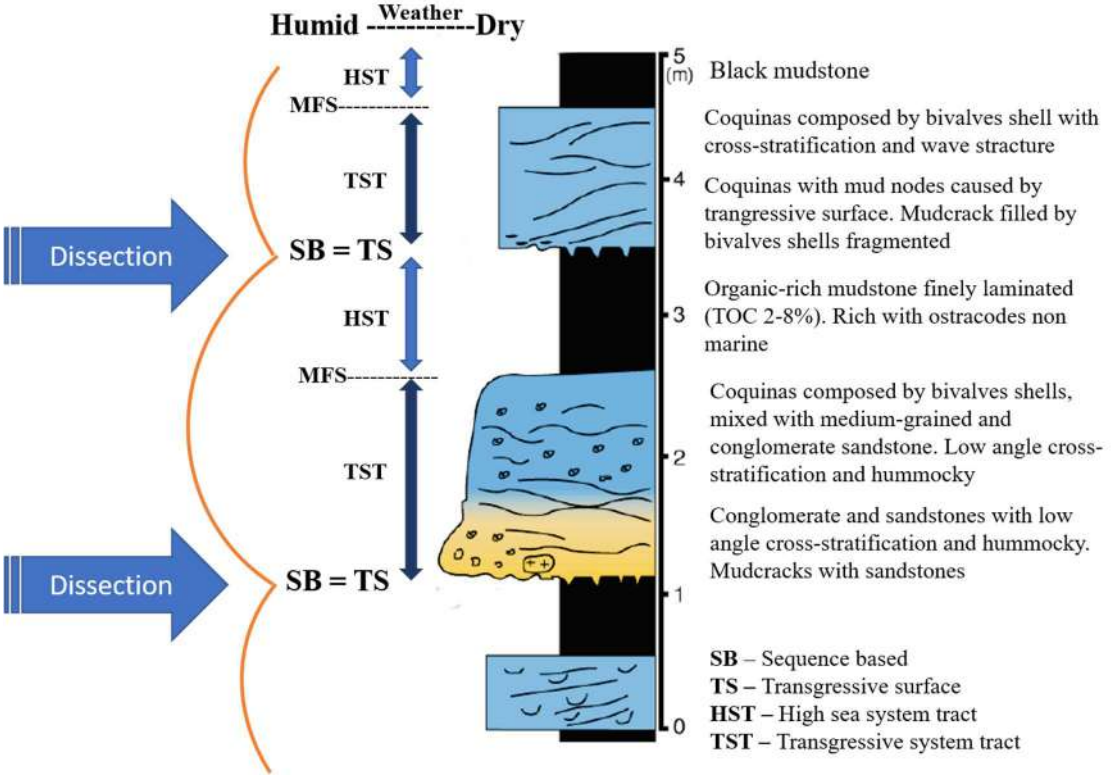

Figure 2-6. Facies model from the Morro do Chaves Formation (modified from AZAMBUJA et al., 1998)

The Morro do Chaves Formation represents a transgressive third-order system covering siliciclastic fluvial deposits from the Penedo Formation. Basement contact is a transgressive surface as well as a sequence boundary. The upper contact of the Coqueiro Seco Formation is gradual by showing a progressive entrance of terrigenous sediments into the basin, with the establishment of fluvio-deltaic and alluvial systems (AZAMBUJA *et al.*, 1998).

The unit suffered from strong tectonic and climatic controls, being marked by a lake carbonate sequence developed on high structures. Deposition occurred in smaller cycles due to variations between humid and arid climates. According to the paleoenvironment, sedimentation strongly varied involving alluvial fans and lakes, and with bars composed of coquinas and shales, with grading towards the depocenter.

The Morro do Chaves Formation is composed of bivalve coquinas of *Anodontophora sp., Gonodon sp., Psammobia sp., Nucula sp.* and *Astarte sp*. (BORGES, 1937; OLIVEIRA, 1937), and small gastropods. The bivalves developed in shallow and oxygenated waters. After their death, due to strong storms, the shells were reworked and

accumulated like bars, washed over fans and beaches, and were transported to the coastline. According to RIGUETI *et al*. (2020), the facies of the Morro do Chaves formation indicate low gradient deposition and a high energy coastline. This is supported by the predominance of coastal sediments as influenced by storms (Fig. 2.7). Shales were generated in shallow waterbodies, restricted by high blocks faults. There was then an abundance of organic matter contained in fish fragments belonging to *Lepidontes* and *Mawsonia,* typical of lake environments, and non-marine ostracodes such as the *Cyprididae* family, common in continental underwater environments (SOUZA-LIMA *et al*., 2002; MAFFIZZONI, 2000).

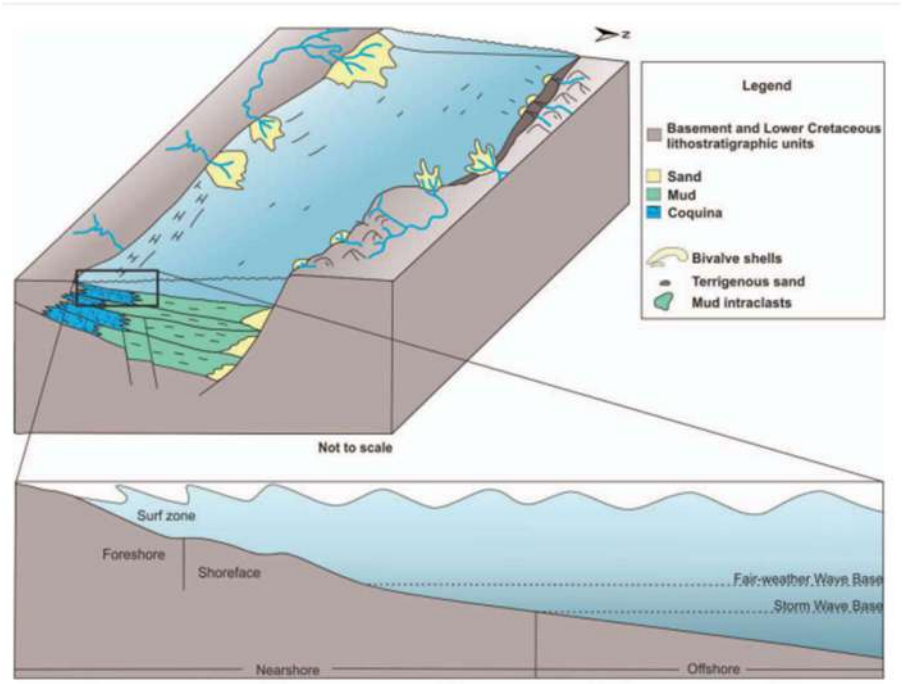

Figure 2-7. Block diagram representing the presumed depositional setting of the Morro do Chaves Formation and the distribution of sedimentary facies along the hydrodynamic zones of a storm-wave-dominated platform, with an onshore-offshore energy gradient (RIGUETI et al., 2020)

2.1.5 Coquinas

Several investigations focused on the taphonomy of coquinas. For example, PETTIJOHN (1957) considered coquinas to be carbonate rocks consisting of fossil fragments (totally or partially) that were transported and then subjected to mechanical stress. However, SCHÄFER (1972) characterized coquinas as a concentration of shells and/or fragments exclusively, deposited by the action of a transport agent. Both studies suggested that the composition, stratum geometry and distribution of coquinas is governed by the laws of sedimentation, instead of biological laws. The views of

SCHÄFER (1972) were supported by TAVARES (2014) who noted that data from the same formation indicated that coquinas formed only from whole and fragmented shells. This point of view is reinforced due to the presence of siliciclastic material in the layers, reaching values of about 50% of the siliciclastic matrix.

Coquina layers appear in geological records in sizes of in centimeters to meters, associated with and/or carbonate deposits. Their main depositional environments are paralic, lakes, estuaries, beaches, and sloughs, but can also occur in a marine platform environment (neritic) as a result of the action of waves and tidal currents, in addition to waves and currents caused by storms. In the case of coquinas from lacustrine environments, they are formed preferentially by the action of currents and storm waves (CASTRO, 1988; TEIXEIRA, 2012).

CASTRO (1988) and TEIXEIRA (2012) suggested that coquinas layers formed by such factors as:

- high production of bioclasts, resulting from a stressed environment, with variations in temperature, salinity, water energy and turbidity; mass mortality, which may have been influenced by volcanism and water bloom (i.e., the withdrawal of oxygen and nutrients caused by the rapid reproduction of plankton, resulting in the release of toxic waste in the water), in addition to earthquakes and tidal waves;
- low input of terrestrial sediments, thus allowing the colonization and accumulation of bioclasts at the substrate;
- hydraulic selection by preferentially transporting shells of greater granulometry (gravel above 2 mm), together with sand and mud;
- diagenetic effects, which relate shell concentrations to such processes as compaction, cementation, micritization, substitution, neomorphism and dissolution. These processes influence concentrations of carbonate layers, being dependent upon temperature, pressure, pH and Eh.

According to TEIXEIRA (2012), large accumulations of shells are not necessarily associated with large populations of organisms, since bivalve shells are highly resistant to transport and can be preserved in large quantities.

2.2 Porosity

In petrophysical terms, porosity is a fundamental volumetric property that describes the potential storage of fluids (water, oil, or gas) in rocks. Most of the physical properties of rocks, including the speed of elastic waves, resistivity, and density, are influenced by porosity. As can be seen in Fig. 2.8, porosity (ϕ) is defined as the pore volume (V_p) divided by the total volume ($V_p + V_g$) of a rock, where V_g is the volume of the grains.

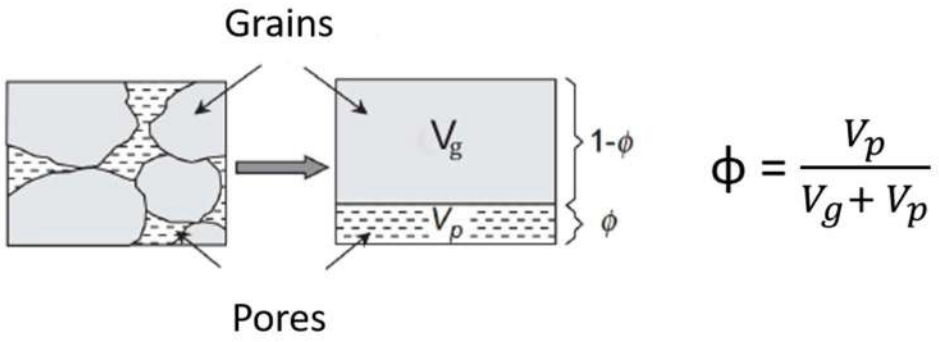

Figure 2-8. Porosity definition by SCHÖN (2016)

Porosity is a dimensionless quantity, usually expressed in fractions between 0 and 1, as percentages, or in terms in p.u's. (porosity units), where 1 p.u. is equivalent to 1% (MESQUITA, 2017). This property can be determined directly using different laboratory techniques, such as gas porosimetry or displacement methods, and, indirectly by profiling methods, such as through neutron responses, seismic wave speed and NMR measurements.

Figure 2.8 defines the porosity of rocks in terms of "total porosity". It is important to note that rocks often contain unconnected parts of the porosity (for example vugs and moldics pores) that do not contribute to fluid flow within the pore system. The term "not effective" is often used for such cases. There are two important definitions that distinguish the pore volume:

- Effective porosity: the fraction of the pore space that is interconnected inside a rock. Effective porosity is always less than the total porosity (HOOK, 2003), and can be easily determined in the laboratory;

- Non-effective or residual porosity: the fraction of the pores that are disconnected from the pore system, and thus do not contribute to the flux inside the rock (AHR, 2008);
- Total porosity: total void (or pore) volume within the rock, being the sum of effective and residual porosity.

CHOQUETTE & PRAY (1970) claim that most carbonate reservoirs have porosities between 5% to 10%, whereas terrigenous reservoirs, such as sandstones, have values between 15% and 30%. However, these values are not considered rules. For example, MOREIRA (2010) classified porosities according to the reservoir quality, as seen in Table 2.1.

Table 2-1 – Pore quality classification of reservoir rocks (MOREIRA, 2010)

Porosity	**Quality**
$\phi < 5\ \%$	Bad
$5\% < \phi < 10\ \%$	Moderate
$10\% < \phi < 20\ \%$	Good
$\phi > 20\ \%$	Excellent

Pores formed concurrently with the formation of a rock are often called primary. However, when formed after deposition, they are referred to as secondary, being a consequence of diagenetic actions, such as dissolution, cementation, recrystallization, dolomitization, and mineral replacement (such as aragonite converting to calcite), in addition to leaching of grains and compaction by burial, which is often predominant in rocks. These factors directly affect the makeup of the pore space and may increase or decrease the porosity as can be seen by the data in Table 2.2. Because of the often high impacts of these effects, carbonate rocks generally have a variety of pores, both in terms of size and shape, while also having an irregular spatial distribution. This causes the geometric analysis and quantification of this group of rocks to become difficult tasks, while still being fundamental for the definition of reservoir properties.

Table 2-2 – Factors that influence the formation of pore space (modified from PETERS, 2012)

Influencing Factor	Result
Fracture	Increases porosity
Clay	Decreases porosity
Cimentation	Decreases porosity
Grain size	Does not affect porosity
Poorly sorted grains	Decreases porosity
Well sorted grain	Increases porosity
Compaction	Decreases porosity
Dissolution	Increases porosity

One may view the pore system of a rock at the micro-scale in terms of two types of pores: pore bodies that are responsible for the storage of fluids, usually with larger sizes, and pore throats responsible for the connection between the pore bodies. The throats have a strong influence on permeability and determine to a large extent the size, shape and arrangement of the pores in a rock sample. If a rock is composed of well-defined spherical grains, the pores between them, classified as intergranular, will have only one grain size fraction, and may have throats and pore bodies of similar size. Rocks with poorly selected grains generally have poorly selected pore bodies and pore throats of varying sizes. The classification and distribution of pore throat sizes in rocks determines the body-throat pore ratio and the accessibility of liquids within the pore space (AHR, 2008).

Different nomenclatures have been developed to classify pores. ARCHIE (1952) was a pioneer in the classification of pores, encompassing its nomenclature aspects related to the rock fabric and its petrophysical properties. His classification was based on textural descriptions of the reservoir rocks along with characteristics of visible porosity. His contribution was to develop a classification system that emphasized the structure of the pores, the characteristics of fluid flow and the distribution of fluids. Another important classification was developed by CHOQUETTE & PRAY (1970), who recognized the importance of time and the way pores are formed in carbonate rocks, including geological

concepts associated with the pore space, thereby emphasizing the importance of pore genesis. However, LUCIA (1983) developed a more generic classification system by not reporting geological origins of the rocks and its pores, but emphasizing the relationship between porosity, permeability, and particle size. The main objective was to classify carbonate rock samples in a more practical way by using a more visual description for laboratory and field studies. In this study, the nomenclature of CHOQUETTE & PRAY (1970) will be used, to be presented in the chapter on materials and methods.

2.3 Permeability

Permeability (k) is a fundamental petrophysical property that defines the ability of a fluid to pass through the interconnected pore system of a rock. The connections that allow the fluid flow in the system are called pore throats. Due to the complexity of most natural rock formations, permeability is commonly anisotropic (SCHÖN, 2016).

The permeability of the rocks can be defined in three different ways:

- Absolute permeability (k_{abs}) – refers to laminar flow of a single fluid that does not react with the rock (100% fluid saturation). This property can be measured on samples in the laboratory, often done by commercial companies;
- Effective permeability (k_{ef}) – refers to the flow of a fluid in a p\rtially saturated rock. Generally, the sample contains then a wetting fluid and a non-wetting fluid, with little or no miscibility between them;
- Relative permeability (k_{rel}) – refers to the ratio between the two previous permeabilities, i.e., k_{ef} divided by k_{abs}.

Fluid flow (Q) is described by Darcy's law (DARCY, 1856) as follows:

$$\mathbf{Q} = \mathbf{A}\left(\frac{\boldsymbol{k}}{\boldsymbol{\mu}}\right)\left(\frac{\boldsymbol{\Delta P}}{\mathbf{L}}\right) \qquad (2.1)$$

where k is the permeability, μ is the viscosity of the fluid, $\frac{\boldsymbol{\Delta P}}{\mathbf{L}}$ is the potential drop in the sample and A is the cross-sectional area of the sample. Permeability is a property of the rock, and viscosity of the fluid, while $\frac{\boldsymbol{\Delta P}}{\mathbf{L}}$ is a measure of the flow potential. In the

International System (IS), permeability is given in m^2, but in the oil industry, permeability is usually given in terms of Darcy (D), where 1D = 0.831 m/day.

The permeability varies considerably in carbonate rocks. Values can be less than 0.1 mD for mudstones (almost impermeable), but can reach 10 D for connected vug systems, fractures or caves. Differences in the size, shape, and distribution of pores, the size and shape of the mineral grains, and the weft of a rock, all lead to a wide variation in the permeability, thus making it difficult to predict soil reservoir productivity. Qualitatively, the permeability values can be categorized as follows (Table 2.3).

Table 2-3 - Qualitative description of permeability in carbonate rocks (NORTH, 1985)

Qualitative description	Permeability (mD)
Poor to fair	< 1.0 – 1.5
Moderate	15 – 50
Good	50 – 250
Very good	250 – 1000
Excellent	> 1000

Permeability measurements in the laboratory are often carried out using special cells (e.g., *Hassler* cell) that allow one to control the fluid pressure gradient within the sample, thus leading to fluid flow and obtaining estimates of the permeability using Darcy's law. Both a liquid or a gas can be used to determine this property in the laboratory. When a gas is used, low pressures gradients are needed, with the speed of the fluid (in this case gas) along the walls of the capillaries (the pore throats) usually not becoming zero as in the case of liquids. This causes an overestimation of the permeability, often referred to as the *Klinkenberg effect* (TANIKAWA & SHIMAMOTO, 2006). To correct for this anomaly, measurements are typically carried out at different pressures, and the results are extrapolated to an infinite pressure (COSENTINO, 2001). This permits one to correct the values and bring them closer to values obtained when using a liquid (SCHÖN, 2016).

Direct in-situ permeability measurements are also possible in nature, such as packer tests and pumping tests, but these are generally very expensive and complex. For

this reason, measurements are often done using geophysical methods involving a variety of well-logging tools (ELLIS & SINGER, 2008). According to SCHÖN (2006), the development and application of NMR technique for the evaluation of formations has brought much new knowledge about the rock pore space, and the behavior and distribution of fluids within the pores.

2.4 Rock Typing

Rock typing is the identification of reservoir rocks in terms of categories based on petrophysical data such as porosity and permeability. The method is a simplification methodology that aims to group rocks having similar petrophysical characteristics (AHR, 2008). Rock typing represents a simple grouping method where the characteristics of the pores are a primary factor for a basic description of the reservoir rocks. Its results can be combined with other information, such as rock classifications, capillary pressures-saturation curves, as well profile signatures, with as ultimate aim the identification and mapping of reservoir flow units.

The rock typing methodology has a wide range of applications. These include applications for drilling, for example to predict the loss of drilling mud at high intervals; for production studies, such as to identify potential production zones, drill locations, the design of diversion systems during acidification, and prediction of high injection zones (ROQUE *et al*., 2017; OLIVEIRA *et al*., 2016); for reservoir studies to define net-pay (KOLODZIE, 1980); to obtain representative sample selections for special core analysis (SCAL) (SERAG EL DIN *et al*., 2014; MIRZAEI-PAIAMAN e SABOORIAN-JOOYBARI, 2016); and for permeability predictions (AMAEFULE *et al*., 1993; ABBASZADEH *et al*., 1996; DAVIES e VESSELL , 1996; TASLIMI *et al*., 2008; ASKARI E BEHROUZ, 2011; CHEN e YAO, 2017); among many other applications. Generally, petrophysical rock typing methods can be classified into two separate categories:

- Methods that use permeability and porosity. Excluding cut-off and other empirical methods, these include the Winland R_{35} equation (WINLAND, 1972; KOLODZIE, 1980), Pittman equations (PITTMAN,1992); FZI by AMAEFULE *et al*. (1993) and FZI* (FZI-Star) by MIRZAEI-PAIAMAN *et al*. (2015);

- Methods based on capillary pressure data along with the J-function, and empirical clustering technique (THOMEER, 1960; LIN *et al*., 2015).

Although there are other methods, the first category receives much interest in the oil and gas industry, and in academia, since there is no dependence on capillary pressure and/or relative permeability data (MIRZAEI-PAIAMAN *et al*, 2018). The identification of flow units and petrophysical rock types is especially difficult because of many variations in pore geometry, the lack of correlations between pore size and pore throats, and between porosity and permeability, and difficulty in establishing any link between the properties of small pores and the properties of a reservoir at the larger scale. Therefore, defining a link between the petrophysical view of a reservoir and the geological view is not trivial (SKALINSKI, 2009).

Methods for determining theoretical rock types are generally based on Kozeny-Carman type equations. Empirical correlations have been established between porosity, permeability, and a representative pore throat radius, derived from mercury injection capillary pressure data (PURCELL, 1949). The specific radius of a pore throat can then be used as an index to characterize the pore geometry dominating fluid flow. Unfortunately, the coquinas employed in this research are unusually complex in terms of their geological and petrophysical properties. As reported by CORBETT *et al*. (2016), coquinas from the Morro do Chaves Formation have a diagenetic history that provides many challenges, such as showing dramatic differences in permeability with only minor variations in porosity. New rock types hence may need to be developed to better correlate observed petrophysical characteristics of the coquinas with their fluid flow properties. CORBETT et al. (2016) used for this GHE (*Global Hydraulic Element*) base maps to separate the samples into two groups, one composed of low-quality reservoir rocks and the other of high-quality rocks. Still, they suggest that additional subdivisions may be required for these rocks because of unusual difficulties in describing their petrophysical properties.

Following the idea to possibly create more subdivisions, a literature search was conducted on the subject, leading to a study by ROMERO (2016). In that study, existing relationships between lithology and the time distribution of transversal relaxation (T_2) were used to identify prior knowledge that each shape of the T_2 curve corresponds to a particular lithology of some reservoirs in western and southern Venezuela basins. Knowing that the T_2 distribution can be related to the pore geometry, ROMERO (2016)

presented an approach for determining the rock quality using NMR measurements of the plugs. T_2 relaxation measurements were performed in the laboratory using various clastic reservoir plugs from eastern Venezuela. The results showed that samples corresponding to the different rock types presented a characteristic pattern in the form of the T_2 distribution. The advantage of this classification is its direct determination, without a need for further analysis to characterize the types of rock.

Following the suggestions by CORBETT *et al*. (2016) and the research by ROMERO (2016), specific rock types will be developed in this research in order to understand and more accurately estimate the permeability of coquinas from the Morro do Chaves Formation.

2.5 Nuclear Magnetic Resonance

NMR is a fast, non-destructive technique that can be used to obtain much information about the analyzed rock, such as porosity, pore size distribution, type and viscosity of the fluids contained in the porous space, saturation, wettability, and permeability (e.g., FLEURY *et al*., 2001).

The porosity of complex systems can generally be determined by the application of a wide range of techniques, such as mercury intrusion capillary pressure (MICP) analysis, gas adsorption (gas porosimetry), X-ray scattering at low angles, and density measurements. All of these techniques have restrictions, such as the need to assume a specific geometry for the pores, overlap in the limits of the pore sizes with their interconnected network, and percolation effects caused by the fluid/gas flow. According to SOUZA (2012), NMR is an attractive alternative because it does not require a particular geometric pore modeling approach in that the method encompasses a broader range of pore sizes (ranging from nanometers to millimeters), and is not affected by the effects of percolation. Due to its versatility, its accuracy in measurements of porosity and the volume of fluids contained in the rocks, NMR can be applied both in the laboratory using benchtop equipment, also for well logging (COATES *et al*.,1997).

NMR techniques are based on the response of atomic nuclei (spins) to external magnetic fields. The possibility of manipulating these spins in one or more dimensions allows the deployment of NMR in many experiments, thus providing unique versatility compared to other spectroscopic techniques. The hydrogen spins, present in the water molecules contained in the saturating fluid of the samples, are analyzed using NMR. The

^{1}H isotope, with its relatively high magnetic moment, is generally used the most for this purpose (FIORELLI, 2015). Exciting the spins in the presence of a magnetic field makes it possible to manipulate the movement and direction of the spins, thereby capturing information about the system.

NMR measures the amplitude and decay curve of the signal. The amplitude is proportional to the density of hydrogen in the pore fluids and, therefore, is an indicator of porosity. The signal decay curve provides information about the types of fluids and their interactions with the pore system. Thus, NMR measures three properties: the equilibrium of nuclear magnetization, *Mo*, and two main relaxation times: T_1 (the longitudinal relaxation time) and T_2 (the transversal relaxation time). *Mo* is proportional to the porosity occupied by the fluid, while T_1 and T_2 can be correlated with such petrophysical properties as pore size, the fluid produced, and permeability (ROSSINI *et al*. 1997). Although T_1 measurements are most commonly used in the literature, they consume more time than T_2, while also having a lower signal-to-noise ratio in the experiments, a fact inherent in any NMR measurement (KENYON, 1997).

Transversal relaxation (T_2) involves the contribution of three processes:

$$\frac{1}{T_2} = \frac{1}{T_{2S}} + \frac{1}{T_{2B}} + \frac{1}{T_{2D}} \qquad (2.2)$$

where T_{2B} is the bulk volume relaxation, T_{2S} is the superficial relaxation, and T_{2D} is the diffusional relaxation. Equation (2.2) is considered one of the fundamentals to evaluate NMR. The term bulk relaxation is used for relaxation measurements of a fluid when the effects of walls and gradients are eliminated. This relaxation is generally inversely proportional to viscosity. Superficial relaxation is the result of interaction of the spins with the pore wall. This effect is responsible for the sensitivity of NMR to pore size and, consequently, the permeability and the amount of irreducible fluid. The relationship of the spins is shortened due to molecular diffusion in a non-homogeneous static magnetic field (gradient), which is represented by T_{2D}. This inhomogeneity on a meter to centimeter scale is a result of the configuration of the permanent magnet inside the tool and appears on the micrometer scale, in contrast to the magnetic susceptibility between the grain and the fluid.

Transverse (or spin-spin) relaxation times, T_2, are typically determined using a pulse sequence called CPMG (Carr-Purcell-Meiboom-Gill), which was improved by MEIBOOM AND GILL in 1958. Through this sequence, the intensities of the echoes are

measured until they are no longer observed, thereby generating a multi-exponential decay which characterizes the complex nature of rocks. Using inverse Laplace transforms, the signal decays are transformed into relaxation curves that are linked to the pore size distribution of the sample. Shorter relaxation times with faster decays represent smaller pores, while larger pores are represented by long relaxation times with longer decays (Figure 2.9). Experiments performed in the laboratory commonly have defined a logarithmic time span between 0.1 ms and 10 s, thus presenting a wide range of points, also called *bins* (Figure 2.10). The number of points is reduced in well-logging because of the shorter time frame involved. These and related theoretical aspects of NMR techniques are discussed by KENYON (1997), ROSSINI *et al*. (1997), COATES *et al*. (1999), and FIORELLI (2015).

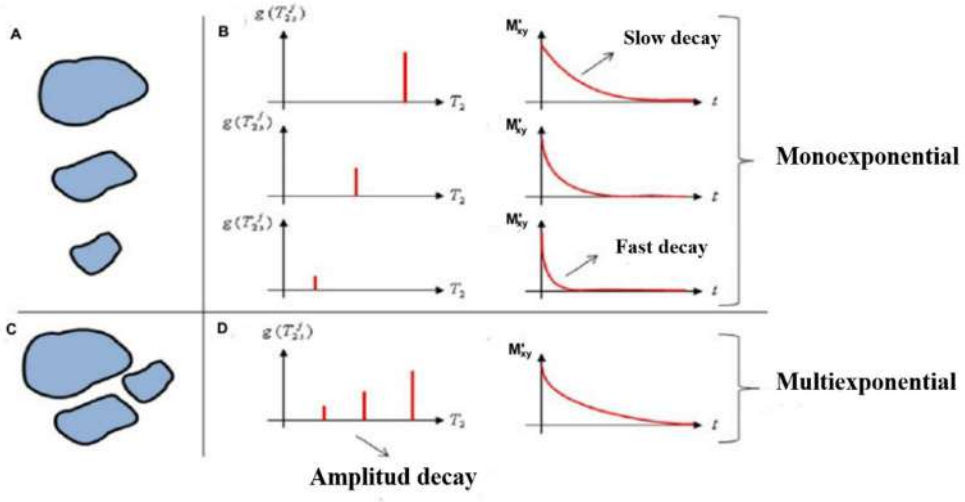

Figure 2-9. - Comparison between amplitude and decay for different pore size distributions.

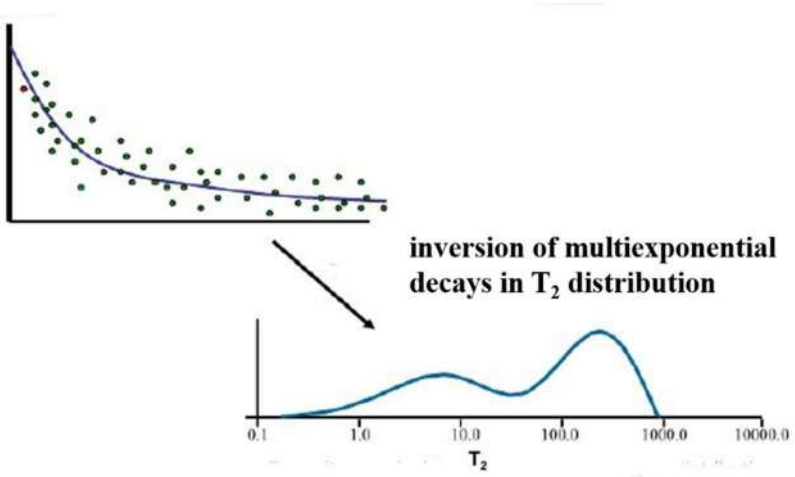

Figure 2-10. - Schematic of the inverse Laplace transform to obtain the pore size distribution of the system (STROMBERG, 2008)

2.5.1 Permeability Estimation Using NMR

One major advantage of NMR techniques is the possibility to estimate the permeability of a rock sample. Permeability is an important parameter for the reliable development of petrophysical and geological models of reservoirs by directly impacting oil and gas production strategies. Since permeability is difficult to estimate directly using well-logging, NMR techniques have undoubtedly become the main approach for making such estimates. Another important aspect of NMR is its versatility since the experiments can be carried out in both the laboratory and the field (FLEURY *et al*., 2001).

For a saturated sample, T_{2B} and T_{2D} are generally much larger than the superficial relaxation time, T_{2S}. In this way T_2 can be approximated as

$$\boldsymbol{T_2 \cong T_{2S} = \frac{1}{\rho_2}\frac{V}{S}} \qquad (2.3)$$

where $\frac{V}{S}$ is the ratio between pore volume and the pore surface area, and ρ_2 is the superficial relaxivity, a parameter related to the abundance of paramagnetic ions on the pore surface (KLEINBERG, 1999). Since T_2 is related to $\frac{V}{S}$, the T_2 measurements should provide all information necessary to calculate the permeability (DAIGLE & DUGAN, 2009).

Several mathematical models have been developed over the years with various success to estimate the permeability; the main formulations are described below. In 1927, Josef Kozeny developed the first empirical model to estimate the permeability, which in

1936 was refined by Philip Carman. The resulting model is known as the Kozeny-Carman equation (e.g., SCHEIDEGGER, 1974):

$$\boldsymbol{k = \frac{\phi^3}{\tau(1-\phi^2)}\left(\frac{V}{S}\right)^2} \qquad (2.4)$$

which shows that permeability is related to the volume to surface ratio$\left(\frac{V}{S}\right)$, also called the hydraulic potential ratio, the total porosity (φ), and the tortuosity (τ) of a sample. SCHEIDEGGER (1974) pointed out that the permeability can be derived from general considerations of fluid flow through capillaries tubes. DAIGLE & DUGAN (2009) demonstrated that the complexity of the porous medium depends on the degree of tortuosity in that a more tortuous pore network leads to a lower permeability of the system.

The first direct relationship between NMR measurements and the permeability was developed by SEEVERS (1966) (Eq. 2.5):

$$\boldsymbol{T_{1Logmean} = \frac{1}{\rho_1}\left(\frac{V}{S}\right)} \qquad (2.5)$$

in which $T_{1Logmean}$ is the geometric mean. In this formulation, the geometric mean is a proportional quantity reflecting the average pore size within the system, ρ_1 is the longitudinal superficial relaxivity and $\left(\frac{V}{S}\right)$ is the same ratio as used in the Kozeny-Carman equation. Thus, Seevers proposed the relationship (Eq. 2.6):

$$\boldsymbol{k = a\,.\,\phi\,.\,T^2_{1logmean}} \qquad (2.6)$$

where *k* is the permeability and *a* is an empirical constant dependent on the rock lithology. This model assumes that longitudinal relaxation is dominated by the interaction of the fluid with the surface, and that this interaction produces high values of ρ's, thus maximizing the dependence on $T_{1Logmean}$ through pore size.

The use of longitudinal relaxation times is often a hindrance in NMR logging operations since it requires long times for the accurate acquisition of the decays. To avoid this problem, longitudinal relaxation times ($T_{1Logmean}$) were often replaced by transversal relaxation times ($T_{2Logmean}$), starting in the 1990s with the improvements of the NMR techniques.

The reliability of the Kozeny-Carman model was tested by RIOS *et al*. (2014). A comparative study was carried out between the NMR estimators using different means of the transversal relaxation times ($T_{2Logmean}$), based on the industry's concern about pre-existing models for the permeability, especially when used for complex carbonate rocks (RAMAKRISHNAN *et al.*, 1999). While $T_{2Logmean}$ usually was calculated by logging interpreters using geometric averages (KENYON, 1997; KLEINBERG, 1999), resulting values for this property often differed widely. For this reason, many used chalk samples (fine-grained carbonate rock) saturated in brine, to determine the T_2 times. Based on the Kozeny-Carman equation, and its modifications, the predictive performance of three estimators based on classical Pythagorean averages (harmonic, geometric and arithmetic) were evaluated. RIOS *et al.* (2014) presented as one of the results of their study that, in some cases, geometric mean would not be the best way to estimate NMR permeability. Calculations using arithmetic means performed better in their case study.

The Seevers model has certain applicability limits. Previous studies have shown that the model works very well to estimate the permeability of uniform porous media, but not necessarily for heterogeneous systems. Several new mathematical models were generated in attempts to improve the accuracy of the permeability predictions. KENYON *et al*. (1988) used hundreds of sandstone samples to develop the following equation, also known as the SDR (Schlumberger-Doll-Research) model:

$$\mathbf{k_{sdr} = c \cdot \phi^{a} \cdot T_{1Logmean}^{b}} \qquad (2.7)$$

where k_{sdr} is the permeability, b and c are empirical constants, and c is an empirical parameter depending upon the lithology. KENYON *et al*. (1988) obtained values of 4, 2 and 4.5 for the constants a, b and c, respectively. They pointed out that longitudinal superficial relaxivity is implicitly included in the constant c, which hence should have the same value for the same lithology. STRALEY *et al*. (1995b) later applied Eq. (2.7) to sandstone and carbonate rocks, but with the parameter $T_{1Logmean}$ changed to $T_{2Logmean}$. They estimated the value of c for carbonate rocks to be 0.1, but with the sandstone rocks showing much smaller values.

In a study of 155 sandstone rock samples, TIMUR (1968) proposed an equation relating the permeability to porosity (ϕ) and irreducible saturation (S_{wir}):

$$\mathbf{k = 0.136 \left(\frac{\phi^{4.4}}{S_{wir}^{2}}\right)} \qquad (2.8)$$

In a new study using the same set of samples, TIMUR (1969a) proposed a relationship between the effective porosity (ϕ_{ef}), the Free Fluid Index, *FFI* (part of the fluid that can be removed from the reservoir), and the fraction of the pores that retain fluids (S_{wr}), according to the equations

$$\boldsymbol{\phi_{ef}} = \left[\mathbf{1} - \frac{\boldsymbol{S_{wr}}}{\mathbf{100}}\right] . \boldsymbol{\phi} \qquad (2.9)$$

$$\mathbf{S_{wr}} = \mathbf{100} . \left[\mathbf{1} - \frac{\mathbf{a\,(FFI)+b}}{\boldsymbol{\phi}}\right] \qquad (2.10)$$

TIMUR (1969b) further improved the results by using 188 sandstones samples, leading to relationships between the NMR signals and *FFI* using three components with decays at different times. The parts represented the total percentage of the pore space (called *FFI3*), indicating that this parameter is identical to the effective porosity value. This study considered that the different pore sizes presented different relaxation times, thus affecting the prediction of permeability.

Based on the model by TIMUR (1969b), COATES (1991) developed a new equation for the permeability based on the relationship between the free fluid index (*FFI*) and the bulk fluid index (*BFI*), the latter representing fluid adsorbed by clay minerals and fluid trapped by capillarity:

$$\mathbf{k_{Tim}} = \mathbf{c} \left(\frac{\boldsymbol{\phi}}{\mathbf{100}}\right)^{\mathbf{a}} . \left(\frac{\mathbf{FFI}}{\mathbf{BFI}}\right)^{\mathbf{b}} \qquad (2.11)$$

in which the constants *a*, *b* and *c* are determined by multiple linear regression (MLR). The values now used mostly in the oil industry are those determined by KENYON *et al*. (1986), notably values of $a = 4$ and $b = 2$, for sandstone rocks. The equation above is known as the Timur-Coates equation (TC).

The Schlumberger-Doll-Research (SDR) and Timur-Coates (TC) equations are considered classics in terms of estimating the permeability from NMR data (RIOS *et al*., 2010). They assume that the T_2 spectrum represents the pore size distribution. The equations have been found to work well for homogeneous rocks, i.e., rocks where the pore system shows a good correlation between the size of the pore bodies and the size of the pore throats, a characteristic not observed for many carbonate rocks (CHEN, 2008).

Subsequent studies using the SDR and CT equations were performed by many. MACHADO *et al*. (2011) presented a way to estimate the permeability using the two equations, but with the application differentiated based on the pore sizes. Previous studies

about the superficial relaxivity showed that in a porous medium composed of micro- and meso-porosity (i.e., smaller pores), the walls have more interaction with the spins during NMR experiments, which then governs the superficial relaxivity. In a system dominated by macropores, T_2 loses sensibility caused by the pore sizes, but not by their volume. Based on these concepts, good correlations could be established by MACHADO *et al*. (2011) for the K_{Sdr} equation when the system has a predominance of macropores, with a new equation being proposed (K_{Macro}) for macropore systems, modified from the Timur-Coates equation (K_{Tim}).

2.6 Mercury Injection Capillary Pressure

Mercury Injection Capillary Pressure (MICP) analysis is a laboratory test used to characterize porous media. The experiment, first proposed by WASHBURN (1921), is capable of obtaining the capillary pressure curve of a porous medium, which can be converted into a distribution of the radii of the interconnected pores of a rock sample. The results provide important input to multiphase flow models and can be compared to the pore size distributions distribution determined using NMR.

Although MICP is an old technique, it is still considered one of the most reliable methods in the oil industry. The main advantages are:

- Experiments can be performed on fragments of samples having irregular shapes;
- The technique offers a very accurate analysis of the porous rock system by providing both the pore sizes and the accessible amount of the pore volume after applying pressure;
- MICP allows the characterization of rock facies based on the radii of pore throats;
- The method can be used to obtain the effective porosity using the total intruded mercury volume after application of some maximum pressure;
- Results may be used to estimate the permeability.

However, the technique also has limitations such as its destructive nature, which limits its use to laboratory analyses, but not for in-situ field applications. This main limitation relates to the toxic nature of the intruded fluid (mercury), which makes it

necessary to discard the samples after the tests due to the high risk to health. For this reason, MICP techniques have gradually been replaced by NMR measurements to estimate pore distributions and volumes, while centrifuge techniques are increasingly being used to obtain capillary pressure – saturation curves since those measurements are not destructive in nature. (SOUZA, 2012).

Much research has been carried out using MICP techniques. For example, HELINGER JR. & SANTOS (2018) applied the technique to coquina samples from the Brazilian pre-salt, to evaluate the influence of pore throats on different types of porosity. They found that samples with mostly moldic pores have narrower throats when compared to samples with interparticle pores, thus directly impacting the permeability.

Another popular application is to use MICP to develop hydraulic rock types. Since MICP measures the pore openings (throats), its results can be used to evaluate the connectivity and flow properties of the samples. MIRZAEI-PAIAMAN *et al*. (2015) proposed the use of two types of rock types: one static, where the samples have similar capillary pressure curves but different flow characteristics, and one formed by samples with similar flow behavior but different capillary pressure curves. THEOLOGOU *et al*. (2015) further developed a methodology that accounts for sample selection, acquisition, data quality control and corrections, and parameterization of the MICP curves through Gaussian decomposition. Their methodology focused on the development of rock types to predict the types of pores determined by MICP for the well scale.

MICP results can be combined with the NMR measurements and applied in several ways to provide a complete characterization of the pore space, such as the pore body and pore throats distributions, irreducible saturation, permeability, and superficial relaxivity. MARSCHALL *et al*. (1995) presented estimates of irreducible saturation and permeability by correlating the two techniques. They showed that the combination of NMR (pore body) and MICP (pore throat) responses could be used to determine superficial relaxivity. Using the T_2 amplitudes and the pore size distributions, a combination of both curves can be obtained by transforming the relaxation times into a pore radii and defining the relaxivity. Many other works have been developed along these lines of research.

2.7 Porous Media Modeling

One of the difficulties in predicting the flow behavior in porous media is the high degree of uncertainty associated with determining the quantities that govern fluid retention and flow (AMBRUS *et al*., 2004). The study of pore-scale processes is essential for understanding the flow and transport processes at the continuum or macro scale, which implies a multi-scale problem (RAOOF *et al*., 2013). These various scales have an associated hierarchy, covering the molecular scale, the micro or pore scale, the macro or laboratory scale, the meso or field scale, and also the mega or regional scale.

One increasingly popular approach to obtain important information about porous media is through Pore Network Modeling (PNM). A bridge can then be developed between the processes at the pore scale and the macro scale, with PNM serving as a tool for establishing how processes at the pore scale are manifested at the macroscopic level (i.e., the core or even field-scale). PNM hence is a valuable tool to understand macroscopic behavior by evaluating relevant physics on the pore scale.

PNM has been widely used in petroleum engineering studies (e.g., WILKINSON & WILLEMSEN, 1983). Its application is extremely useful to obtain the constitutive properties of the samples. The approach typically involves images acquired from X-ray microtomography (micro-CT), from which 3D skeletons are generated, with PNM then providing details of porous media flow and retention parameters that are of fundamental importance for the simulation of multiphase flow (LEI YANG *et al*., 2018).

Capillary bundle models have traditionally been used to estimate the relative permeability of porous media, such as the initial study by PURCELL (1949) and many others since then (BURDINE, 1953; MUALEM, 1976). According to this approach, porous media can be modeled using capillary tubes of different diameters. Such models ignore the interconnectivity of natural porous media and often do not give very realistic results. However, with the use of PNM, pore bodies (nodes) and pore throats (or channels) are used with a specific topological configuration, with the pore throats prescribing the connections between pore bodies. The pore bodies are represented by large empty spaces (generally modelled as spheres) inside the rocks, while the pore throats (modeled as capillary tubes) serve as connections between the pore bodies. Pore networks have been widely used for estimating multiphase flow properties (BLUNT *et al*., 2001; ALGIVE *et al*., 2012), as well as for modeling the dissolution of organic liquids (ZHOU *et al*., 2000), CO_2 sequestration (RAOOF *et al*., 2012), biomass growth (ROSENZWEIG *et al*., 2013),

solute dispersity (VASILYEV *et al*., 2012), adsorption (RAOOF *et al*., 2010), and the hydraulic conductivity (THULLNER *et al*., 2002), among others.

PAN *et al*. (2004) noted that fluid flow simulations using the Lattice Boltzmann approach (SHOLOKHOVA *et al*., 2009) may be very accurate, but are almost impossible to run for realistic representative elementary volumes (REVs). Thus, new models needed to be developed, including pore network models. One main advantage of PNMs is their efficient use of detailed geometric and topological information, even for porous media that have a disordered geometry. Thus, the prediction of multiphase flow properties within the porous space can be carried out in an easier way. Still, one of the deficiencies of the technique is its need to use a simplified geometry for the porous media, normally by assuming uniform circular or square shapes with idealized cross-sections. Accurate simulation of several processes, such as biogeochemical reactions, hence may become a challenge since they involve significant changes in the complex pore geometry resulting from dissolution, precipitation and/or biological clogging (RAOOF *et al.*, 2013).

Recent advances in PNM techniques allow one to consider a certain degree of irregularity in the shape of cross-sections of the pore throats with relatively low computational cost, thus improving the ability to capture important statistical characteristics of the medium, such as pore size distributions (LINDQUIST *et al*., 2000), the distribution of coordination numbers (RAOOF & HASSANIZADEH, 2009) and topological parameters such as the Euler number (VOGEL & ROTH, 2001).

YANG *et al*. (2017) carried out an important study showing the quantitative predictive potential of PNM pore by pore. They made a direct comparison of PNM simulations and experiments using corresponding micro-models of the same scale and pore-scale geometry. Their research showed that a pore network dynamic flow solver can predict the displacement of two-phase flows in pore-scale drainage experiments. YANG *et al*. (2018) further studied the permeability of porous media containing a gas hydrate (a compound of water and gases with small molecular weight). Since gas is generally distributed unevenly in the samples, the inhomogeneity can significantly impact the permeability of a reservoir. They employed PNM calculations using acquired micro-CT images to observe the effects of different pore body and pore throat radii, non-uniform hydrate distributions and fluid flow directions on both the absolute and relative permeability.

2.8 Principal Component Analysis (PCA)

Multivariate analysis, in general, refers to statistical methods that simultaneously analyze multiple measures of an object under investigation. Of many available multivariate techniques, principal component analysis (PCA) is one of the most popular statistical techniques for data analysis in several disciplines such as agronomy, hydrology, biology, ecology, and medicine.

The PCA methodology was first described by PEARSON (1901), but later formulated in terms of practical computational methods by HOTELLING (1933, 1936). PCA is a multivariate statistical technique that linearly transforms a set of variables, initially correlatable to each other, into a considerably smaller set with no correlation between them, but still keeping most of the information from the original set. According to HONGYU (2015), PCA techniques aim to redistribute the variations observed along the original axes to obtain a set of non-correlated orthogonal axes.

The PCA technique consists of transforming a set of original variables into another set of variables of the same dimension, called principal components. These components have important properties since each main component is a linear combination of all original variables, but independent of the others and estimated such that they retain the maximum amount of information in terms of the total variation contained in the data (JOHNSON & WICHERN , 1998). Having this understanding in mind, it can be concluded that the maximum variations will be in increasing order of the components, starting with principal component 1 (PC1) until the last one. When interpreted in this way, the PCs with the greatest variances will present the best correlations in that they will explain the maximum variability of the data, with only the first two components being used normally. All components can be correlated with each other for interpretation, but the smaller the variance, the more difficult it will be to interpret the results.

PCA techniques can be used to generate indexes or group individuals or objects. Their main objective is to explain the structure of variance and covariance of a random vector, by means of linear combinations of the original variables. The linear combinations represent, geometrically, a new coordinate system obtained by rotating the original system such that the new coordinate axes have $\boldsymbol{p}$ random variables. The new orthogonal axes (new variables) are called scores of the principal components. The analysis groups individuals according to their variation, implying that individuals can be grouped

according to their behavior within the population, represented by variations in the characteristics of the settings that define the individual.

HONGYU (2015) explained that to establish an index that makes it possible to order a set of ***n*** objects according to criteria defined by a set of appropriate ***m*** variables, it is necessary to choose the weights of the variables that translate the information contained in them. Although PCA technique was developed initially to solve specific problems (REGAZZI, 2000), they can be used to solve other problems such as reducing the dimensionality of variables and grouping individuals (observations) because of their similarities or differences, thus making them applicable to different areas of study.

The main advantage of the PCA methodology is the possibility of transforming a set of original correlatable variables into a new set of non-correlated variables (main components) by removing multicollinearity. In addition, PCA reduces many variables to perpendicular axes with fewer variables to explain the variations in data in a decreasing and independent way.

The method has as disadvantage its insensitivity to outliers, which causes many to not recommended its use in case of a lack of data. PCA techniques are also not recommended when there are more variables than sample units, which can lead to loss of information about the variability of the original variables. There are cases where the PCA does not work, for example when even with a reduction in the number of variables, the variability is still exceptionally large, which can be explained by the original variables having little correlation (HONGYU, 2015).

Since PCA is a multivariate method with wide application, it can be used for several problems of data analysis by helping one to identify similarities and explaining the results according to the variables used. RAMOS *et al*. (2009) applied the technique to 68 samples of Brazilian crude oil, ranging from light to extra heavy (having viscosities of 2 to 30,000 cP), and low-field NMR measurements used to predict and analyze the viscosities. Application of the PCA methodology showed that the first two principal components, PC1 and PC2, comprised 65% of the total variance, thus making it possible to identify distinct groups with good correlation between similar viscosity samples, according to the classification adopted by ANP (the National Petroleum Agency of Brazil).

RIOS *et al*. (2011) used PCA to predict the permeability of rock samples from observed NMR data. Using 68 sandstone samples from Brazilian reservoirs, two partial least-squares regression models (PLSR) were created to estimate the permeability from T_2 measurements, with results compared with estimates obtained using the classic

Kenyon model (K_{Sdr}). BENAVENTE *et al*. (2006) further used multivariate analysis to evaluate the pore structure, the water flow properties, and the resistance of rocks to wear by salt. PCA was used to examine the direct relationship between salt wear and the petrophysical properties.

3 MATERIALS AND METHODS

This chapter describes in detail the rock samples that were used, as well as the most relevant methods and measurements utilized for this research, including the invoked materials and techniques. The chapter gives more details regarding the proposed workflow in topic 1.3.

3.1 Coquinas from the Morro do Chaves Formation

For the development of this work, 44 coquina samples were used from a continuous test core (UFRJ 2-SMC-02-AL), drilled at Pedreira Atol, located in the city of São Miguel dos Campos in the Brazilian state of Alagoas (WGS-8409 ° 45'17"S / 36 ° 09'14"W), which is part of the Sergipe-Alagoas Basin. The core was provided by the Laboratory of Sedimentary Geology (LAGESED) of UFRJ. All samples had a cylindrical shape, about 2.5 cm in diameter x 4.5 cm in height (Figure 3.1).

Figure 3-1. - Detail of the plugs used in this work

As opposed to sandstone rocks, carbonate rocks are known for their complex and heterogeneous composition, attributed to various depositional and diagenetic processes. After the initial deposition of the rock, these processes significantly affected the internal

network of pores and their connections, leading to both more favorable as well as undesirable reservoir characteristics. Since they are formed by bioclasts, mainly lake bivalves, these components may undergo dissolution and hence lead to higher porosities of the rocks. Cementation on the other hand could drastically decrease the porosity, which would directly affect the storage and fluidity of carbonate reservoirs. All of these factors cause such rocks to become a challenge in terms of petrophysical modeling. The coquinas in this study were classified lithologically according to the scheme by GRABAU (1904). In this classification, sediments are divided into three categories:

I. Calcirudites: sediments with a particle size greater than 2mm;
II. Calcarenites: sediments with granulometry between 2 and 0.0625mm;
III. Calcilutites: sediments with granulometry less than 0.0625mm.

TAVARES *et al*. (2015) and RIGUETTI *et al*. (2018) previously carried out several studies in the Pedreira Atol area. The study by TAVARES *et al*. (2015), carried out in a mining front at Pedreira Atol, focused on the composition of the formation rocks (notably the presence or absence of micrite or siliciclastic material) and the degree of fragmentation of the shells. They suggested that facies with a predominance of fragmented shells, without micrite, would have been deposited in underwater bars, above the base level of good weather waves. The considerable fragmentation of the shells and the absence of micrite would indicate constant rework in a moderate to high energy environment. Facies with whole shells and the presence of micrite would have been deposited between the base level of action of good weather and storm waves. RIGUETTI *et al*. (2018) further provided both a macroscopic and microscopic description of core 2-SMC-02-AL, from which the plugs of this research were taken, aiming at the faciological and stratigraphic characterization of the coquinas. The well was divided into four stratigraphic intervals, with a predominance of different sedimentary facies and successions of facies, as shown Table 3.1.

Table 3-1 – Succession of sedimentological facies of well 2-SMC-02-AL, separated by stratigraphic intervals (modified from RIGUETI *et al*., 2018; TAVARES *et al.*, 2015)

Succession of sed. facies	Sedimentary facies	196.30 - 202.40m	169.35 – 196.30m	100.40 – 169.35m	64.20 – 100.4m
Nearshore	Calcarenite composed of fragmented shells (≥80%), showing plane-parallel or low angle cross-stratification **(cApp)**. Contains: ≤ 10% micrite ≤10% siliciclastics	-	2%	4%	5%
	Calcirudite with cross stratigraphy **(cRc)**	-	-	-	10%
	Calcirudite composed of whole shells (≥20%), densely packed, showing massive structure **(cRdm)**. Contains: ≥ 10% micrite ≤ 10% siliciclastics	-	80%	81%	16%
	Nodular microcrystalline carbonate **(Nc)**	-	1%	1%	1%
Offshore	Massive calcirudite, densely to loosely packed, with sandy-gravelly matrix **(cRpm).** Contains: ≥ 20% of non-fragmented shells ≥ 10% micrite ≥ 10% siliciclastics	-	-	-	1%
	Massive calcirudite, densely to loosely packed, moderately to poorly sorted terrigenous sandy-muddy matrix (**cRm**). Contains: ≥ 20% non-fragmented shells ≥ 10% micrite ≥ 10% siliciclastic	-	2%	5%	2%
	Massive green mudstone or with incipient lamination **(Fg)**	76%	1%	4%	5%
	Organic-rich mudstone finely laminated **(Forg)**	-	-	2%	3%
Hyperpicnal Flux	Calcirudite composed of whole bivalve shells; fragmented shells (≥40%), densely to loosely packed, well-sorted terrigenous sandy matrix showing cross-stratification (**cRdlc**). Contains: ≤ 10% micrite ≥ 10% siliciclastics	3%	4%	1%	51%
	Calcirudite composed of well-sorted, fragmented and whole bivalve shells (≥40%); densely to loosely packed, well-sorted terrigenous sandy matrix showing cross-stratification (**cRcl**). Contains: ≤ 10% micrite ≥ 10% siliciclastics	-	-	1%	-
	Moderately to poorly sorted, medium to coarse-grained sandstone, moderately to poorly sorted, showing cross-stratification **(Sc)**;	-	6%	-	-
	Well-sorted, fine to medium-grained sandstone, exhibiting cross lamination **(Scl);**	1%	1%	-	3%
	Well to moderate sorted, very fine to medium grained sandstone, graded **(Sg);**	-	1%	0.5%	3%
	Well sorted, very fine-grained sandstone, showing low angle divergent lamination **(Sdl);**	20%	2%	0.5%	-

Rock typing is a simplified methodology widely used in the study of reservoir rocks. It groups rocks with similar petrophysical characteristics, such as porosity and permeability (AHR, 2008), to facilitate the understanding of the reservoir. The porosity and permeability distributions are very important, especially for reservoir and

petrophysical engineers, for assessing the formation and defining recovery strategies, thereby improving also accurate forecasts using reservoir model simulations. Rock typing represents a simple grouping method in which the pore characteristics are the primary factor used to describe reservoir rocks. Its results can be combined with other information, such as rock classification, capillary pressure- saturation data and well profile signatures, aiming at the identification and mapping of the reservoir flow units. The identification of flow units and petrophysical rock types is generally difficult because of much variation in the pore geometry, a lack of correlation between pore body and pore throat sizes, poor correlation between porosity and permeability, and difficulty to establish links between the properties of the small coquina scale pores and the properties of a reservoir at a large scale. Therefore, establishing a link between the petrophysical properties and the overall geological properties of a reservoir is not trivial (SKALINSKI, 2009).

3.2 Routine Core Analysis

The samples were initially subjected to thorough cleaning and the extraction of fluids previously present in the pore system, an essential step for the complete removal of impurities contained in the samples. For this stage, Soxhlet extractors were employed using solvents such as toluene for removing hydrocarbons, and methanol for the extraction of salts and water. The advantage of using this technique is the possibility to completely remove natural contaminants in a continuous and unsupervised manner, without causing damage to the samples. After cleaning, the samples were dried in an oven at a controlled temperature of 60°C for 12 hours.

3.3 Fluid Saturation

After basic petrophysical tests, samples were prepared for the NMR (nuclear magnetic resonance) measurements. Preparation consisted of saturating the samples in brine at 30kppm of KCl, in order to minimize possible reactions of the clay material present in the samples. The brine had a density of 1.067 g/cm³. For this saturation, the samples were separated into two separate groups having high and low permeabilities. For the samples of high permeability (i.e., having values above 100 mD), a vacuum was applied to the samples immersed in brine. The lower permeability samples were applied vacuum for 8 houres before placed in a pressure cell, filled with the fluid until they were completely covered. It was applied a pressure of up to 2,000 psi for 24 hours to guarantee

total saturation (Fig. 3.2). After this step, the samples were weighed again and their dry mass subtracted from the wet mass, this giving estimates of the mass of the solution that entered the sample. The volume of solution present in the sample was calculated subsequently by dividing the mass of the solution by the density of the brine.

Figure 3-2 - Photo illustrating saturation of low permeability samples. a) Cell where samples remained for 24 hours, immersed in brine and under the pressure of 2,000 psi; b) Detail of the interior of the cell containing a sample immersed in the fluid

Complete as possible saturation of the samples is crucial for carrying out the NMR assays, with values above 95% considered to be ideal in order to obtain more accurate T_2 distributions. After determining the solution volume that entered the samples, all samples were kept in containers filled with the same saturating fluid (Fig. 3.3) for the purpose of maintaining ideal saturation. The sample saturation process was carried out at the NMR and Petrophysics Applications Laboratory at Universidade Federal Fluminense (UFFLar), Niteroi, Brazil.

Figure 3-3 - Samples stored in brine-filled containers to maintain saturation for NMR analysis

3.4 Nuclear Magnetic Resonance (NMR)

The NMR experiments were carried out in a low-field spectrometer GeoSpec2 (Oxford Instruments, UK), having a magnetic field equal to 0.047 T and a frequency of 2 MHz, belonging to the NMR and Petrophysics Applications Laboratory (UFFLar) (Fig. 3.4). All acquisition controls were implemented using GIT software (Green Imaging Technologies, Fredericton, Canada).

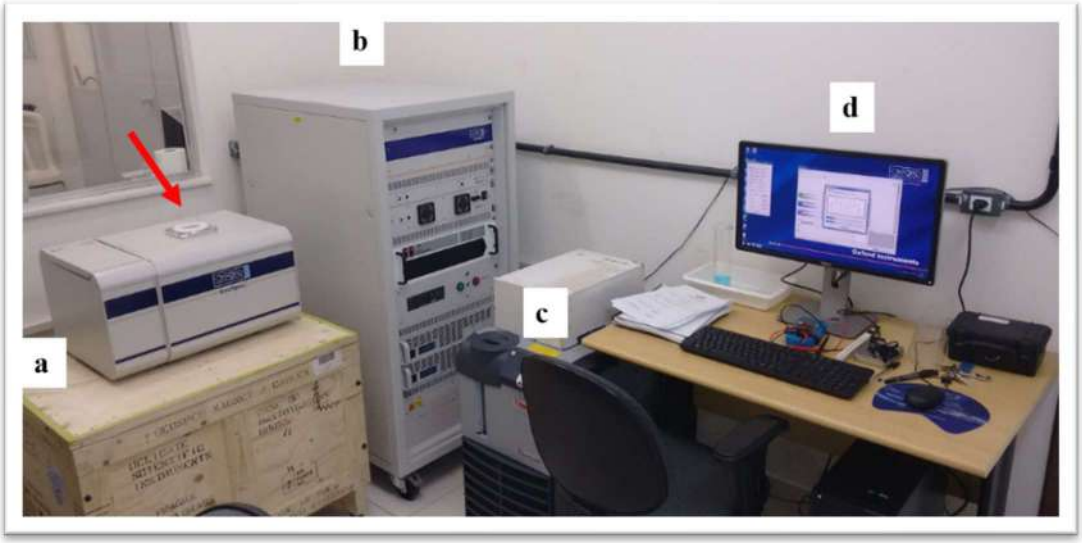

Figure 3-4 - NMR equipment used for the experiments. a) Equipment where the experiment is carried out, with detail of the sample entry at the top (red arrow); b) Tower containing the electronic part of the NMR; c) Equipment responsible for maintaining the temperature at 20 ° C; d) Computer to control the experiment, with GIT installed (source: website UFFLar)

After calibration of the equipment using a standard sample, the analysis started. The samples were wrapped with Teflon tape to contain saturation throughout the experiment and positioned inside the probe. Table 3.2 shows the parameters used to acquire NMR data.

Table 3-2 – NMR data acquisition parameters

Parameters	**Values**
Total echos	16,250
Echo time	200μs
Number of averages	64
Waiting time between averages	10s
90º pulse width	12,04μs
180º pulse width	24,24μs
Temperature	25ºC

The research was carried out using transversal relaxation measures (T_2) obtained by using CPMG pulse sequence, which are mostly used in petrophysical studies. A CPMG pulse sequence consists of a 90 ° radio frequency pulse followed by a pulse train of 180°, delayed by π/2 of the first pulse. Echo intensity measurements were performed with a signal/noise ratio above 100.

Typically, the pore size distribution of a sample directs the distribution of T_2 times, determined by mathematical inversion of relaxation measurements (BUTTLER *et al.*, 1981). At the limit of the fast diffusion regime, the time T_2 of a fluid that saturates a porous medium is given by (Eq. 3.1):

$$\left(\frac{V}{S}\right)_{pore} = \rho_2 T_2 \qquad (3.1)$$

where ρ_2 represents the surface relaxivity. This equation shows that the relaxation times of the fluids inside the pores are inversely proportional to the pore surface/volume ratio, defined as S/V in Eq. (3.1), with the scaling of this relationship being the surface relaxivity, ρ_2.

As a result of the experiment, the effective porosity and the pore size distribution curve of the sample are obtained. The porosity results can be compared with those obtained with the routine core analysis once the samples are well saturated. The pore size

distributions help to understand the complexity of the pore system, as well as assist in separating the samples into the various rock types.

3.5 Mercury Injection Capillary Pressure (MICP)

The MICP experiments were performed by the Weatherford company using the equipment Autopore IV 9500 (Micromeritics Instruments Co.). The subsamples for these tests were taken from regions adjacent to the plugs used for the other laboratory experiments. Since MICP is a destructive technique, the subsamples submitted to the MICP measurements were selected according to comparative criteria, i.e., samples having similar porosities but different permeabilities, and vice versa. In total, 15 subsamples were chosen.

Based on the assumption that fluid is not able to enter the pore opening of a rock pore network without pressure and that the fluid does not "wet" the pore surface, the MICP tests consist of the gradual injection of mercury using increasing pressures, leading to estimates of the ratio of the capillary pressure of the pores and the volume of fluid injected (SHAFER & NEASHAM, 2000). The experiments begin by enclosing the previously unsaturated sample in a closed container under vacuum, which is then filled with mercury. Starting with atmospheric pressure itself, increasing pressures are subsequently applied to push mercury into the sample. The non-wetting mercury will first invade the larger pores but with increasing pressures slowly move into the entire pore system (Fig. 3.5).

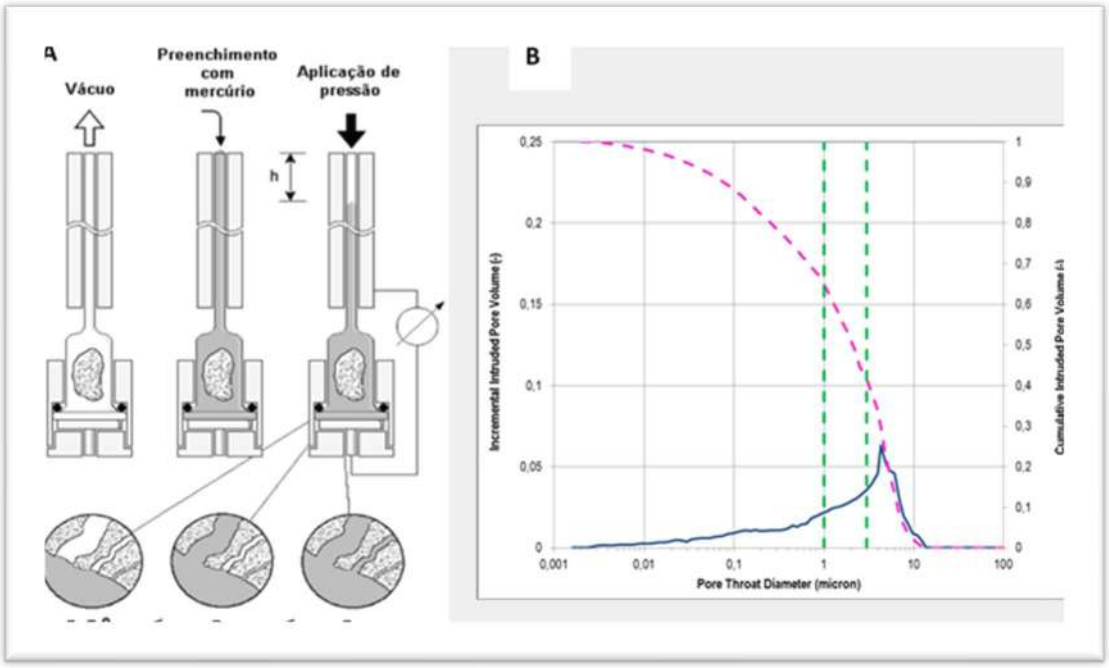

Figure 3-5 - a) Layout of the MICP experiments. b) Plot showing the incremental porosity (blue line), the cumulative porosity (pink dashed line), and the pore size partitions (green dashed line) as a function of the diameter of the pore throats of a sample (LIMA, 2016)

Assuming that the pores can be approximated as equivalent cylinders, it is possible to relate the capillary pressure to the radii of pore throats using the Washburn equation (WASHBURN, 1921) (Eq. 3.2):

$$P_c = \frac{2\sigma |\cos \theta|}{R_t} \qquad (3.2)$$

where P_c is the capillary pressure (dynes/cm²), σ is the surface tension of mercury (480 dynes/cm), θ is the contact angle of the mercury/air interface (140°) and R_t is the radius of the pore throats (μm). Through this transformation one can obtain the distribution of pore throats by the intruded mercury, such as shown by the graphs in Fig. 3.5 (MESQUITA, 2017).

3.6 Integration NMR and MICP

An important application of the NMR and MICP techniques is the integration of its results to determine the surface relaxivity, an essential parameter for calibration of T_2 curves, in order to obtain the pore size distribution (WONG, 1999; FLEURY *et al*., 2016). Considering the pore system of the rock as a bundle of cylindrical capillary tubes of radius

r, the distribution of pore throats determined using MICP can be correlated with the distribution of T_2 by means of the surface relaxativity ($\boldsymbol{\rho_2}$) according to (Eq. 3.3):

$$\left(\frac{S}{V}\right)_{cylinder} = \frac{2\pi rl}{\pi r^2 l} = \frac{2}{r} \qquad \rightarrow \qquad r_{cylinder} = 2\rho_2 T_2 \tag{3.3}$$

where ***l*** is the length of the cylinder. The value 2 holds for cylindrical pores, being necessary to convert the pores in the *S/V* ratio of Eq. (3.3) to pore throat radii, but can be changed to 3 when approximating the pores as equivalent spheres. Thus, once the correlation between the NMR and MICP curves is obtained, $\boldsymbol{\rho_2}$ can be adjusted until the two curves are consistent and the peaks overlap (SOUZA, 2012). The combination of NMR and MICP measurements will not produce good results if no correlation exists between the pore size distributions and corresponding pore throats (MESQUITA *et al*., 2016).

The above methodology to convert T_2 values to pore radii was used for the segmentation of the pores in 3D images. Assuming that the microCT images are acquired with a pixel size of 14μm, the entire region of the pore distribution curve below 7 μm (the pixel radius value) will be considered sub-resolution and cannot be viewed. Therefore, all pores on the curve above this value can be viewed at this resolution. The porosity of the region resolved by the resolution (i.e., the region that can be differentiated from solid rock material), is then equivalent to the total area under the NMR curve, from the pore radius of the imaging resolution until the end of the distribution. Thus, the maximum porosity value that can be seen in microCT images at a given resolution is defined by NMR, which helps to choose the ideal threshold value to calculate the porosity of the image. Figure 3.6 shows the adjustment of the curves as well as the separation between the two regions to be used in the microCT images (red is the visible porosity and blue the sub-resolution porosity).

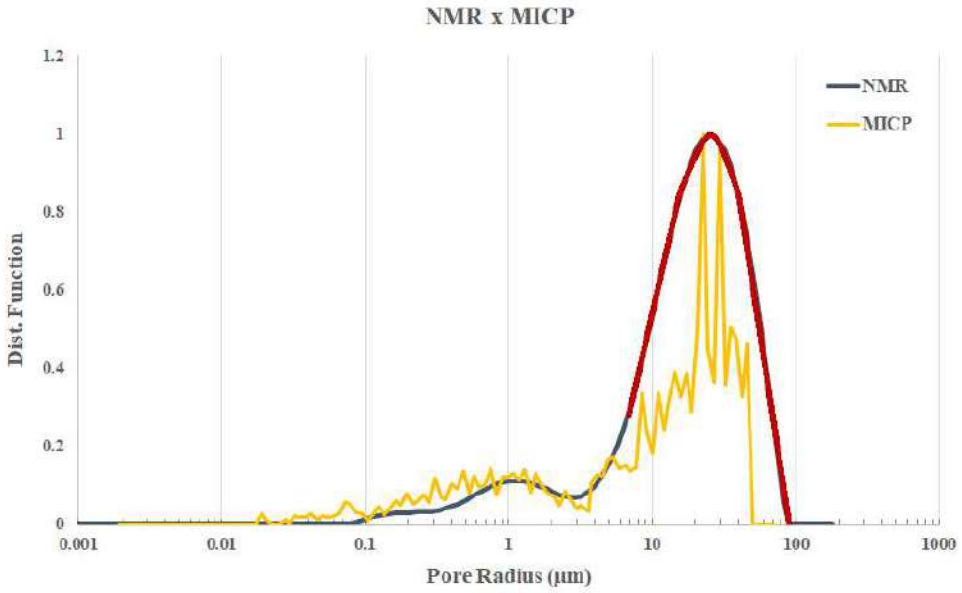

Figure 3-6 - Adjustment of NMR and MICP curves for transforming the relaxation times T_2 into pore radii. The highlighted red part of the NMR curve is for radii above the resolution of the microtomography

3.7 X-Ray Microtomography

The samples were cleaned again after the NMR step, using the Soxhlet method as mentioned in item 3.2, to start the imaging process. For the acquisitions, two tomographs were used: Skyscan model 1173 High Energy (Bruker), belonging to the Nuclear Instrumentation Laboratory (LIN) of the Nuclear Engineering Department, and CoreTOM (Tescan), belonging to the Advanced Oil Recovery Laboratory (LRAP).

Imaging techniques can be of great value in the porous media research field by making it possible to determine the size and shape of the macropores, the topology of the pore distribution (mixing region) and throats (segments connecting the pores), as well as the network of micropores. A limitation of the use of microCT images to represent the pore size distribution is a compromise between sample size and spatial image resolution.

MicroCT scanners provide a non-destructive 3D imaging technology for investigating the internal structure of materials. In the petroleum industry they have been used mainly for studying fluid flow and characterizing rocks (BLUNT *et al.*, 2013). MicroCT imaging techniques allow investigations of the pore structure at scales ranging from micrometers up to a few millimeters. They use the ability of radiation to penetrate materials in varying degrees. The equipment uses a fan-shaped beam geometry to acquire images, which are transmitted X-ray beams coming out of the source, passing through the sample, and being captured by a detector. During acquisition, the sample rotates 360°

with steps of 0.5°. At each step, a transmitted image is acquired and saved in 16-bit files (TIFF extensions). After acquisition, the images are reconstructed using specific software from the manufacturer. Table 3.3 gives the conditions for acquiring images with the equipment.

Table 3-3 – Conditions for the acquisition of microCT images

	Skyscan	**CoreTOM**
Source voltage (kV)	120	160
Current (µA)	66	93
Distance Source - Detector (mm)	364	820
Distance Object - Source (mm)	102.52	76.53
Filter (mm)	Al 1.0	Cu 1.0
Exposure time (ms)	1100	490
Scan duration (hs)	01:08	04:15
Resolution (µm)	14	14
Image extension	TIFF	TIFF

After the acquisition and reconstruction processes, the images were treated using the Avizo 9.5 software (Thermo Fisher Scientific), with the same workflow being applied to all images regardless of the equipment used for imaging. Initially, the pore edges of the images were smoothed for better definition using a non-local means smoothing filter.

The next step was segmentation of the stack of images.The Edit New Label Field tool of Avizo was used to determine the best threshold corresponding to the visible pores for the selected resolution (as explained in section 3.6), immediately followed by segmentation of the images to obtain the percentage of pores present in the sample. After the segmentation process, it is possible to calculate the porosity based on the NMR pore size distribution above the microCT resolution. Although it seems to be a simple and direct process, this phase is the most delicate since it directly impacts the quality of the pore body and pore throat network. Since segmentation is marked by the visible porosity in the imaging resolution given by the NMR technique, visual adjustment is hence still necessary, and very much dependent upon the user experience of the software.

With the segmented pores, the Dilation tool of Avizo is used to dilate the pore space, which helps to connect the pores. The Erosion tool is used next, with the same number of pixels as employed previously, to exclude excess segmentation, leaving only the connections between the pores. In this way, the percentage of pores does not change, and

the pore clusters become connected. The Connected Components tool is applied after dilation/erosion, and the groupings can be determined. After these various steps, the pore space is ready to be transformed into cylindrical tubes (equivalent to the pore throats) and spheres (the pore bodies), using the Autoskeleton tool of Avizo. In addition to presenting the image containing the throats connected to the pore bodies, the Avizo software provides a spreadsheet with the skeleton topology comprising the nodes (connections in the pore bodies), points (pores with location and radius) and segments (throat pores) of the connected clusters. These are the input data used for modeling of the pore network in the porous medium. Figure 3.7 shows the sequence used in the skeletonization process of a coquina sample.

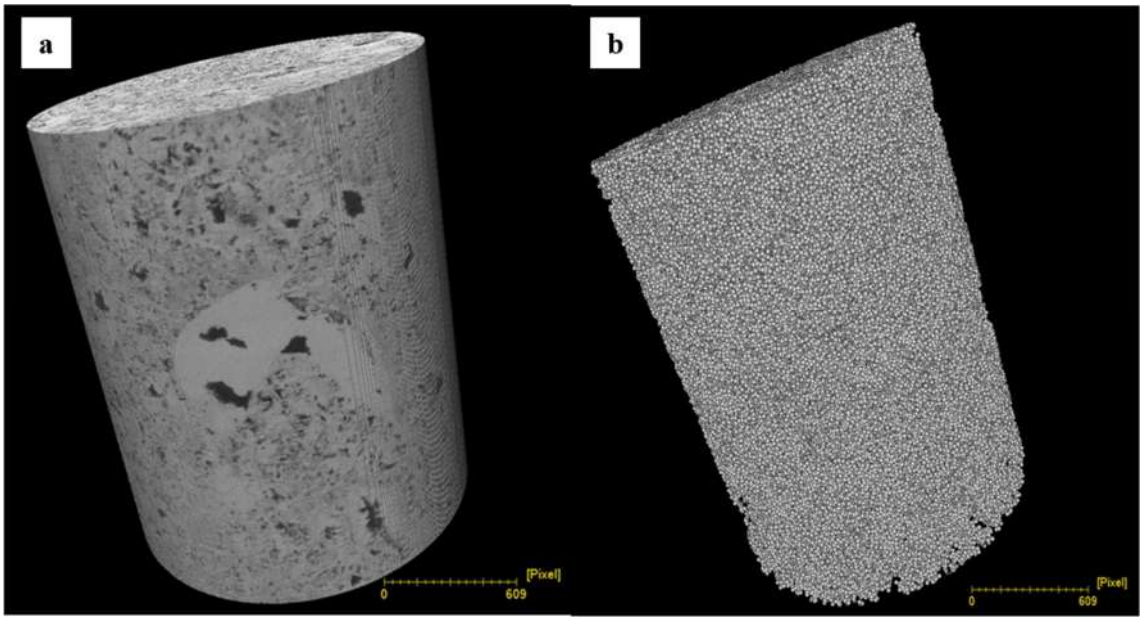

Figure 3-7 – a) MicroCT image from sample 88; b) Skeleton obtained after processing the stack of microCT images using the Avizo software

3.8 Pore Network Modeling

After processing the image stack using the Avizo Fire® software as described in section 3.7, the skeletonization output data were prepared in order to model the pore system using pore network modeling (PNM). The Poreflow pore network model of RAOOF *et al.* (2013) was used for this purpose. PNM has the advantage of accelerating the simulations of water flow and solute transport in the pore systems of relatively large samples, such as for the coquinas in this work. This attribute is often not very viable when using direct numerical solutions, especially for general multiphase flow conditions.

Although the implementation of PNM techniques is not trivial, they can provide a more realistic estimate of different properties of the porous medium. When modeling coquinas, which often have multi-porosity characteristics, it is necessary to add a description of the connectivity between the macro- and micro-porosity domains, which computationally can be challenging. In this research, quasi-static flow modeling was used to calculate the absolute permeability.

In quasi-static single-phase flow, a pressure gradient is established in the pore network between the input and output boundaries of the PNM along the z-axis. The numerical simulations were carried out assuming connectivity between the top and bottom of the sample (the z-axis), being the direction of the experiments with this plug. Flow through a pore throat is assumed to laminar as described with the Hagen-Poiseuille equation:

$$Q_{ij} = g_{ij} (p_j - p_i) \tag{3.4}$$

where Q_{ij} is the volumetric flow rate through the pore throat between two adjacent connected pore bodies, i and j, p_i and p_j are the pressures at the two pore bodies, and g_{ij} is the conductance of the cylindrically shaped pore throat whose value can be obtained using:

$$g_{ij} = \frac{\pi R_{ij}^4}{8 \mu l_{ij}} \tag{3.5}$$

where R_{ij} is the radius of the pore throat that connects pore bodies i and j, μ the dynamic viscosity of the fluid, and l_{ij} the length of the pore throat. For incompressible flow, the continuity equation can be applied to the pore throats as follows:

$$\sum_{j=i}^{N_i} Q_{ij} = 0; \qquad i = 1,2,3, \ldots\ldots, N_i \tag{3.6}$$

where Q_{ij} is the volumetric flow rate within the pore throat going from pore body i to pore body j, and N_i is the coordination number of pore body i. A small differential of pressure was adopted to guarantee laminar flow (low Reynolds number), an important assumption to guarantee laminar flow.

Application of the above equations to the entire pore network leads a linear system of equations with a sparse, symmetric and definite positive coefficient matrix, which can

be solved to obtain the pressures in the individual pore bodies. Considering a well-defined sample, the average velocity of a fluid in the pore network, $\bar{v}$, can be calculated as (RAOOF *et al*., 2013)

$$\bar{v} = \frac{Q_{tot}\, L}{V_f} \tag{3.7}$$

where Q_{tot} is the total flow through the network, which can be determined at the entrance or the exit of the pore network as the sum of all local flows, L is the length of the pore network, and V_f is the total volume of the liquid phase within the network of pores.

The absolute permeability K of the sample is calculated using Darcy's equation:

$$K = \frac{\mu Q_{tot}\, L}{A\, \Delta P} \tag{3.8}$$

where μ is the viscosity of the fluid, ΔP is the pressure differential between the pore network inlet and outlet and A is the cross-sectional area of the pore network. The equations above summarizes the calculations necessary to obtain absolute permeability estimates.

PNM characterizes pore bodies (also called nodes) as the largest elements present in the pore network, and as such represent the largest voids found in natural porous media. The pore throats, which are the narrow openings that connect adjacent pore bodies, are essentially capillary tubes estimated from smaller spherical elements embodying the size and topology as reported in the work of FOUARD *et al*. (2006).

According to RAOOF et al. (2013), PNM has the ability to simulate highly disordered geometries, such as a porous medium, with relatively low computational cost as compared for example to Lattice Boltzmann simulations (SHOLOKHOVA *et al*., 2009). Pore Network Modeling is a promising tool for predicting the multiphase fluid flow and solute transport properties of porous media. When modeling at the pore level, the length of the throats is defined by the distance between two connected pore bodies, while their radii are calculated as a function of the average radii of the spherical elements comprising the path between two pore bodies. To calculate the radii of the pore throats, different averaging methods can be used (notably harmonic, geometric or arithmetic averaging), as well as the minimum radius method, which considers the average radius to be the minimum value found in a pore throat. In this research, the arithmetic mean of the pore radii that make up each throat was used.

The PoreFlow software (RAOOF *et al.*, 2013) was used in this work to model the pore system. It uses multi-directional pore modeling to simulate water flow and solute transport in the pore system. The numerical scheme is based on the assumption that porous media can be represented by a network of pore bodies and throats with finite volume. As described by RAOOF *et al.* (2013), some computational characteristics of the PoreFlow software are:

- The multidirectional pore modeling approach allows a distribution of coordination numbers varying between 1 and 26;
- The natural angularity of the pores is taken into account, with a wide variety of shape factors, such as those for rectangular and circular pores, in addition to several irregular triangular cross-sections;
- The pore bodies and pore throats have volumes, allowing mass balance equations, mass flows and solute concentrations to be applied to the pore bodies and throats;
- Various parameters and relationships can be computed, among them: capillary pressure curve - saturation (P_c x S_w) curves, relative permeability curves, interfacial area, solute dispersivities (saturated and effective diffusion coefficients), tortuosities, and percolation properties.

Resulst of modeling the pore network of the coquinas using the PoreFlow software include not only absolute permeability, but other data such as digital porosity of the samples and the flow length in the coquina pore network. The program provides numerical output results as well as 3D graphical representations, which can be viewed by other software.

The Paraview 5.3.0 software (AYACHIT, 2015) was used to check the pore connections in the system, thus visualizing the main clusters of the samples. This software is an open code, allowing the visualization and analysis of extremely large data sets. The program uses parallel data processing and rendering to allow interactive visualization of the data. Input data consists of vtk extension files (visualization toolkits), which provide dorsal spirals of the visualization and processing of data files generated after modeling using the PoreFlow software.

3.9 Thin Section Petrography

Microscopic characterization was performed using thin sections made at the Solintec company in Rio de Janeiro. Standard size slices (4.5 x 2.5 cm) were made from cross-sections of the plugs (Fig. 3.8). They were impregnated with blue epoxy resin to fill the pores of the rock, thereby highlighting and facilitating the interpretation of the types of pores and mineralogy. A Zeiss optical microscope, model Axio Imager 2 under polarized light, was used for the analysis, carried out at the Sedimentary Geology Laboratory of UFRJ.

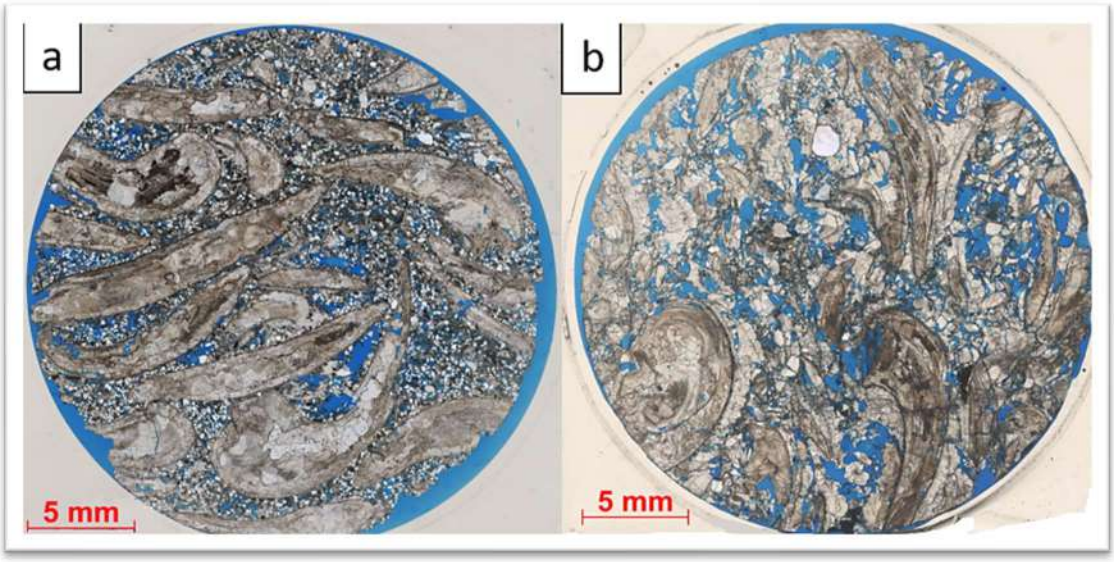

Figure 3-8 - Petrographic thin-sections of sample 87.35 (a), and sample 90.95 (b). The pore space is highlighted by the blue epoxy resin.

Pore space can be created, modified, or destroyed at many stages during the formation of carbonate rocks. The pore system is generally complex from both a petrophysical as well as a genetic point of view. If formed during deposition and modified due to diagenesis, sometimes the resulting system may resemble a well-selected sandstone. This change represents an unusual physical and genetic simplification of carbonates since complexity is the rule for these rocks.

The classification of pores within the thin slices used in this research is facilitated by using the nomenclature of CHOQUETTE & PRAY (1970). Their classification employs geological concepts concerning the carbonate pore space, while also emphasizing the importance of pore genesis. The classification is based on a relationship between the various constituents of the rocks: when a dependency exists between the pores and the particles (i.e., the grains or debris), the rock fabric is referred to as having

a selective weave, and when it is not possible to establish a dependency, the weave is non-selective. Primary pores formed during deposition of sediments usually have a selective weave, while secondary pores formed after deposition, often due to the effect of diagenesis, have a more non-selective weave. Figure 3.9 summarizes the classification proposed by CHOQUETTE & PRAY (1970).

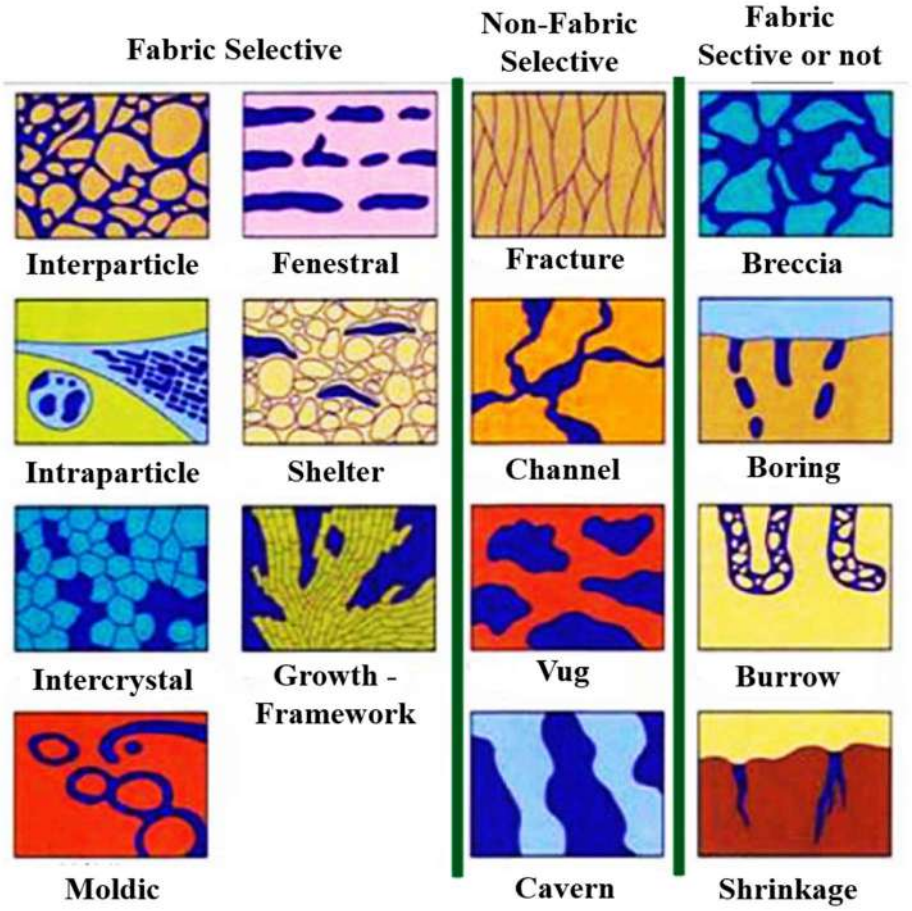

Figure 3-9 – Pore classifications by CHOQUETTE & PRAY (1970) as used in this research

3.10 X-Ray Difraction

The mass percentage of all minerals present in 11 of the samples that were used was determined using X-ray diffraction. The analysis was carried out on sub-samples from regions adjacent to the plugs. Sample preparation was carried out at the Centro Tecnológico Mineral (CETEM) in Rio de Janeiro. The following protocols were followed for sample preparation prior to X-ray diffraction: 10 grams of each sample were grounded in a Fritsch Pulverisette 6 planetary mill, with a pan and agate spheres of 10, 20 and 30 mm diameter, at a speed rotation of 300 rpm for 1 minute, or until the entire sample had passed through a 106 micrometer sieve.

After quartering in a Quantachrome rotary quartz, a representative aliquot of 3 grams of the sample was pulverized in a McCrone mill containing 15 ml of deionized water in a plastic jar, with the mixture being ground with an agate cylinder of 1cm diameter for 10 minutes. This procedutre was applied to avoid loss of crystallinity of the minerals by overflow. After this process, the sample was dried in an oven at 60° C for 24 hours in a Teflon Petri plate. The dried sample was disaggregated using an agate mortar and mounted on a backload support for analysis by X-ray diffraction.

The samples were next analyzed through of a Bruker-D4 Endeavor diffractometer using the following operating conditions: a Cu Kα sealed tube (λ = 0.179021 nm), a generator operated at 40 kV and 40 mA, goniometer speed of 0.01° 2θ step with counting time of 0.5 sec per step, and collected from 4° to 90° 2θ, with a LynxEye position-sensitive detector. After carrying out the experiment, the spectra needed to be interpreted. This was done by making comparisons of the obtained spectra with standards contained in the PDF database (ICDD, 2019) using the Bruker Diffrac EVA 5.0 software. The mineral phases were subsequently quantified in terms of fundamental parameters (CHEARY & COELHO, 1992) by using the software DIFFRAC.TOPAS version 5.0 from Bruker-AXS based on the Rietveld refinement method.

3.11 Principal Component Analysis

To better understand the influence of the pore size of samples within given rock types, a multivariate Principal Component Analysis (PCA) was carried out. PCA is a dimensionality-reduction method often used to reduce the dimensionality of large data sets by transforming a large set of variables into a smaller number that still contains most of the information in the larger set, with minimum loss of information (WOLD, 1996). By reducing the size of the data set and eliminating overlaps, existing patterns are more easily viewed and identified. PCA is a data exploration analysis useful for identifying clusters and for classifying eventual information from the samples. This is especially useful when the feature vectors are multi-dimensional, and it is not possible to represent the original data in graphical form.

The first step of a PCA is to standardize the data by making them dimensionless. The aim of this step is to standardize the range of the continuous initial variables so that each one contributes equally to the analysis. This procedure is widely used when working with data sets that vary in scales having very different amplitudes. Standardization prior

to PCA is critical since the analysis is quite sensitive regarding the variances of the initial variables. If there are large differences in the ranges of the initial variables, then those variables with the larger ranges would have dominated those having smaller ranges. Mathematically, the standardization was accomplished by subtracting the mean of each variable from each measured value and dividing by the standard deviation. With this standardization, the new values found for each variable become dimensionless. In this work the T_2 distributions of the samples were used as variables.

The software PAST® (Paleontological Statistics) (HAMMER *et al.*, 2001) was used to analyze dimensionless data. As a product of PCA, a new set of variables called the principal components (PC) is calculated, which are formed by a linear combination of the original variables (MCKENZIE *et al*., 2011). According to GOTELLI & ELLISON (2011), the new variables (PC) can be ordered based on the amount of variation that was present in the original data. The covariance matrix computational step is then used to understand how much the variables of the input data set differ from the mean with respect to each other (i.e., to see if there is any relationship between them). In order to identify these correlations, the covariance matrix is computed, and the sign of the covariance identified: if positive this means that the two variables increase or decrease simultaneously (i.e., are correlated); if negative, one increases when the other decreases (inversely correlated).

PC are new variables that are constructed as linear combinations or mixtures of the initial variables (GOMES, 2014). The combinations are achieved such that the new variables (i.e., the principal components) are uncorrelated, with most of the information within the initial variables being compressed into the first components. The idea is to convert n-dimensional data into n PCs, with PCA trying to place maximum possible information into the first component, then optimizing the remaining information in the second component, and so on. At this point, the eigenvectors are computed and ordered by their eigenvalues in descending order, leading to a set of principal components in decreasing order of significance.

A PCA allows one to reduce the dimensionality without losing much information, notably by discarding the components with low information and considering the remaining components as the new variables. The initial PCs have the biggest variation, but during interpretation of the data they can be combined with all other components to find the best match of the dataset. The analysis may be used to cluster the samples of each rock type, leading to a better understanding of certain petrophysical properties.

After determining the PCs, it is possible to build graphs that allow one to identify outliers and facilitate the interpretation of patterns in the samples, such as similarities, differences and groupings. The results of a PCA are usually discussed in terms of component scores (the transformed variable values corresponding to a given data point), and loadings (the weight by which each original standardized variable should be multiplied to get the component score). To understand the results of a score graph (Fig. 3.10), it is necessary to compare the graph with a loading graph showing the contribution of each variable.

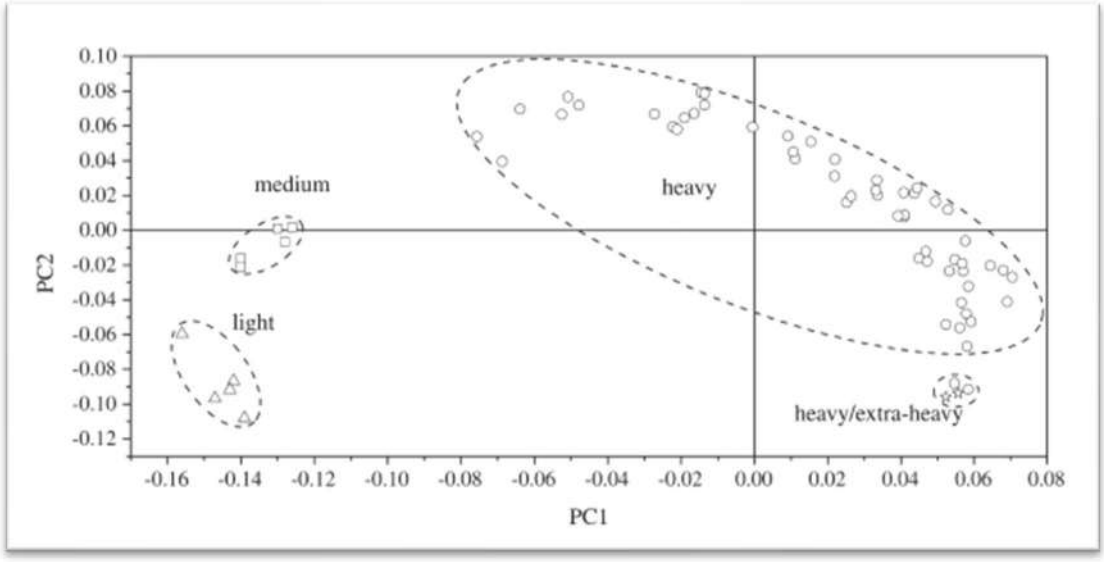

Figure 3-10 - Score graph showing the results of a PC1xPC2 analysis. The graph shows the clustering of crude oil samples having different viscosities, based on T_2 relaxation data (from RAMOS *et al*., 2009)

4 RESULTS AND DISCUSSIONS

This chapter contains results obtained using the techniques described in Chapter 3 (Materials and Methods) and the research workflow (Chapter 1). Results are discussed, including how complementary techniques were used to understand variability within similar rock types. First presented are the measurement methods that were applied to all samples (routine core analysis and NMR) and how the various rock types were defined. Available samples were divided into rock types, while identifying samples that deviated in some manner from others of the same rock type. For this purpose, various analyses were performed (such as analyses of the mineralogy components, and the use of thin sections and X-ray diffraction), to confirm similarities among the samples and to better understand the deviations. After characterizing the rock types, other techniques were used (MICP, microCT, and pore scale modeling) to better understand the variability in porosity and permeability, as well as to study the effects of connectivity on fluid flow within the pore system. A complete analysis of the entire data set for each rock type, as described in the flowchart of Fig.1.1, showed which information was important for characterizing the rock clusters, and for optimizing possible equations to predict the permeability.

4.1 Petrophysics

All samples were analyzed using routine core analysis and nuclear magnetic resonance (NMR). Table 4.1 shows the main results for grain density, porosity (ϕ) and permeability (k). The routine petrophysics data were obtained at the beginning of pore system studies. Also displayed in Table 4.1 are porosity values acquired through NMR.

Table 4-1 – Results from the routine core analysis and the NMR measurements of the samples

Samples (m)	Grain Dens. (g/cm³)	Φ_{Rout} (%)	K_{Rout} (mD)	Φ_{NMR} (%)
66.35	2.70	19.1	93.1	18.4
68.65	2.69	18.2	117.6	18
71.30	2.72	24.7	152.9	24.4
73.20	2.71	18.2	70.7	17.7
80	2.71	16.3	24.1	15.4
80.95	2.71	19.6	504.4	17.5
82.05	2.71	19.4	179.5	17
83.05	2.70	18.6	568.4	17.7
83.65	2.71	17.4	388.2	16
87.35	2.70	10.2	5.3	9.6
88	2.71	8.70	5.2	9.0
90.95	2.71	15.2	428.5	13.7
93.00	2.71	19.8	232.9	17.9
94.40	2.70	18.5	103.5	17.9
98.55	2.71	18.4	649.9	18.0
99.50	2.70	24.9	84.0	24.6
100.7	2.71	16.3	227.7	15.9
102.55	2.71	18.8	174.1	18.1
105.30	2.71	9.7	2.7	10.2
113.7	2.70	8.7	0.4	8.9
122.45	2.72	12.2	5.7	12.1
126.05	2.71	11.5	13.0	11.2
128.05	2.70	12.1	22.1	13.6
132.15	2.71	11.3	10.6	10.5
133.90	2.72	13.3	17.3	13.0
136.85	2.71	15.9	244.9	15.1
140.80	2.71	7.0	1.8	7.6
141	2.71	11.8	4.3	11.1

Samples (m)	Grain Dens. (g/cm³)	Φ_{Rout} (%)	K_{Rout} (mD)	Φ_{NMR} (%)
143.25	2.70	8.4	1.3	8.9
146.25	2.71	4.0	0.04	4.4
148	2.71	6.1	0.2	6.2
151.15	2.70	10.6	0.98	10.0
154.20	2.70	16.6	77.2	16.2
156.50	2.70	14.1	258.5	13.6
160.10	2.70	13.4	144.9	13.1
162.50	2.71	17.5	121.9	17.6
169.45	2.71	7.8	0.2	8.0
170.65	2.68	20.2	366.7	20.1
173.50	2.71	10.8	5.2	11.0
176.85	2.72	9.9	1.5	9.1
180	2.71	16.8	245.1	16.3
184.95	2.72	11.1	63.6	11.2
187.95	2.70	12.2	152.4	12.4
189.40	2.70	15.1	273.7	15.2

The data in Table 4.1 show that the samples exhibited much variability in terms of both porosity (4% - 24%) and permeability (0.04mD - 649mD). The grain density data reflect the predominance of calcite in the mineralogical composition of the rocks (in general, 2.71g/cm³), with only two samples (68.65 and 170.65) having a slightly lower density (2.69 and 2.68 g/cm³, respectively).

As reported by LIMA *et al*. (2020), routine core analysis is important because it provides information for calibrating other investigative techniques in petrophysics. For example, Fig. 4.1 shows a graph that was generated for NMR and routine porosities values of the samples used in this research ($R^2 = 0.9791$). The values are not expected to be same but should have errors of less than approximately ± 2 p.u. (SOUZA, 2012). The NMR experiments hence showed good quality and can be used as a comparative parameter for the same type of rock. One advantage of NMR is that this method also gives estimates of the pore size distribution curve of the rocks. Once the samples have a saturation index above 95%, graphs can be generated of the pore size distribution from the transverse

relaxation time distribution curve (T_2), which will then show the heterogeneity of the samples being studied.

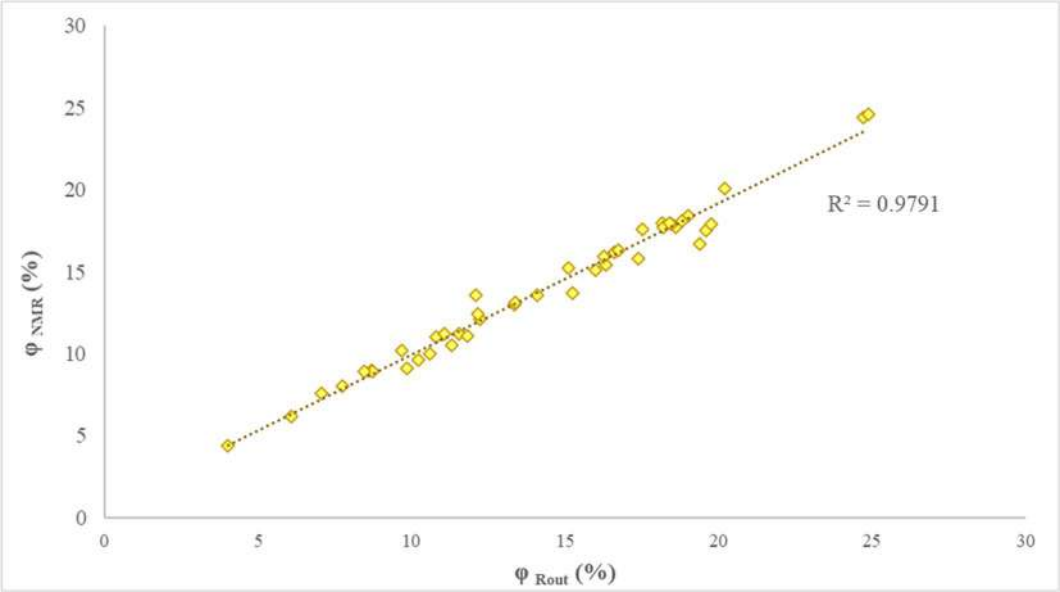

Figure 4-1 – Routine core analysis porosity versus NMR porosity

Fig. 4.2 shows variations in the pore size according to their T_2 relaxation times. For the partitioning of pore sizes, we used to scheme proposed by SILVA *et al*. (2015). The heterogeneity is well evidenced by the variation of pore families within the sample database, thus reinforcing the idea of separating the pore sizes into five partitions: up to 1ms would be considered micropores; between 1 - 10ms is a transition region between micro- and mesopores; 10 - 100ms would correspond to mesopores; 100 - 1000ms is a new transition zone between meso- and macropores; and, finally, the region above 1000ms dominated by macropores. However, as highlighted by SILVA *et al*. (2015), it is not surprising that most bins of the T_2 spectrum effectively contribute to the permeability of the system. This because carbonate rocks samples are composed by pores that can vary by up to three orders of magnitude.

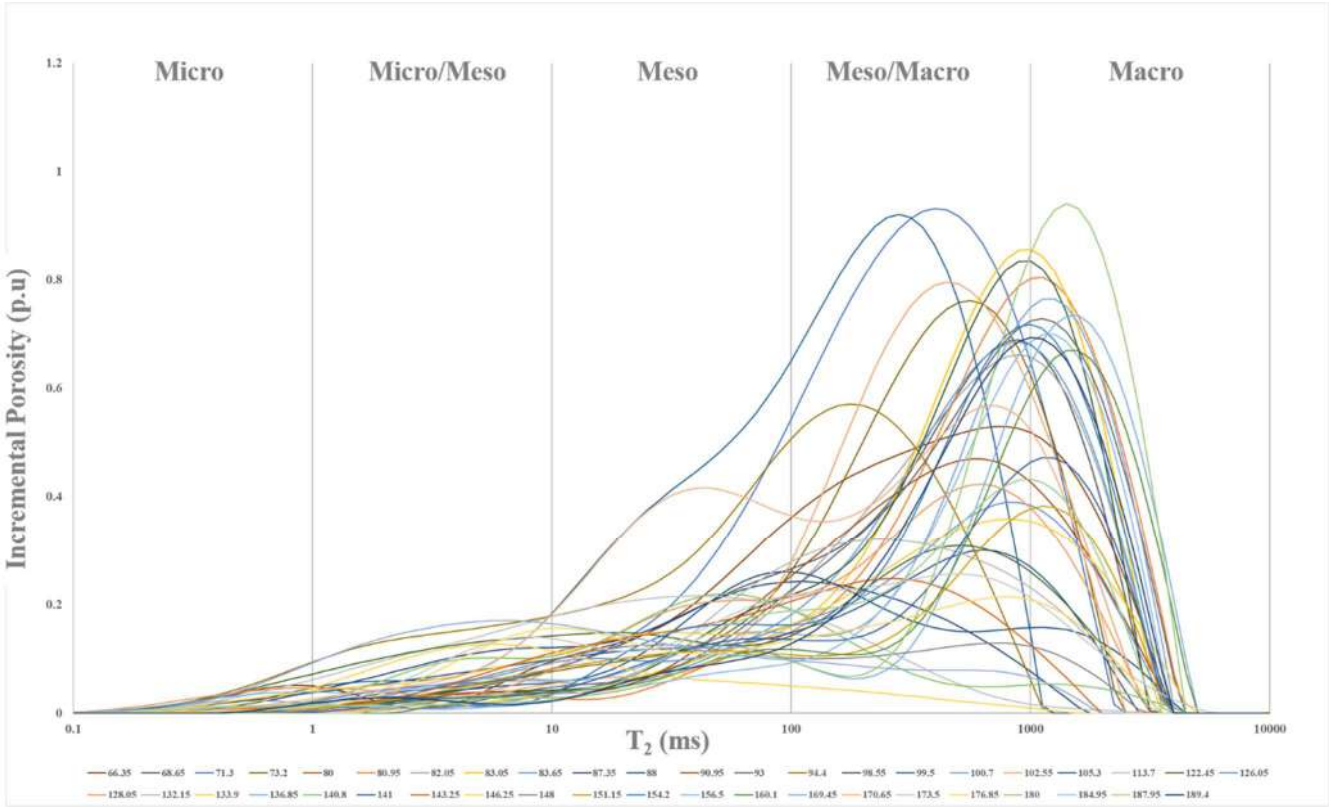

Figure 4-2 – Plot showing T_2 distributions and the pore size partitioning of all samples used. The wide range of the curves reflect the considerable heterogeneity of the pores

The samples in this study were separated into groups, called rock types, in order to understand how pore size influences the permeability, as well as to estimate permeability using the results obtained with the NMR and MICP techniques. The various rock types are discussed next.

4.2 Rock Types (RT)

A graph of porosity versus permeability was generated using the routine core analysis data, in attempts to optimally group the samples into different rock types (Fig. 4.3). In this graph the samples were separated into rock types within certain permeability ranges. Rock type 1 (RT1) was used to group samples having the lowest permeabilities of the whole set, between 0.04 to 5.65 mD; followed by RT2 having permeability values ranging from 10.57 to 93.04 mD; RT3 with values from 144.88 to 649.91 mD; RT4 showing values from 103.49 to 366.68 mD; and finally the RT5 showing values of 84.04 and 152.96 mD.

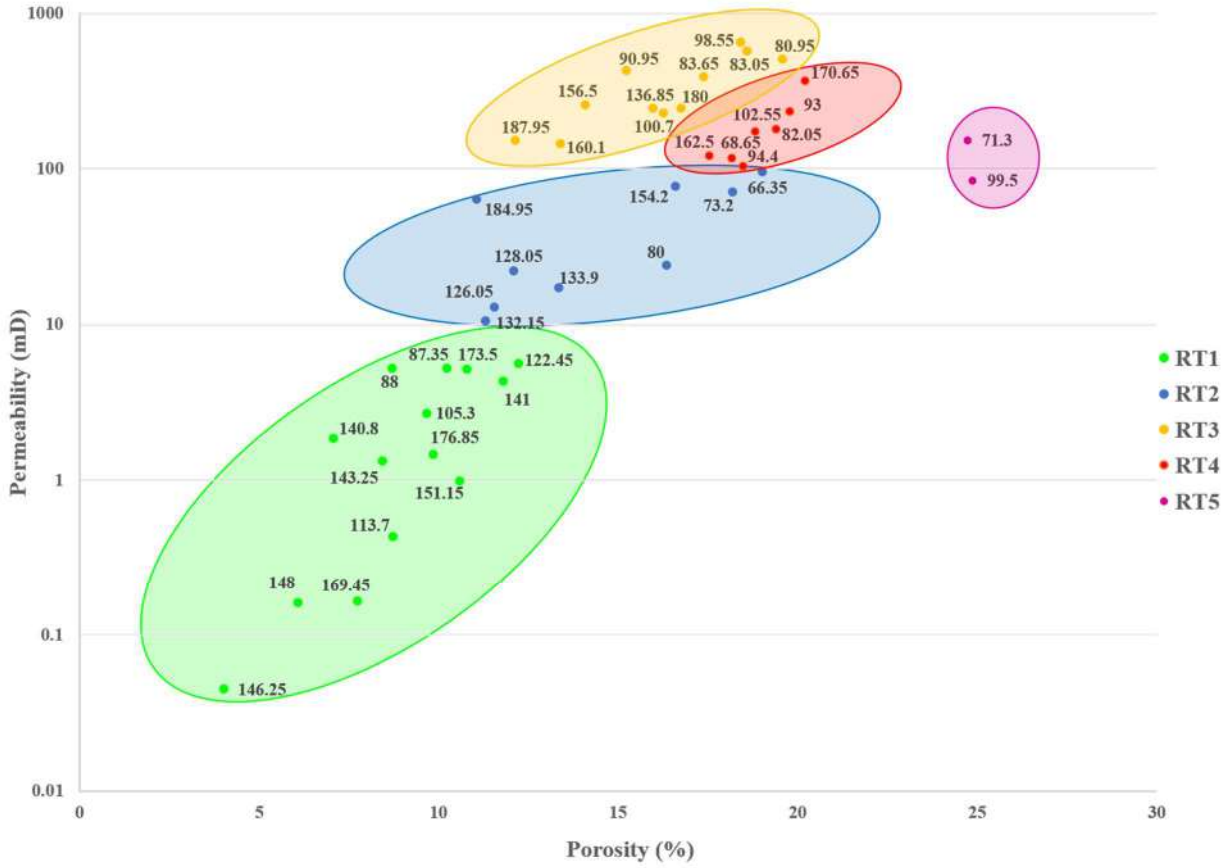

Figure 4-3 – Plot showing the rock types based on porosity and permeability as derived from routine core analysis. Rock types are separated by colors: RT1 in green, RT2 in blue, RT3 in yellow, RT4 in red and RT5 in pink

One important aspect of the results in Fig. 4.3 is that the progressive increase in permeability is not followed by a similar increase in porosity. For example, the RT2 and RT3 groupings show that the porosity ranges are quite similar, while the permeabilities diverge much more. This is a recurring characteristic of coquina pore systems and reinforces the finding that samples, even with similar porosities and sometimes taken from similar depths, can have different fluid flow properties. This shows the importance to understand the complex pore systems of coquinas.

As previously mentioned, the first confirmation of similarities between samples in the same cluster was based on the T_2 distributions showing similar shapes of the curves, the distribution of the pore sizes and the average relaxation times. However, samples in some cases showed differences when comparing their T_2 shape to others within the group, thus requiring complementary analyses. Instead of having only three rock types (e.g., low, medium and high permeability), subdivisions were created within the highest permeability range. For this, not only the permeability but also the NMR distribution

curve and the petrophysical and petrographic characteristics of the samples were taken into account. This notion is based on conclusions by CORBETT *et al*. (2016) who found that the diagenesis of a rock formation can dramatically change the permeability with small variations in porosity. Their research suggests a need for additional studies to better understand the formation as such, to analyze 3D images for better interpretation of the interconnectivity of the pores, and to create subdivisions of petrophysical rock types.

Auxiliary methods used in this research to improve the characterization of samples are multivariate statistical principal component analysis (PCA), description of thin sections (focusing on the mineralogy and morphology of pores and shells) and X-ray diffraction (XRD) for mineralogical determination and quantification, to improve the characterization of the samples. The groupings with their main characteristics are presented below.

4.2.1 Characteristics of Rock Type 1 (RT1)

As shown in Fig. 4.3, RT1 groups samples having the lowest permeability of the entire set. Table 4.2 shows its main petrophysical characteristics, as well as the most relevant geological details of RT1, such as the fragmentation percentages of shells and siliciclastic minerals, quantification of the main minerals by X-ray diffraction as well as classification of the pores according to CHOQUETTE & PRAY (1970).

Table 4-2 – Petrophysical and geological properties of Rock Type 1

Sample (m)	Φ_{Rout} (%)	K_{Rout} (mD)	$T_{2Logmean}$ (ms)	Shells fragm. (%)	Silicic Min. (%)	Pore Classif.	XRD Calcite	XRD Qtz
87.35	10.2	5.3	50.9	20	40	Interparticle (90%)	83%	14%
88	8.7	5.2	133.0	40	5	Interparticle (65%)	-	-
105.3	9.7	2.7	111.6	70	18	Intraparticle (35%) Moldic (35%)	95.6%	3,6%
113.7	8.7	0.4	23.3	70	45	Interparticle (50%)	69%	26%
122.45	12.2	5.6	75.4	-	-	Intraparticle (50%)	-	-
140.8	7.1	1.8	41.8	5	12	Vug (40%) intercrystaline (35%)	-	-
141	11.8	4.3	354.0	15	1	Vug (60%)	-	-
143.25	8.4	1.3	17.7	8	15	Intercrystaline (35%) interparticle (35%)	-	-
146.25	4.0	0.04	11.5	-	8	Intraparticle (20%)	-	-
148	6.1	0.2	83.1	5	1	Vug (75%)	-	-
151.15	10.6	0.98	247.7	3	-	Intraparticle (50%)	-	-
169.45	7.7	0.2	17.7	95	5	Intrapartícle (25%)	-	-
173.50	10.8	5.2	102.5	2	5	Interparticle (35%) Vug (25%)	-	-
176.85	10.8	1.5	98.7	15	4	Vug (60%)	-	-

As can be seen in Table 4.3, the samples that make up RT1 have low porosities, between 4 - 12%, permeabilities between 0.04 - 5.65 mD and relatively low average relaxation times ($T_{2Logmean}$), consistent with samples that are predominantly composed of small pores. Fig. 4.4 shows the pore size distributions of the samples in this set.

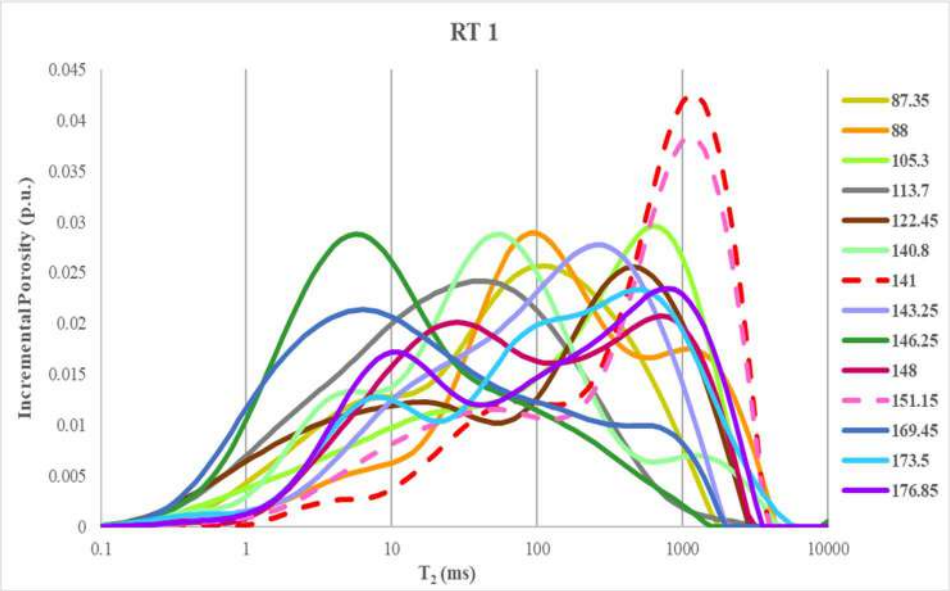

Figure 4-4 – Plots of the multimodal T_2 distributions for RT1 samples. The curves for samples 141 and 151.15 are dashed to show their differences with the other curves

Since the T_2 times reflect the pore size distributions (RIOS *et al*., 2014), with the curves normalized in terms of total area, they clearly indicate that the samples have bimodal and trimodal distributions, with most of the $T_{2Logmean}$ situated between 11.5ms and 133.04ms. The curves highlight the diversity of the pore sizes in this cluster, even though they have similar porosities (i.e., no predominance of a certain range of pores). However, two samples stand out by showing sharp peaks in the macroporosity region: samples 141 and 151.15 have much higher $T_{2Logmean}$ averages as compared to the others (i.e., 354.02 and 247.74 ms respectively).

Since no preferential shape of the T_2 curves was apparent among the samples of the same rock type, a need exists to find similarities between them from another point of view. A promising tool for studying the influence of pore size on the hydraulic conductivity of this rock type is multivariate statistical PCA. This method is used here to find which pore size range influences the grouping the most, thus confirming its similarities. The PCA technique was applied to 44 samples to obtain scores of the bins obtained as a result of NMR. Fig. 4.5 shows a graph of scores for these variables for the entire sample set, with the samples of rock type RT1 identified in green.

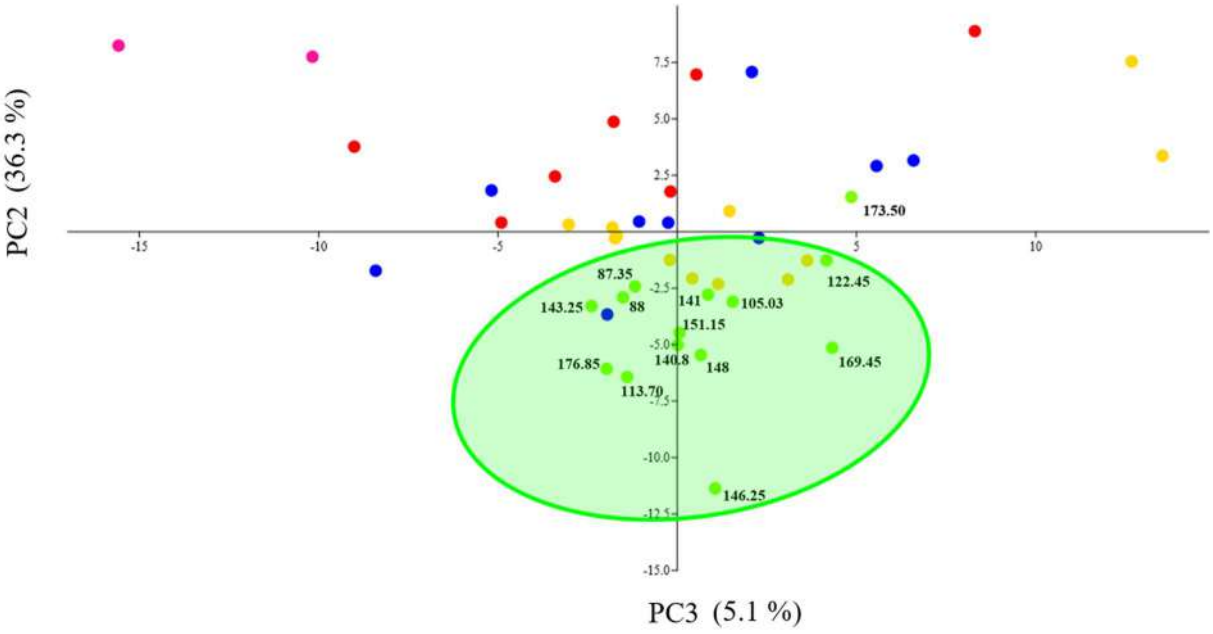

Figure 4-5 – Plot showing scores for all samples. Most of the RT1 samples (highlighted in green) are concentrated along the negative PC2 axis

The graph containing the PC3 versus PC2 scores shows that most of the samples contained in RT1 are clustered around the negative axis of PC2, with only the 173.5 being outside that region. To interpret the positioning of the samples, one needs the loadings graphs of the principal components. Each principal component describes a linear combination of the original variables, with the contribution of each variable being displayed in the loadings graph. Initially, the PC2 graph was examined to provide a better overview of all available samples (Fig. 4.6).

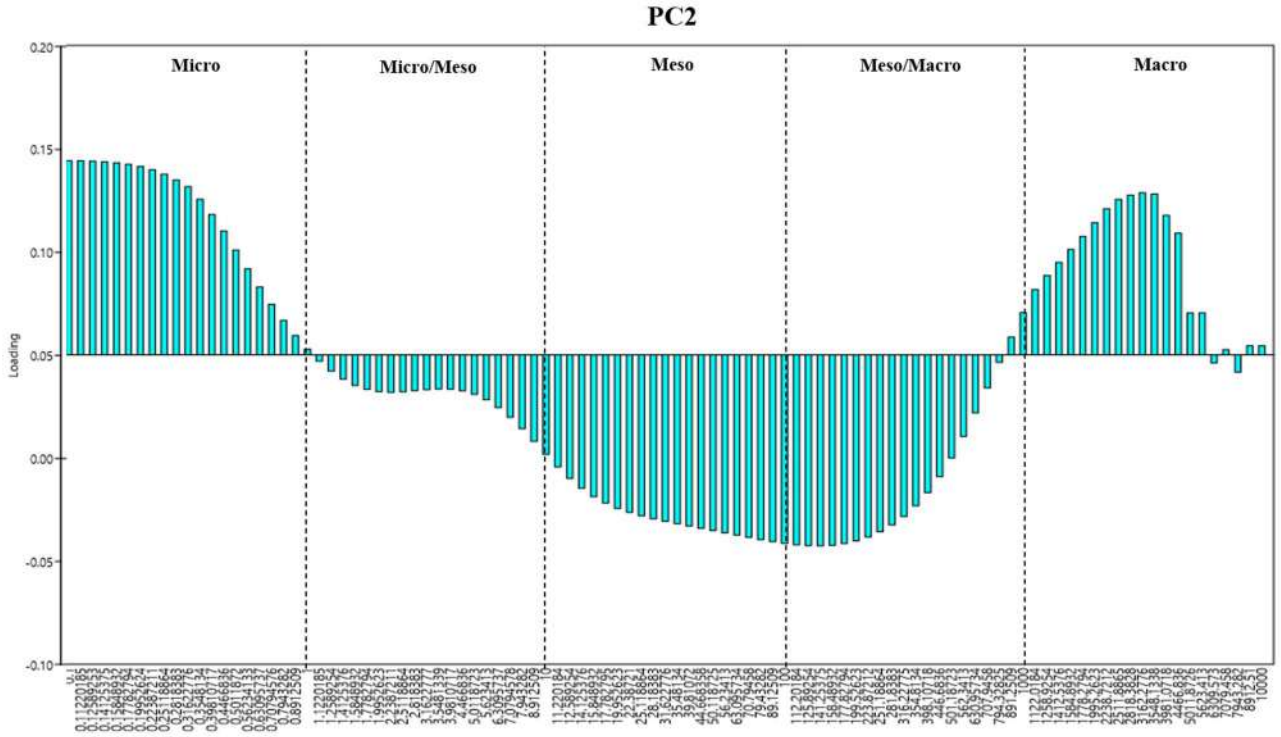

Figure 4-6 – PC2 loading plot showing the contributions in each pore size partitioning

The graph of scores (Fig. 4.5) indicates that the samples of rock type RT1 are concentrated in the negative region of PC2. Interpreting this information through the loadings graph of this component (Fig. 4.6), the high negatives correspond to relaxation times between 10 and 100 ms (the region of mesopores) principally. This affirms that this partition has more influence on the grouping, and consequently contributes more to fluid flow in the pore system. The result of this analysis is confirmed by SILVA *et al*. (2015), who showed that the micropores of carbonate rocks do not contribute as much to the permeability as do the larger pores. One hence may conclude that, even though there is no clear correspondence in the T_2 curves, the PCA technique was able to find similarities between the samples within the cluster.

Another principal component may be used for sample 173.50, whose position differed from the others. In the graph of scores (Fig. 4.5), this sample is located on the positive axis of PC3. The interpretation of the PC3 loadings graph was examined (Fig. 4.7). The PC3 graph shows that the high positives are, mainly, in the micro region (0.1 to 1ms) and in the meso/macropore hybrid region (approximately 100 – 1000 ms) principally.

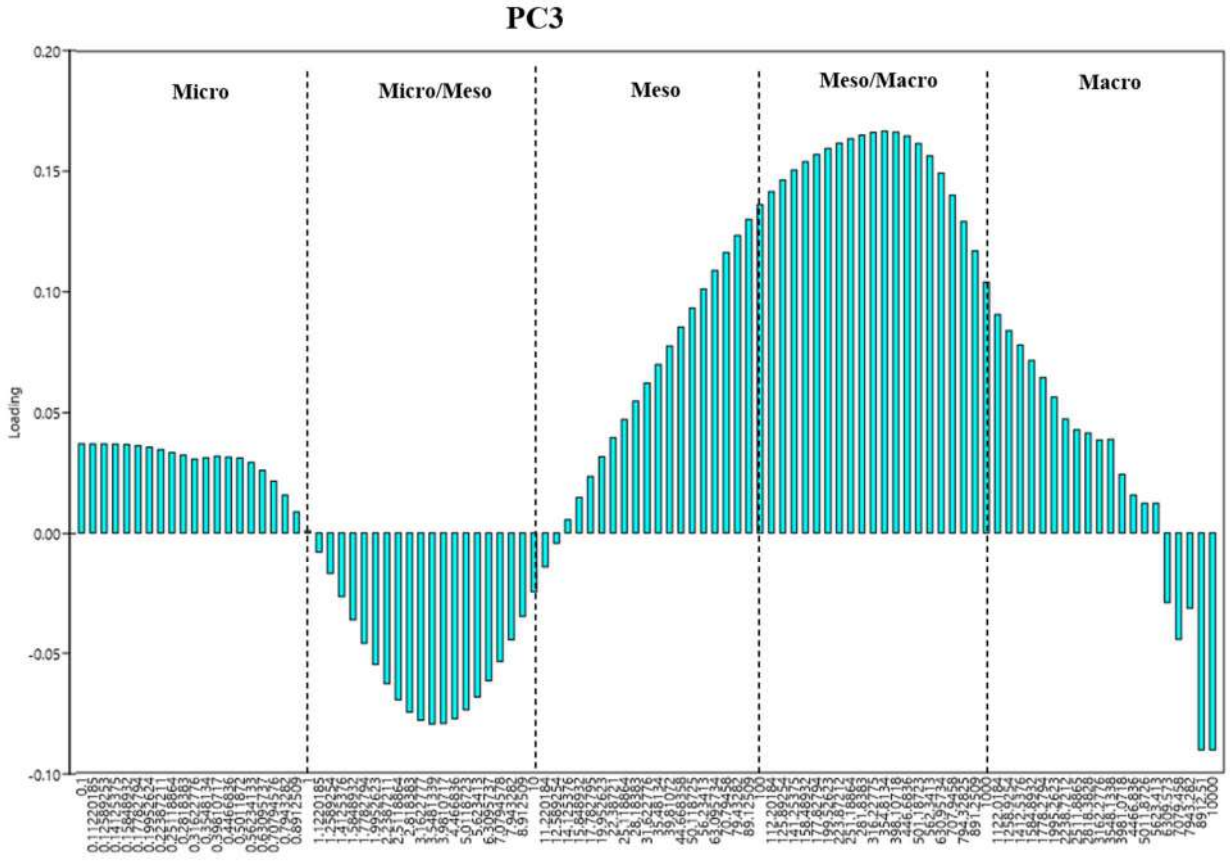

Figure 4-7 – PC3 loading plot showing the contributions of each partitions of pore size

The above example shows that PCA techniques make it possible to verify that for the samples of this study, even with their different NMR curves, the mesoporosity pore partition mostly influences flow in the RT1 group. This result makes it possible to separate the samples into groups according to their relaxation peaks. It allows the identification of samples that show peak relaxations within the most influential region of RT1, and to separate the other samples that show peak relaxations in the regions of least influence. For this reason, the curves are separated into the three groups shown in Fig. 4.8.

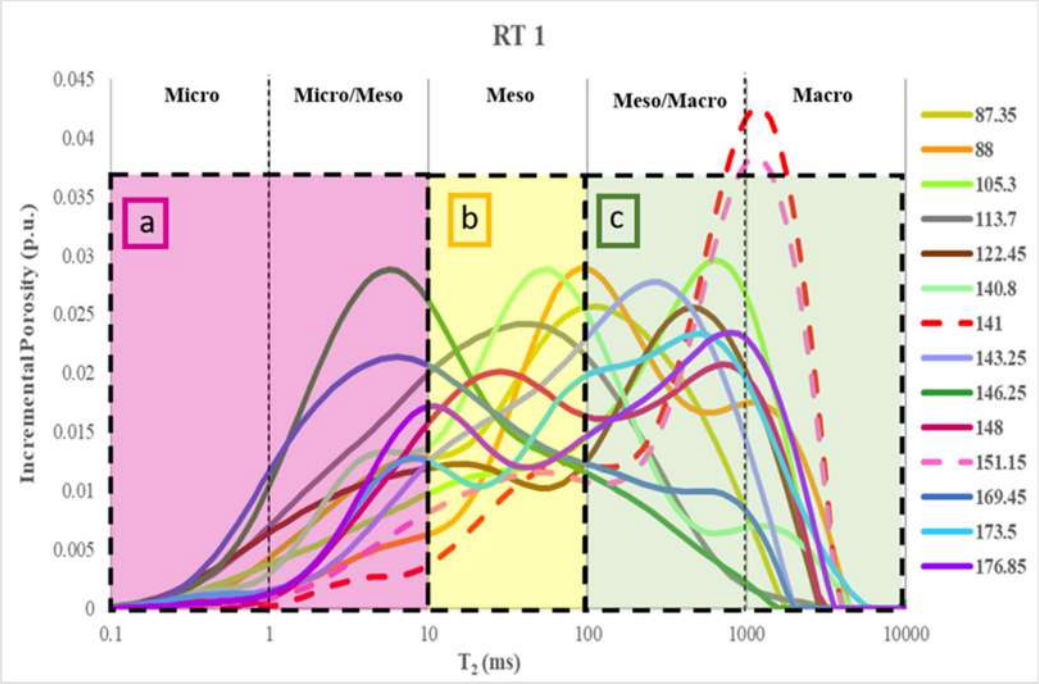

Figure 4-8 – Plot showing T_2 distributions curves for RT1 samples. From the PCA, the NMR plot was separated according to regions of influence for flow in the samples, being: a) samples that showed peaks in the region of least influence; b) samples that show relaxation peaks in the region of greatest influence; c) samples showing peak relaxation in the region of least influence

The contribution of multivariate statistics was critical to understand the influence of pore size partitioning on the conductivity of the RT1 samples. Initially, the heterogeneity of the samples was observed from the T_2 curves, without identifying a region where the relaxation peaks were concentrated. With the use of the bins resulting from the NMR, the PCA technique was applied, thereby making it possible to create separations between the samples according to the importance of their predominant pores.

Fig. 4.8 highlights three regions: a pink region (a) containing samples 146.25 and 169.45, with relaxation peaks between 0.1 - 10ms, below the region of greatest influence; a yellow region (b) containing samples 87.35, 88, 113.7, 140.8 and 148, that show a relaxation peak between 10 - 100ms, with the greatest influence within the cluster; and a green region (c) composed of samples 105.3, 122.45, 141, 143.25, 148, 151.15, 173.5 and 176.85 whose peak relaxation occur above the region of greatest influence (above 100ms).

It is important to note that sample 148 has peaks in two partitions due to the bimodal distribution with two very similar peaks. This is yet another example of the difficulty in diagnosing similarities between the samples. Another finding is the presence of two samples with relaxation peaks at the threshold of regions *b* and *c* (samples 87.35

and 88). These separations made it possible to determine which samples has a more homogeneous pore system, with similarities between them explained by analysis of their petrographic characteristics. The petrographic interpretation was made using thin sections of the rock samples, with as aim to identify some geological factors that could have caused the similarities and differences.

To better assess the rocks and resolve doubts, their geological aspects were evaluated to highlight some of the properties that impact porosity and permeability, notably shell fragmentation, mineralogy and pore types. After petrographic analysis, similarities were found between samples from each region in terms of shell fragmentation pattern, pore morphology, and other geological aspects. To illustrate these aspects, Fig. 4.9 shows thin sections of samples that dominated in each the three regions identified in Fig. 4.8.

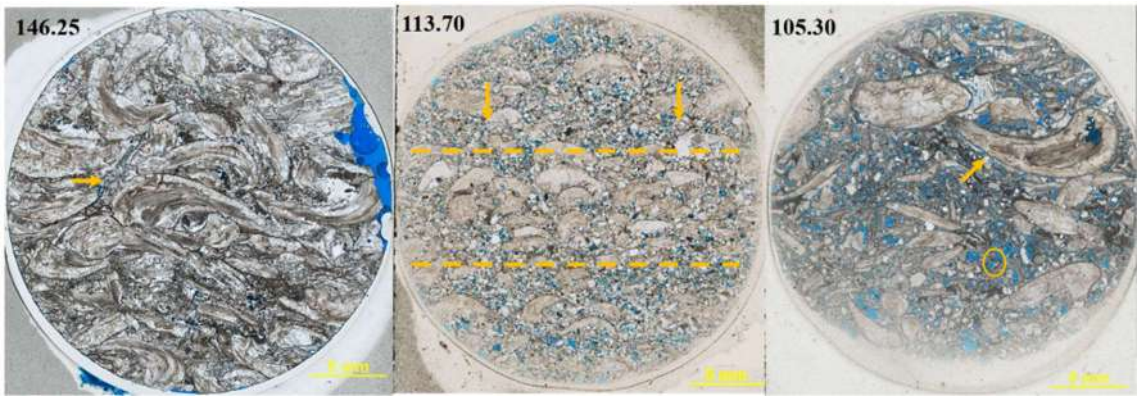

Figure 4-9 – Thin sections of samples from RT1 (niçois parallel), with pore space highlighted in blue. Sample 146.25 (shells cemented by calcite); sample 113.70 (arrows indicate compaction direction and the dashed lines shells orientation), and sample 105.30 (arrow indicates whole shells and the yellow circle showing moldic porosity). The scale bar is 5 mm

The thin sections helped to understand the morphology of the pores and shells that are characteristic of each region separated by the PCA statistics. The difference in shell size of the samples is clear, as well as the composition of the pore system. Sample 146.25 was used as an example for the characterization of the rocks below the range of greatest influence (Fig. 4.8). The sample contained entire shells, from coarse to medium grain size, well sorted, and cemented and compacted, all factors that reduce the pore space and hence lower the flow capacity. Regarding pore type, the intraparticle pores stood out by being the most representative pore type for the samples of this region.

Sample 113.70 was used as an example of region *b* (Fig. 4.8), with T_2 peaks between 10 – 100 ms, being the region that most contributed to the permeability of the

cluster. The morphology of the shells and pores was analyzed in terms of their petrographic characteristics. A reduction in the size of the shells was noticed, with a clear orientation (dotted lines) caused by physical compaction (arrows), a common effect of samples from the formation. The fragmented shells had very coarse to granules, whole shells with granules to fine pebbles and well sorted. Quartz was present among the minerals in the thin section, being fine to coarse sand (mostly medium sand), and moderately well sorted. In the pore space, fragments of shells and other constituents could be observed, such as siliciclastic material that causes a reduction in the pore volume. As for the classification of pores, sample 113.70 had a predominance of interparticle pores, which is a characteristic of samples that have relaxation peaks within this region. It is evident that compaction identified in the thin sections has direct impact on pore connectivity, thus reducing the permeability of the system.

Thin section 105.30 was used to characterize typical samples in region ***c***, above the region of greatest influence. One could notice morphological differences of the shells and pores compared to the other samples. The sample contained medium to coarse-grained fragmented shells, as well as fine to medium pebble-sized whole shells, poorly sorted. Regarding its mineralogy, calcite minerals dominated, but quartz grains with fine to very coarse sand, high to low sphericity, subangular to angular, poorly sorted were also observed. The pores showed a predominance of intraparticle and moldic pores. The presence of relaxation peaks in this region may be due to the larger pores identified in the thin sections, mainly moldic pores generated by the dissolution of larger particles (shells or minerals). Evidently, the low flow capacity of the porous medium was due to the presence of more angular fragments, mainly of smaller particles, which directly affected the tortuosity of the system. Added to this fact, the narrowing of pore throats is equally important in terms of lowering the permeability. These findings explain the curves of samples 141 and 151.10 (Fig. 4.8). The dashed lines of the pore size distribution of these samples indicate the presence of large pores, classified as moldic, but having relatively low permeabilities resulting from narrower connections and flow through more tortuous paths.

Several conclusions are possible from the petrographic characterizations. Despite heterogeneity as shown by the NMR curves, similarities identified using the PCA analysis can be explained geologically by using various petrophysical aspects. Samples show similarity in the morphology of the shells and the pores when they have relaxation peaks in the same pore size partition. Region ***a*** showed the greatest cementation and pore

characteristics (mostly intraparticle pores), and a well-defined shells. The factor that contributed most to a lower permeability of the samples is cementation, which agglutinates the particles and impacts the conductivity. Region ***b*** has a predominance of smaller shells with good selection, but with more fragmented material in the pores as well as some orientation of the particles due to compaction. The rocks contain quartz grains with good selection and pores mostly classified as interparticle. The presence of more fragmented material, even with good selection, may be one explanation for the low permeability of the samples. This since the grains can block the pore throats, thus reducing the flow capacity. Region ***c,*** on the other hand, is characterized by fragmented shells having a relatively coarse granulometry, with poor selection. The presence of subangular to angular quartz particles highlights the poor selection of these minerals. The predominance of moldic pores explains the relaxation peaks in this region in that some particles that make up the rocks were completely dissolved, thus leaving empty spaces. However, due to the poor selection of shells and quartz grains, the connections between the large pores are reduced, thereby causing a lower conductivity.

All samples were analyzed using thin sections. In addition to morphological identification of the constituents of the samples and classification of the pores, the mineralogy was also examined. Compositionally, most of the minerals were found to be calcites, but siliciclastic material was also present, mainly in samples 87.35, 105.3 and 113.70. Because of high visual quantification, the samples were submitted to XRD experiments to define the complete mineralogy. The results in Fig. 4.10, obtained using the Rietveld method, show the percentages of each mineral that make up the samples. Most of the constituent minerals were calcites, making up a total of 83% in sample 87.35, 95.6% in sample 105.30 and 68% in sample 113.70. Quartz was also present, especially in sample 113.70, making up 26% of the total minerals. The feldspar mineral microcline was also found, mostly in sample 113.70 (3%). The samples also contained some kaolinite clay, presumably due to diagenesis suffered by these rocks. Despite the appearance of the siliciclastic minerals in the samples, their petrophysical characteristics remained similar to the others in the cluster.

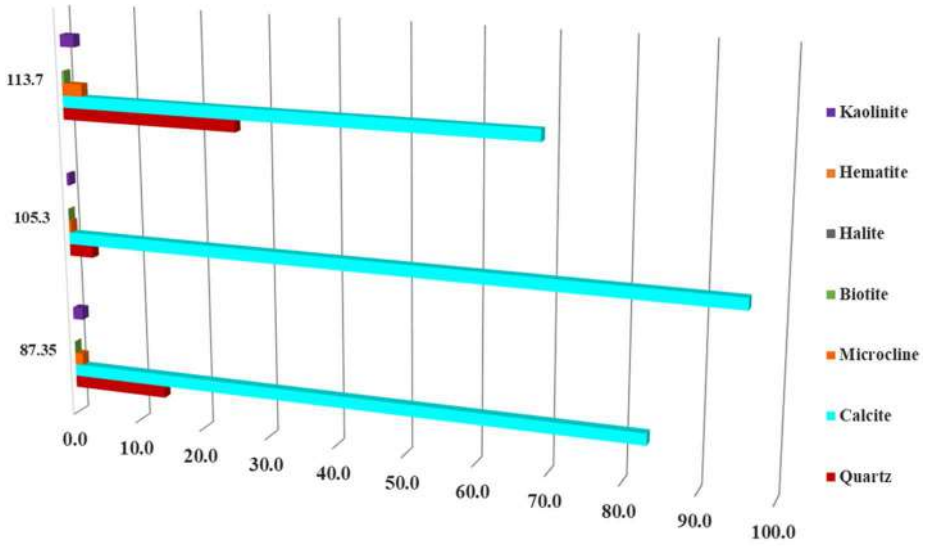

Figure 4-10–XRD results from samples 87.35, 105.3 and 113.70 showing a predominance of calcite in the samples

4.2.2 Characteristics of Rock Type 2 (RT2)

The RT2 cluster, shown in Fig. 4.3, contains samples with slightly higher permeabilities as compared to RT1. Table 4.3 shows the main petrophysical characteristics of the RT2 samples, such as porosity, permeability and $T_{2Logmean}$, in addition to geological aspects such as the fragmentation percentage of the shells and siliciclastic minerals, the main minerals as determined using X-ray diffraction, and their pore classification according to CHOQUETTE & PRAY (1970). The data in Table 4.3 show that the porosity of the RT2 samples varied between 11 and 19%, and the permeability between 10.57 and 93.04 mD, while the average relaxation times slightly decreased consistent with the increase in permeability.

Table 4-3 – Petrophysical and geological properties of Rock Type 2

Sample (m)	Φ_{Rout} (%)	K_{Rout} (mD)	$T_{2Logmean}$ (ms)	Shells fragm. (%)	Silicic. Min. (%)	Pore Classif.	XRD Calcite	XRD Qtz
66.35	19.1	93.1	212.1	60	10	Intraparticle (60%)	-	-
73.20	18.2	70.8	262.5	60	30	Intraparticle (40%)	93%	5%
80	16.3	22.9	64.8	80	68	Moldic (50%)	61%	29%
126.05	11.5	10.3	225.1	15	-	Interparticle (35%) intercrystaline (20%)	-	-
128.05	12.1	22.1	145.1	2	3	Interparticle (35%) Intercristalina (20%)	-	-
132.15	11.3	10.6	177.5	15	1	Intercrystaline (40%)	-	-
133.90	13.3	14.5	165.9	10	10	Intraparticle (60%) Interparticle (20%)	-	-
154.20	16.6	62.8	390.1	25	10	Moldic (60%)	-	-
184.95	11.1	51.5	285.2	20	-	Intercrystaline (50%) Vug (30%)	-	-

Fig. 4.11 shows the pore size distributions of the samples in the RT2 set. The T_2 distributions, normalized by the total area, indicate that the samples have larger pores compared to RT1, with a slight bimodal distribution. The majority of pores have relaxation times above 100ms, mostly within the hybrid mesopore and macropores regions. Unlike for RT1, the RT2 pore distributions are more grouped together, with $T_{2Logmean}$ averages ranging between 64.84ms and 390.12ms, with a predominance of meso and macroporosity.

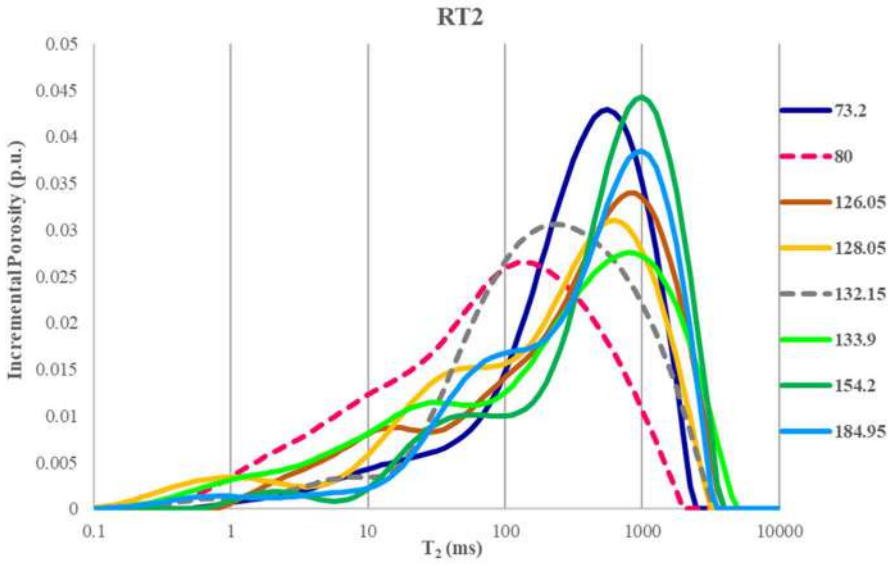

Figure 4-11 - Plot showing T_2 distribution curves for RT2 samples. The dashed lines show different curves for samples 80 and 132.15

Observing the RT2 cluster curves, it appears that most samples have relaxation peaks in the same region, close to 1000ms, thus indicating a greater volume of pores with sizes between meso- and macropores. Even with their different pore volumes, the distributions are quite similar. However, samples 80 and 132.15, highlighted by the dotted lines in Fig. 4.11, show some divergence from the other distributions. With their relaxation peaks closer to 100ms, the samples have porosities of 16.34% and 11.30%, permeabilities of 22.93 mD and 9.08 mD, and $T_{2Logmean}$ averages of 64.84ms and 177.51ms, respectively. Even with the differences in the T_2 curves, the variations in the petrophysical parameters are well within the expected range for the RT2 cluster. Still, the divergence found for these samples required complementary analyses to justify their grouping within this rock type.

Because of the deviations in the pore-size distributions of samples 80 and 132.90, other investigative methods were used to justify their presence in RT2. The first method was again PCA multivariate statistics. Contrary to what was possible for RT1, the PCA analysis of RT2 did not provide a conclusive explanation for the divergences that were found, with little agreement between the samples in the principal components. PCA is often unable to decode the responses found in the data being study, thus requiring other methods. This was done using thin sections to analyze information provided by petrophysics and NMR, and to search for possible similarities among the samples within RT2. Fig. 4.12 shows the thin sections that were obtained for the RT2 samples.

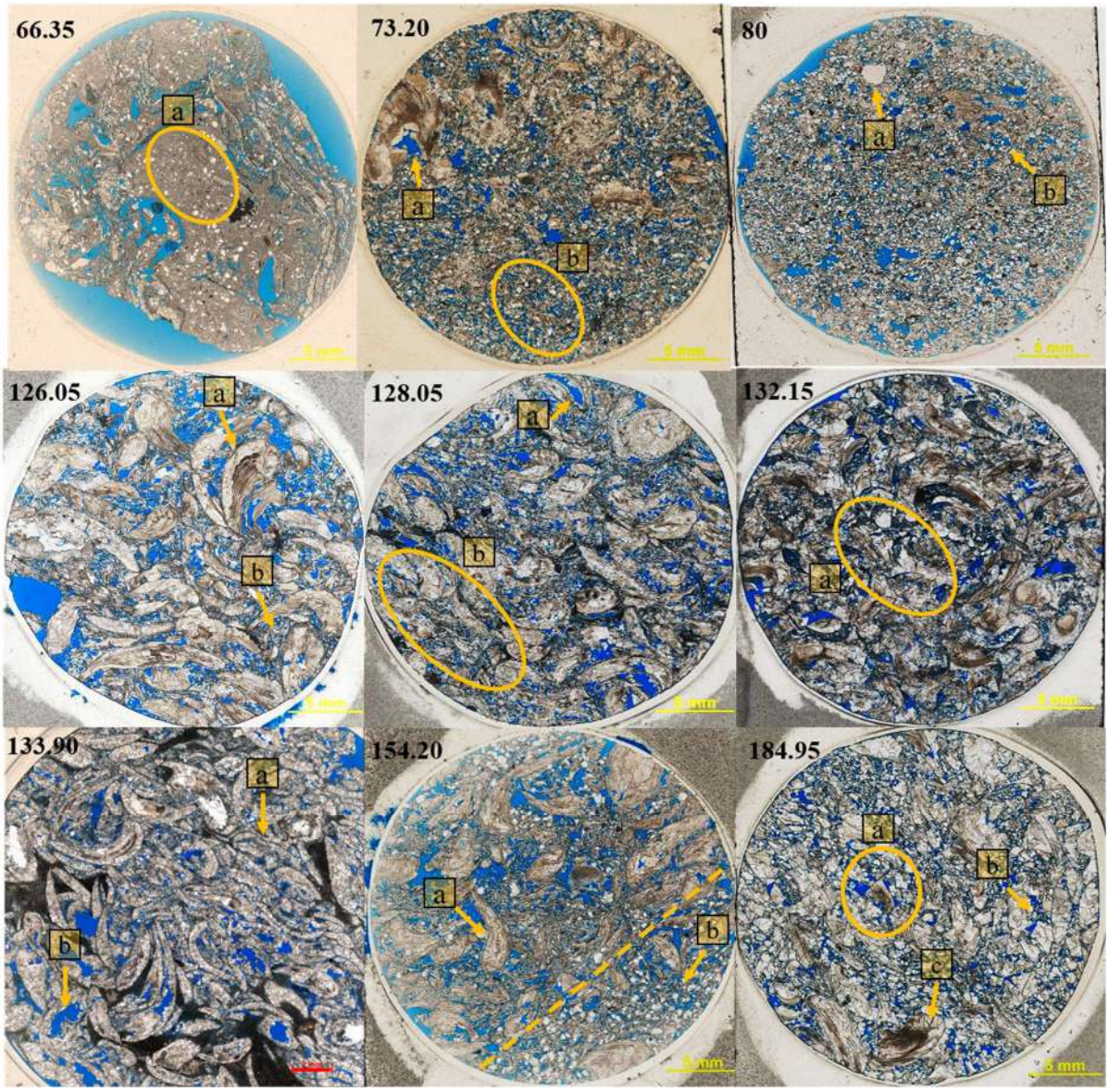

Figure 4-12 – Thin sections of the RT2 samples (parallel niçois). Some features are highlighted in blue: Sample 66.35 – a) micritized matrix with quartz; Sample 73.20 – a) intraparticle pore, b) shell fragments and quartz inside the pore space; Sample 80 – a) monocrystalline quartz, b) moldic pore; Sample 126.05 – a) whole shells, b)) shell fragments at the pore space; Sample 128.05 – a) intraparticle pore, b) shell compaction, pore space filled with fragments; Sample 132.15 – a) cementation; 133.9 – a) shell compaction, b) intraparticle pore; Sample 154.20 – a) whole shell, b) pore space filled with fragments; pore space filled with fragments above the dashed line; yellow circle shows quartz within the pore space; Sample 184.95 – a) angular shell fragment, b) elongated pores caused by shell fragmentation, c) whole shell. Scale bar = 5 mm

Similarly as for RT1, the first aspect explored of the RT2 thin sections was the morphology of the shells and pores. The morphological differences between the samples are very much evident. Several characteristics can be highlighted:

- Sample 66.35 had a clearly visible micritized matrix (carbonatic clay) in which subangular quartz grains were deposited. Predominance of intraparticle pores;
- Sample 73.20 contained partially dissolved and fragmented shells (60%) that were poorly sorted. Presence of siliciclastic subangular material. Intense micritization and dissolution. Predominance of intraparticle pores;
- The thin section from sample 80 exhibited fragmented shells that were moderately sorted, making up 80% of the total particles. Presence of quartz, fine to very coarse sand, moderately sorted. Micritization is visible, characterized by micrite envelopes at the pore boundaries. Pores were formed by dissolution while maintaining the shape of the particles. Predominance of moldic pores;
- The thin section of sample 126.05 showed whole shells (85%) in some compacted portions. The pore space contained shell fragments and medium to very coarse sand-size, poorly selected. Predominance of intraparticle pores;
- Sample 128.05 consisted predominantly of entire shells, as well as coarse particles to fine pebbles, moderately sorted, 98% of the particles present. Compacted shells could be observed, containing fragmented shells, causing a reduction in the pore space. Most pores could be classified as interparticles;
- The thin section from sample 132.15 showed much evidence of compaction: the presence of robust whole shells, coarse sand to fine pebbles, poorly sorted, making up 85% of the total particles. The pores, in their majority, could be classified as intercrystalline, partially filled by shell fragments, medium to very coarse sand;
- The thin section from sample 133.90 consisted of whole shells, granules to fine pebbles, moderately sorted (90% of the total) and quartz grains (10%). Evidence of compaction with fragmented shells, coarse to very coarse sand. Occurrence of porosity by dissolution, leading to a higher percentage of interparticle pores;
- Sample 154.20 contained whole shells, up to 75% of the total, and coarse sand to fine pebbles. The pore space was filled by shell fragments and

quartz, subangular, moderately sorted, mainly in the lower region of the slide (below the dotted line). Diagenetic action resulted in a moldic porosity, associated with micritization;

- Sample 184.95 contained whole shells, up 80% of the total, very coarse to fine pebble. Fragmented shells medium to very coarse sand, poorly sorted. Intercrystaline pores predominate.

The petrographic analysis of the samples failed to identify other geological characteristics that could justify the clustering. No single cause could be identified for the development of the pore space of the RT2 samples. According to the T_2 curves (Fig. 4.11), most of the samples showed that pores concentrated mostly in the region from mesopores to macropores, with overlapping peaks, but with diverging pore volumes. The main similarity of the RT2 rocks hence is that they have the same permeability range by containing pores of similar sizes but reflecting different geological processes. The RT2 grouping hence is considered to be a transition group separating the region with the lowest permeability (RT1) from the region with the highest permeability (RT3), which will be discussed hereafter.

Despite cluster RT2 being a transition region in which the samples do not have petrographic similarities, we still evaluated the mineralogical composition of the samples. As reported earlier, calcite was identified as the predominant mineral of the rock. However, some siliciclastic material could be identified in several samples, especially in the thin sections of samples 73.20 and 80. These samples were submitted to XRD analyses, again using the Rietveld method, since they visually showed a higher content of siliciclastic material. The results for samples 73.20 and 80 in Fig. 4.13 indicated that calcite was again by far the most abundant material, totaling 83% and 70%, respectively. Quartz was present in both, with sample 80 having a higher percentage (29%). Other siliciclastic minerals were identified, such as microcline, a feldspar mineral, which occupied 1.6% and 4.5% of samples 73.20 and 80, respectively. Kaolinite clay was also identified in sample 80 (2%), resulting from diagenetic processes.

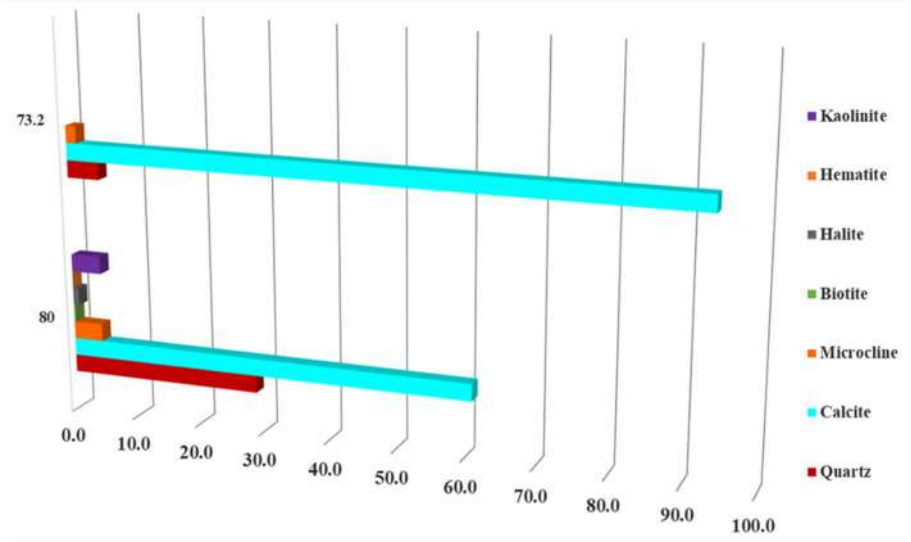

Figure 4-13 – Results of XRD from samples 73.20 and 80. Sample 80 showed more siliciclastic material

It is important to note that, even though the RT2 samples are in a transition region with their own specific petrographic characteristics, the studied specimens are still quite similar in terms of their heterogeneity. This fact can be explained by the NMR results (Fig. 4.11), which show that even with their multimodal distributions, the highest pore volumes are located in the same time range of relaxation, indicating that the pore systems of the samples are similar. This interesting characteristic causes these samples to remain in their own group.

4.2.3 Characteristics of Rock Type 3 (RT3)

Following the logic of the development of the rock types of this study, all rocks that showed permeabilities above 100 mD were grouped initially in a single cluster. The NMR results, however, showed that they exhibited divergent pore-size distributions and hence could not be included in the same group. This motivated us to establish three new groupings: RT3, RT4 and RT5. This separation enabled a more complete description of the samples by assembling specimens with similar hydraulic characteristics. Thus, RT3 contains rocks with higher permeabilities, as can be seen in Table 4.4. This table presents the main petrophysical and petrographic characteristics of the samples, similarly, as done before for the other rock types.

Table 4-4 – Petrophysical and geological properties of Rock Type 3

Samples	Φ_{Rout} (%)	K (mD)	$T_{2Logmean}$ (ms)	Shells Fragm. (%)	Silicic. Min. (%)	Pore Class.	XRD Calcite	XRD Qtz
80.95	19.6	482.3	528.9	70	15	Moldic (30%) Vug (30%)	90.6%	8.3%
83.05	18.6	556.4	484.4	90	5	Intraparticle (50%)	-	-
83.65	17.4	369.9	434.8	70	15	Vug (30%) Moldic (25%)	59.3%	33.1%
90.95	15.2	412.2	274.4	30	15	Vug (45%) Intercrystaline (35%)	97.9%	2.1%
98.55	18.4	649.9	398.1	10	-	Vug (60%)	-	-
100.7	16.3	217.4	458.5	5	-	Vug 50% Intraparticule (30%)	-	-
136.85	15.9	175.5	405.3	35	12	Vug (50%)	-	-
156.5	14.1	179.4	571.3	20	8	Vug (75%)	-	-
160.10	13.4	110.1	638.8	15	-	Vug (80%)	-	-
180.00	16.8	245.1	749.3	40	-	Vug (70%)	-	-
187.95	12.1	152.4	461.2	5	-	Vug (35%) Intercrystaline (35%)	-	-
189.40	15.10	191.58	463.13	3	-	Vug (60%)	-	-

As can be seen in Fig. 4.3., RT3 is formed by samples with the highest permeabilities, yet intermediate porosities. While porosities ranged from 12% to 19%, permeabilities were between 110 and 649 mD. The higher permeability values are consistent with the relatively high average relaxation times as shown by the NMR-derived pore-size distributions of the RT3 samples in Fig. 4.14. The distributions in this figure show a predominance of pores in the macroporosity region, with peaks at slightly more than 1000 ms, with very few micropores. The difference with the previous groupings is clear: the increase in the permeability and T_2 values reflect a predominance of large pores. The $T_{2Logmean}$ averages increased to between 110 and 649 ms, consistent with the increase in permeability.

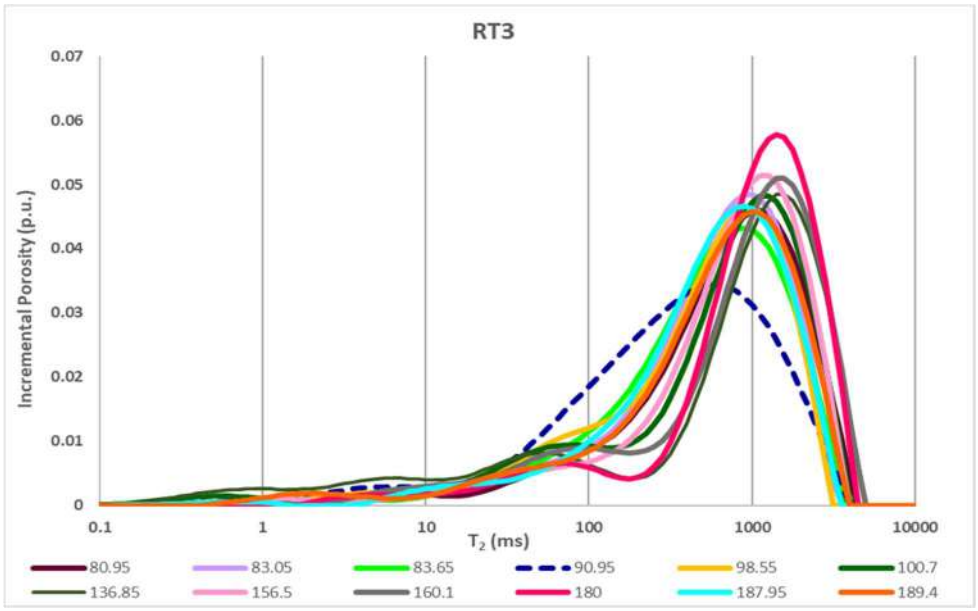

Figure 4-14 - Plot showing T_2 distributions for RT3 samples. Note that most samples had very similar distribution. Sample 90.95 is represented by a dashed line to highlight the different shape of its T_2 distribuition

The T_2 curves in Fig. 4.14 indicate that almost all samples in the cluster have much of their pores in the same region, close to 1000ms. The overlapping of the NMR curves furthermore confirms the considerable similarity of the various RT3 samples, except for sample 90.95. The peak of the distribution for this sample was located slightly to the right, thereby reflecting a change in pore size with a predominance of pores in the meso/macro hybrid region. Its pore volume was lower compared to the others in the group as shown by its $T_{2Logmean}$ value of 274.37ms, one of the lowest in the group. However, this sample still had a porosity of 15.23% and a permeability of 412.2 mD, one of the highest in the group. Because of these peculiarities, other methods were used again to justify the similarities among the samples, including sample 90.95, first with multivariate statistics.

In the PCA technique, the spectrum data (bins) of the NMR experiment were used to identify the most influential pore partitions in the group, thus demonstrating their similarities. In Fig. 4.15, the scores of these variables are presented for the entire set of rocks in the study, with the RT3 samples identified by the yellow color.

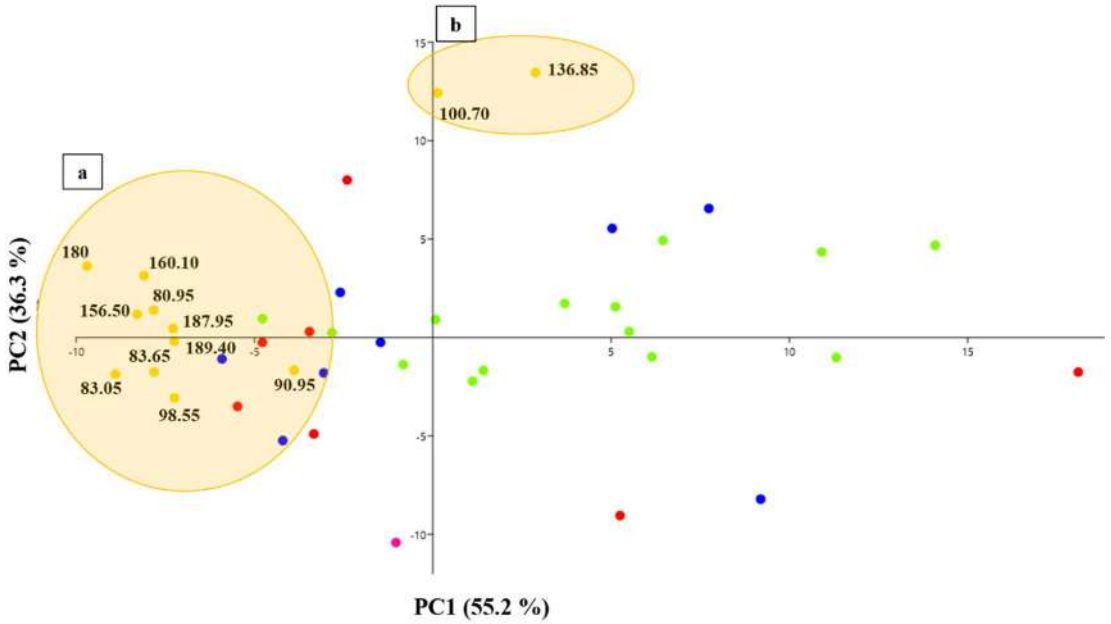

Figure 4-15 – Plot showing scores for all samples. a) Most RT3 samples are concentrated at – x axis (PC1); b) 100.70 and 136.85 are concentrated at +y axis (PC2)

To better interpret the results, the loadings graphs of the components were further analyzed, with results shown in Figs. 4.16 and 4.17 for components PC1 and PC2, respectively. The PC1 graph in Fig. 4.16 shows that the highest negative values correspond to relaxation times between 250 - 5000ms, being part of the meso/macro hybrid region and the region of predominance of macropores. These partitions hence have a greater influence on the cluster, and thus contribute more to flow in the pore system. The higher permeabilities of these samples are hence due to an increase in the size of the pore throats. Regarding sample 90.95, whose T_2 curve diverged from the other samples, its distribution belongs to the same group of pore sizes that predominate the RT3 group. This shows that even with a difference in the pore-size distribution curve provided by NMR, sample 90.95 is still very similar to the others.

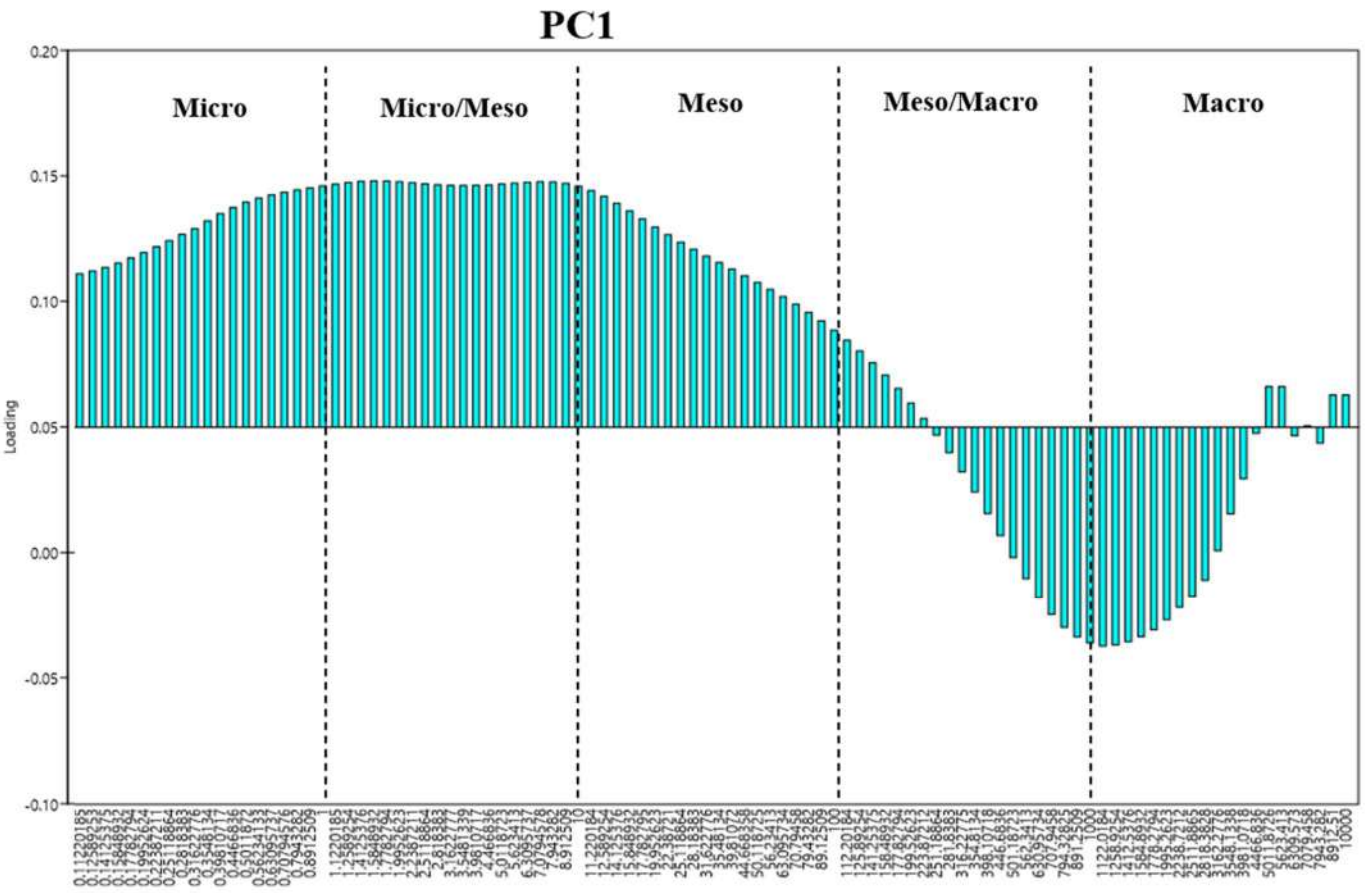

Figure 4-16 – PC1 loading plot showing the contributions of each pore size partitioning

The PCA analysis showed a different behavior of two samples in the cluster: 100.70 and 136.95. The NMR distributions of these two samples were quite similar as the others, which was not apparent from the PCA results in Fig. 4.15. To better understand these differences, Fig. 4.17 shows the PC2 loadings graph (the principal component where the samples are located).

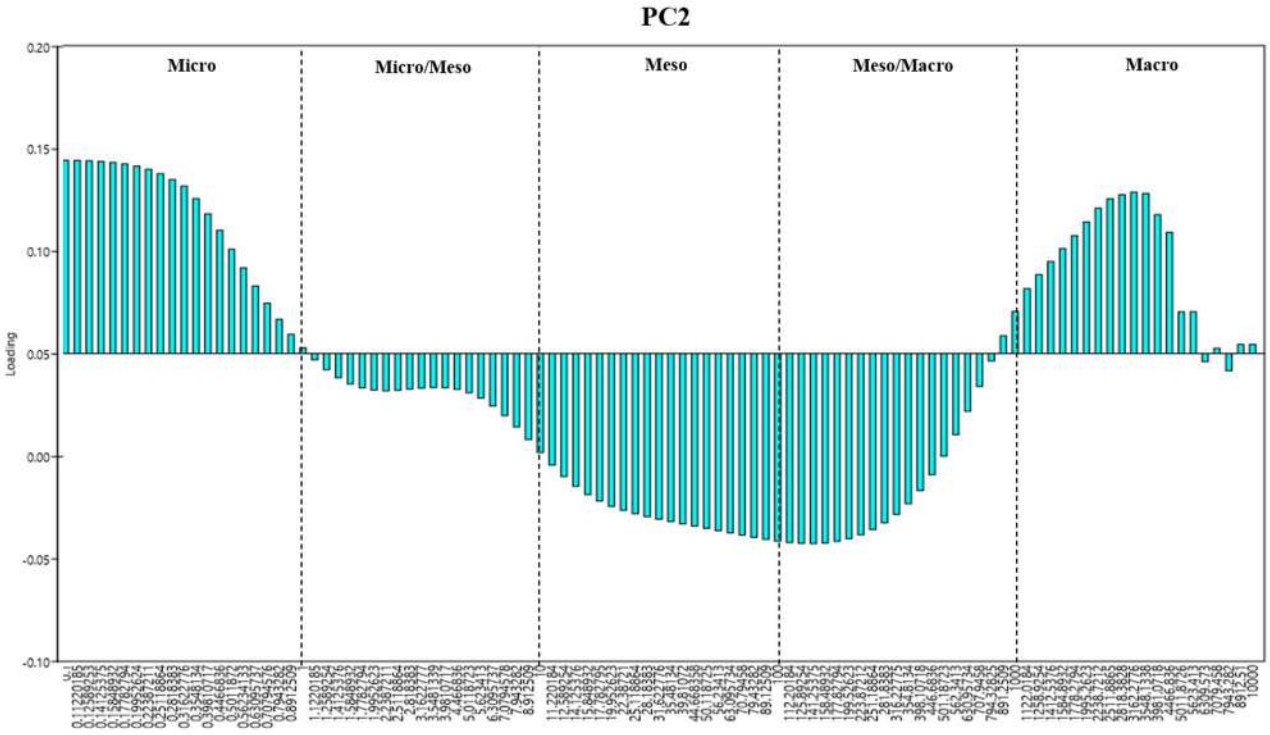

Figure 4-17 – PC2 loading plot showing the contributions of each pore size partitioning

One of the great virtues of PCA statistics is its versatility in various applications. For RT1, the PC2 component explained similarities between the samples, similarly as for RT3 in terms of the pore partitions that influence samples 100.70 and 136.95. These two samples were positioned on the positive part of PC2. The loadings graph in Fig. 4.17 shows that the highest positive values are attributed to two distinct partitions: micropores and the region of predominance of macropores. Since the distribution provided by NMR encompasses the entire pore space without differentiating between pore bodies and pore throats, one may conclude that the samples have large pore bodies (peak of the T_2 distribution), connected by micrometric throats (slight elevation in the T_2 curve). However, this interpretation does not exclude the possibility of having larger throats, a fact compatible with the high permeability value of the samples (217.41 mD and 175.47 mD for samples 100.70 and 136.95, respectively). To better analyze this possibility, thin sections of the samples were studies next.

Thin sections were evaluated, highlighting some geological characteristics that impact porosity and permeability: fragmentation of shells, mineralogical composition and types of pores (Fig. 4.18).

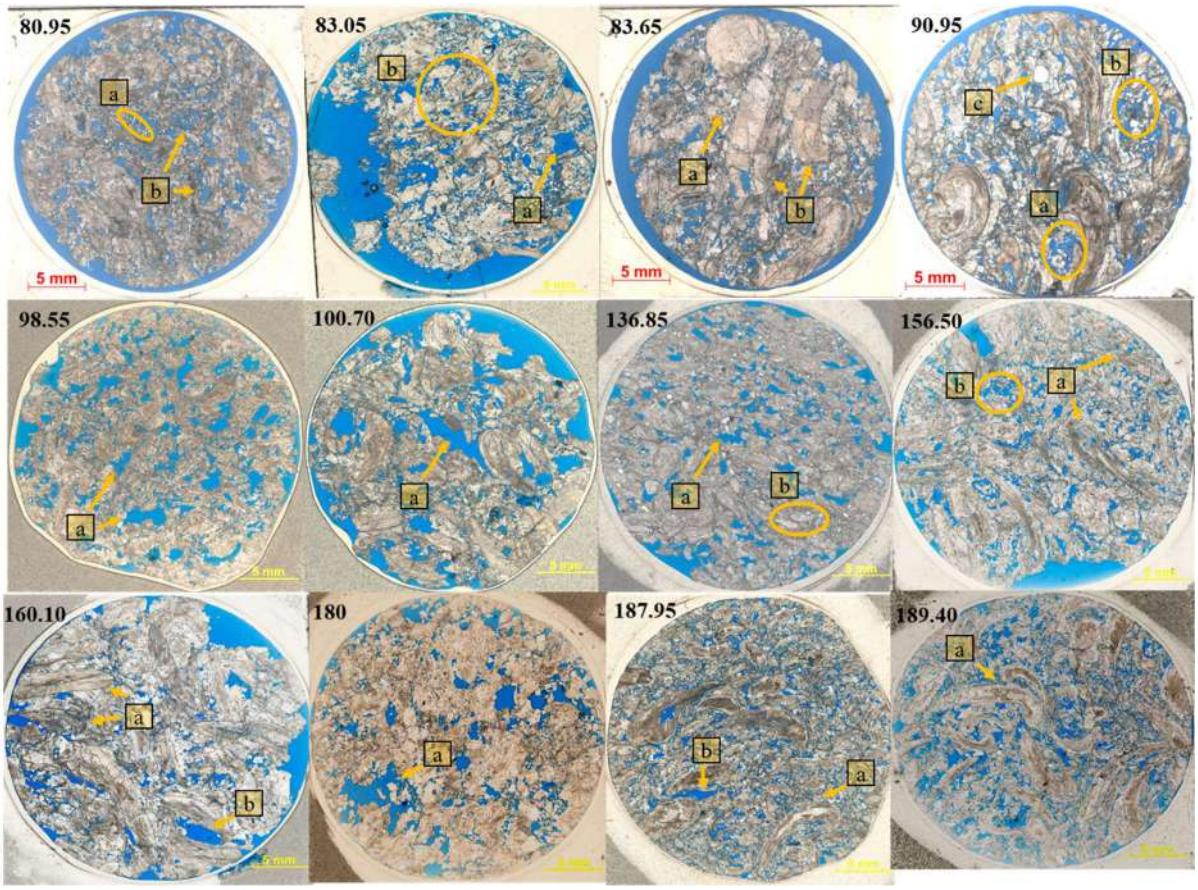

Figure 4-18 – Thin sections of samples from RT3 (parallel niçois). Some features are highlighted: 80.95 – a) Shells and quartz fragmented, b) vug porosity; 83.05 – a) vug porosity, b) shells highly fragmented; 83.65 – a) intercrystaline porosity, b) robust shells fragmented; 90.95 – a) vug porosity, b) shells dissolved, c) quartz; 98.55 – a) vug porosity; 100.7 – a) vug porosity; 136.85 – a) vug porosity, c) whole shells; 156.60 – a) whole shells, b) vug porosity; 180 – a) vug porosity; 187.95 – a) whole shells, b) vug porosity; 189.40 – a) whole shells. Scale bar – 5 mm

Analyzing the thin section in Fig. 4.18 some aspects can be noted: sample 83.05 shows the typical impact of fragmentation on the permeability, making up 90% of the shells fragmented, leading to a heterogeneous structure involving secondary pores classified as intraparticle pores, as well as vugular pores causing a high permeability of the system. The remarkable presence of vugular porosity in most of the thin sections also helped us to understand the hydraulic behavior of the cluster: the samples demonstrate the effects of dissolution, i.e., chemical processes that affect carbonate rocks by increasing their hydraulic capacity. This diagenetic process causes the formation of secondary pores, causing an increase in both pore bodies and pore throats and reducing the tortuosity of the system. This effect can be seen clearly in samples 80.95, 90.95 and 98.55, which have the highest permeability of the group: 482.3, 412.20, and 649.91 mD, respectively.

Another important diagenetic effect exhibited by the RT3 thin sections was the cementation of particles. Cementations is capable of agglutinating loose particles in the porous interior by transferring saturated fluid to the cement phase, a process which depends on the chemistry of the water and the available carbonate supply. This process can be seen for samples 83.65, 136.85 and 160.10. These samples show that cementation occurred as the first diagenetic phase, followed by a second diagenetic phase, dissolution. This sequence of events caused a reworking of the shells, thereby contributing to the interconnection of the pores and, consequently, to an increase in the permeability. The existence of multiple diagenetic phases is evident in these samples, which may explain the increase in flow through the pore systems.

The T_2 curve of sample 90.95 in Fig. 4.14 exhibited a different shape, which is consistent with its thin section showing more elongated pores and probable wider throats caused by dissolution, thereby enhancing the connectivity of the pore system. Even with its difference with other RT3 curves, this sample is petrographically similar to the others by containing many vugular pores that increased the permeability of this rock.

As with the previous groups, fragmentation percentages of the shells in the RT3 samples were quantified. Most thin sections showed clear fragmentation, especially sample 83.05 (90% fragmentation), followed by samples 80.95 and 83.65 having 70% fragmentation each. The samples consequently have relatively high permeability values: 556.36, 482.3 mD, and 369.90 mD, respectively

Another important aspect of rocks is the type of pores that can be classified using the thin sections. Many RT3 thin sections show vugs, relatively large pores with often a poorly defined geometry, which is common for carbonate rocks and resulted from their diagenesis. Several studies demonstrated that connected vugs can significantly increase the flow capacity of reservoirs, at times reaching a permeability of 10 D (AHN, 2008), which suggests that vugs are a likely cause of the increase of this parameter in the RT3 rocks.

The mineralogical composition was further measured using thin sections. Results confirmed that most of the minerals present were calcites, but siliciclastic materials were also observed, similarly as in the other groups described above. Fig.4.19 shows the mineralogical composition and the mineral percentages of samples 80.95, 83.65 and 90.95 as obtained from the XRD measurements. The three samples showed a predominance of calcite, totaling 90% of sample 80.95, 59% of sample 83.65 and 80% of sample 90.95. Quartz was also quantified, with sample 83.65 showing the highest

percentage (33%). The siliciclastic microcline mineral was found in sample 80.95 (0.1%) and, in a much greater quantity, in sample 83.65 (4.6%). Some kaolinite clay was also identified, with percentages being around 1%, resulting from the alteration of siliciclastic minerals. As noted earlier, these siliciclastic minerals in the samples did not modify the petrophysical characteristics of the various samples in this group.

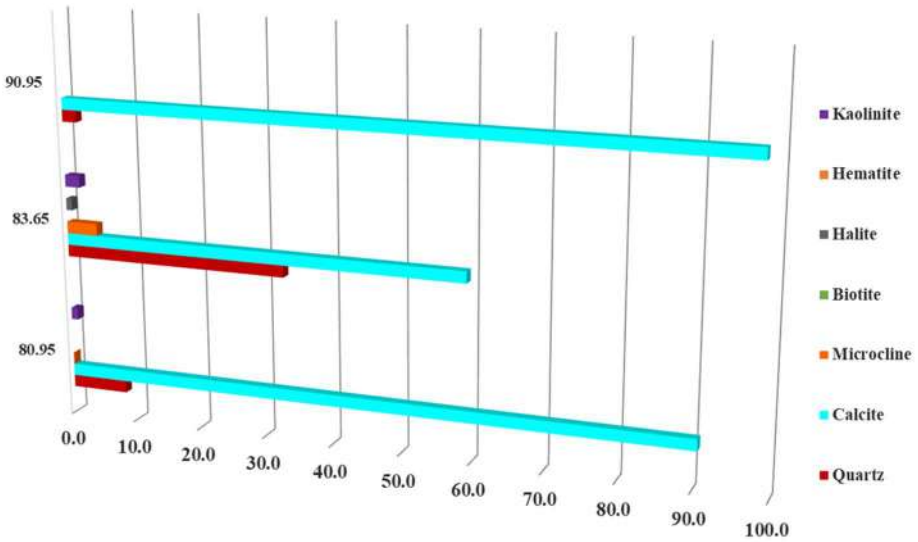

Figure 4-19 – XRD results for samples 80.95, 83.65 and 90.95

4.2.4 Characteristics of Rock Type 4 (RT4)

As mentioned earlier, samples with permeabilities above 100 mD were subdivided into three groups (RT4, RT4 and RT5). RT4 contained samples with slightly lower permeabilities compared to RT3, as can be seen by the entries in Table 4.5 summarizing the RT4 petrophysical information and petrographical characteristics. The data show a decrease in permeability as compared to RT3. Porosities ranged from 17.5 % to 20.2 %, and permeabilities from 92.88 mD to 243.58 mD, slightly lower than those of the RT3 grouping. The average relaxation times ($T_{2Logmean}$ times) were also lower than those of RT3, consistent with the reduction in permeability.

Table 4-5 – Petrophysical and geological properties of Rock Type 4

Sample	Φ_{Rout} (%)	K (mD)	$T_{2Logmean}$ (ms)	Shells Frag. (%)	Silicic. Min. (%)	Pore Class.	XRD Calcite	XRD Qtz
68.65	18.2	113.8	269.2	30	30	Vug (50%)	-	-
82.05	19.4	169.2	357.2	70	15	Moldic (35%) Vug (25%)	-	-
93	19.8	232.9	437.6	20	-	Vug (30%) Moldic (30%)	-	-
94.4	18.5	103.5	56.1	100	70	Interparticle (60%)	56%	37%
102.55	18.8	165.8	310.9	90	5	Intraparticle (45%) Interpartícle (40%)	-	-
162.5	17.5	121.9	311.1	85	5	Moldic (45%) Intraparticle (30%)	-	-
170.65	20.2	243.6	130.7	98	45	Interparticle (35%) Vug (25%)	62.6%	31%

Fig. 4.20 shows the NMR measured pore-size distributions of the RT4 samples, with the T_2 curves normalized by the total area. The curves exhibit strongly unimodal properties, with many of the pores having relaxation times above 100 ms in a relatively hybrid region of meso/macro pores. As can be seen, the average $T_{2Logmean}$ times varied between 56.11 ms and 357.16 ms, slightly slower than those of the RT3 samples. Samples 94.4 and 170.65, highlighted by yellow and green dashed lines, respectively, showed different distributions. Sample 94.4 contained pores that are more distributed throughout the plot, but still showing a predominance of meso to macropores, while sample 170.65 exhibited a well-marked bimodal curve, with relaxation peaks in two different partitions: the mesopore region and the hybrid meso/macropore region. Their average $T_{2Logmean}$ times were 56.11ms and 130.65ms, respectively.

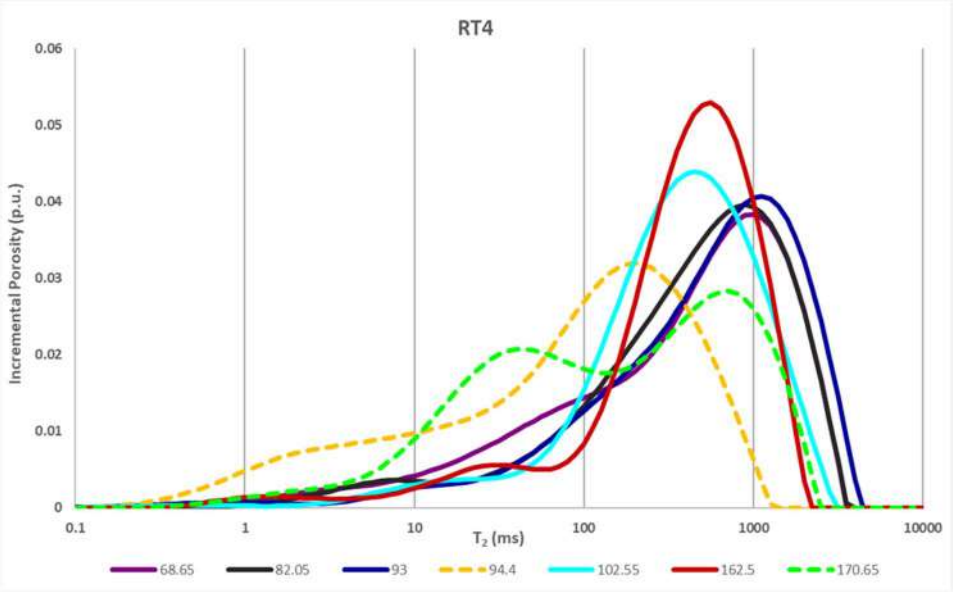

Figure 4-20 - Plot showing T_2 distributions curves for RT4 samples. Samples 94.4 and 170.65 are represented by dashed lines to highlight the different shape of their distributions

Samples 94.4 and 170.65 had T_2 distributions that diverged from those of the other RT4 rocks, thus requiring additional investigations using other methods to justify their positioning in the group. The first tool used for this was again a PCA multivariate statistical analysis. Fig. 4.21 shows a plot of the PC3 versus PC1 scores of the variables for the entire set of 44 samples, with the RT4 samples identified in red. The plot indicates the formation of sample clusters in three subgroups: *group a*, formed by samples 68.65, 82.05 and 93, located close to the negative axis of PC1; *group b*, formed by samples 102.55 and 162.50, located close to the positive axis of PC3; and finally *group c*, composed of samples 94.4 and 170.65, located in the positive quadrant of the two principal components.

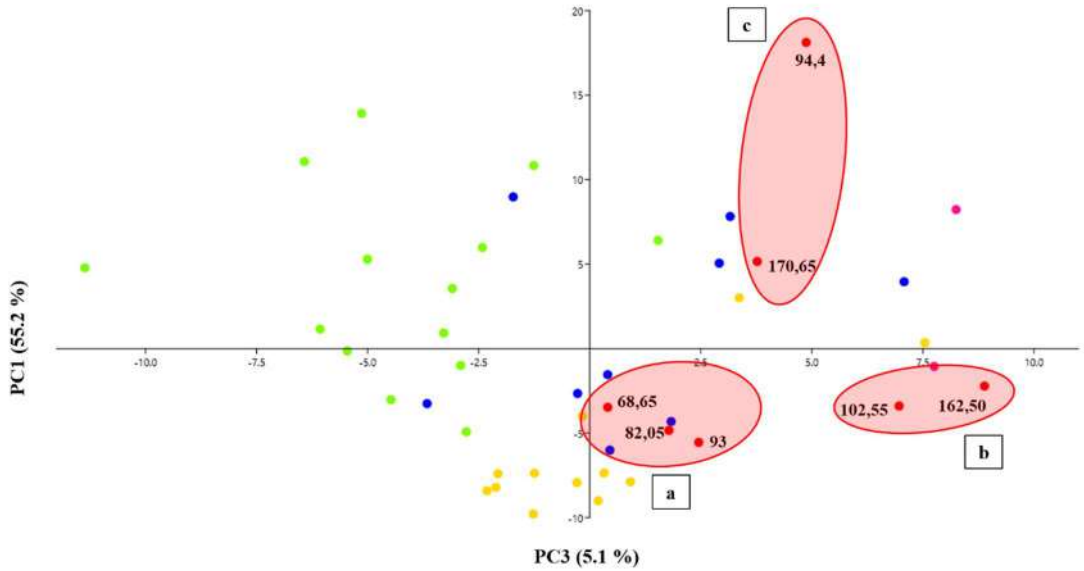

Figure 4-21 – Plot showing scores for all samples. Group ***a*** concentrates samples along PC1 axis; group ***b*** has samples along PC3 axis, while group ***c*** consists of samples in positive quadrant of the PC3 and PC1 components

To interpret the close positioning of the samples in Fig. 4.21, the loadings graphs of the principal components were used again to display the contributions of each variable. Because of their close location, the graphs of PC3 and PC1 are presented together in Fig. 4.22.

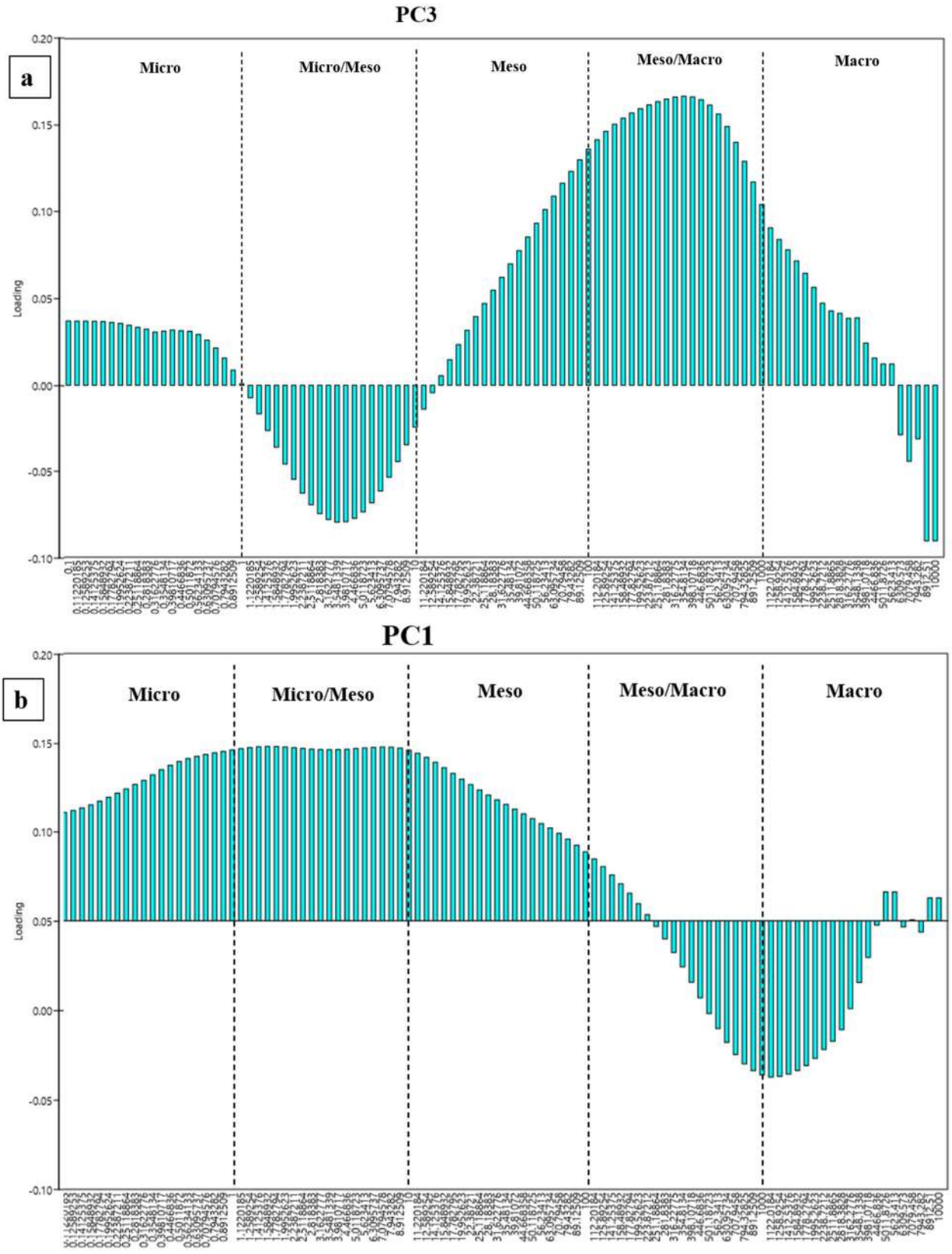

Figure 4-22 – PC3 and PC1 loading plots showing the contributions of each pore size partitioning

The scores graph in Fig. 4.21 showed that the samples came together in three groups: *group a*, *group b* and *group c*. The loadings graphs of the components in Fig. 4.22 reveal the relaxation time zones with the greatest influence in accordance with the positioning of the samples in the scores graph. Thus, *group a* containing the highest negative values of PC1 represents a region comprised of partitions from meso/macro to macro pores (250 to 4000 ms). This interpretation about the T_2 curves implies that samples 68.65, 82.05 and 93 are strongly influenced by relatively large pore higher relaxation times, with their T_2 distribution peaks overlapping at about 1000 ms.

The samples within *group b* (102.55 and 162.50) have high positive values of PC3, influenced by the micropores partitions (0.1ms to 1ms) and meso to macro pores (15ms to 4000ms). With the aid of the resulting NMR curves, we identified that these samples have their peaks superimposed, being strongly influenced by pores of the hybrid meso/macro region. Probably the pore bodies have a larger diameter, but the smaller pores identified in the PCA are responsible for the connectivity and fluid flow, which would justify the reduction of permeability when compared with the RT3.

Group c, presenting samples located in the positive quadrant of the principal components, exhibit a different behavior, mainly due to the result of PC1. The high positives of PC1 include relaxation times from 0.1 ms (micropores) to 220ms (meso/macro pores), with the influence distributed over almost all pore sizes within the spectrum. Due to its location, sample 94.40 is likely to be more influenced by these pore sizes as compared to sample 170.65. The high positives of PC3 are identified by the strong influence of micropores partitions (0.1 to 1 ms) and meso- to macropores (20 to 4000 ms), strikingly more in the sample 170.65 due to its location next to this component. Analysis the information together with the T_2 curves shows that the more elongated distribution of the sample 94.40, with its larger pores in the meso region, must be connected through smaller pores (micropores). The bimodal curve of sample 170.65 is marked by a strong influence in the meso- and macropore region, having larger pore bodies (within the meso/macro hybrid region) connected through meso-sized throats.

Compared with the RT3 samples, the characteristics of the pore system of RT4 samples would theoretically not explain a reduction in permeability, which would be necessary to evaluate the petrographic factors that explain the differences in this petrophysical parameter. For this analysis, the thin sections were interpreted and are shown in Fig. 4.23.

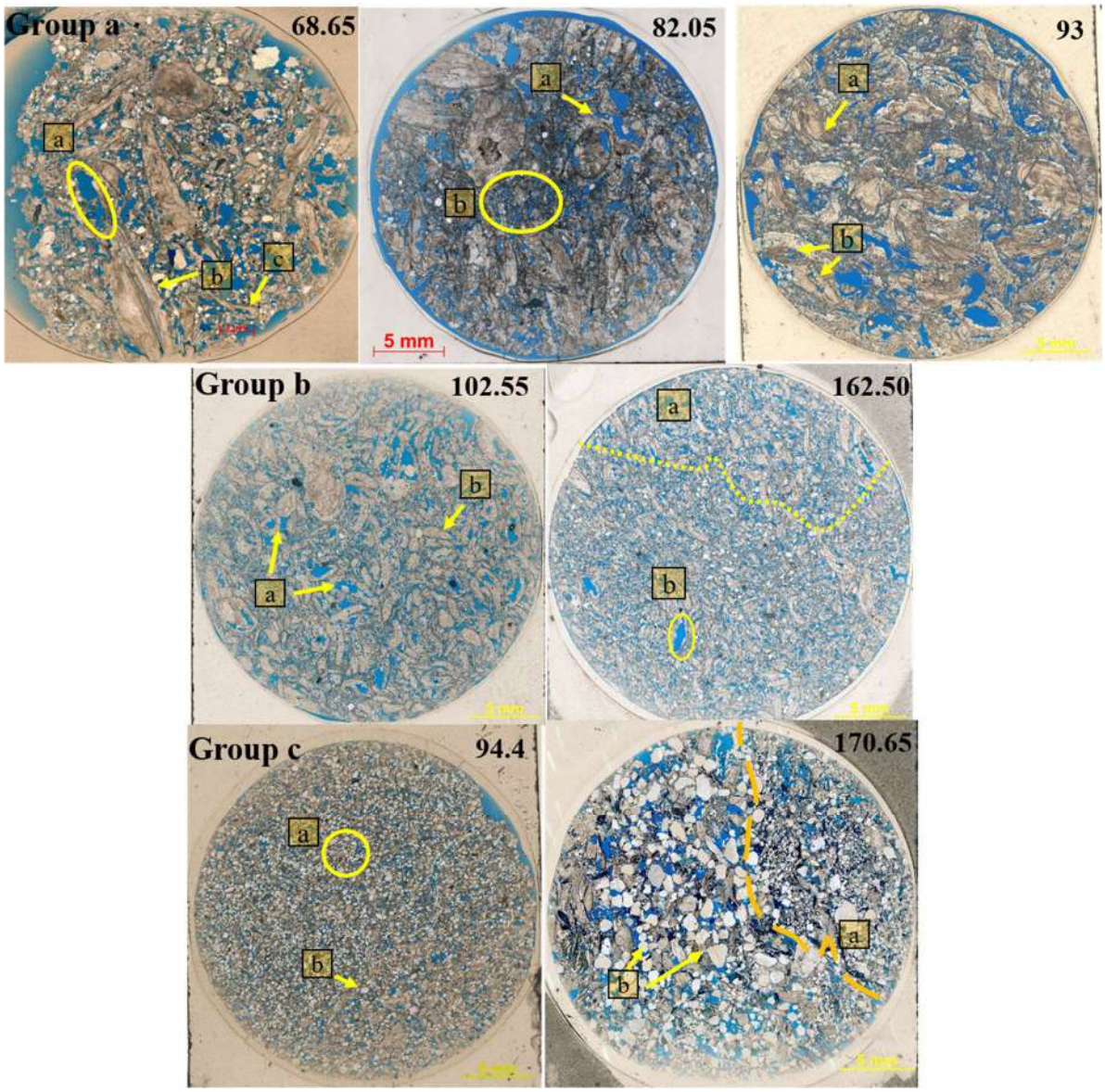

Figure 4-23 – Thin sections of RT4 samples (parallel niçois). Some features are highlighted: 68.65 – a) vug porosity, b) whole shells; 82.05 – a) vug porosity, b) fragmented shells; 93 – a) whole shells, b) intraparticle pores; 102.55 – a) intraparticle pores, b) whole shells; 162.50 – a) yellow dashed line separated whole shells zone, b) moldic pores into fragmented zone; 94.40 – a) shells highly fragmented into interparticle pores, b) quartz well sorted; 17065 – a) fragmented zone with interparticle pores separated by yellow dashed line, b) robust grains and quartz zone with interparticle pores. Scale bar is 5 mm

To better understand the rocks in the RT4 cluster, the thin sections were again evaluated to identify petrographic characteristics that may impact the porosity and permeability, notably the fragmentation of shells, the mineralogical composition and the types of pores. The thin sections in Fig. 4.24 were grouped according to the PCA analysis (Fig. 4.21) to facilitate the explanations of the results. Below are the main petrographic aspects associated with the NMR and PCA results.

- ***Group a*** - composed by samples showing distribution peaks in the meso/macro hybrid region. Regarding the multivariate statistical analysis, the samples are influenced mostly by micropores and meso/macropores. According to their thin sections, we classified the largest pores as vugs and moldic pores. These pores were formed by complete or partial dissolution of particles and mineral grains that were part of the initial constitution of the rock, thus benefitting the storage of fluids. The thin sections were composed by grains and particles, medium to coarse-grained sand, poorly sorted. Associating the information obtained by the methods, we realized that samples 68.65, 82.05 and 93 are more similar: the NMR results showed overlapping T_2 distribution peaks, while the PCA identified that these samples clustered close to the negative PC1 axis. This evidence signifies that even with large pores, the factor that most impacted the permeability is good connectivity through micropores. This connection is strongly influenced by an increase in the tortuosity, reflected by a poor selection of shells and mineral grains.

- ***Group b*** - composed of samples 102.55 and 162.50 showing T_2 curves within the mesoporosity region (between 100 and 1000 ms). The PCA analysis indicated that these samples are displaced in relation to group *a* by remaining closer to the positive axis of PC3, thus indicating the influence of the micropore and meso/macropores. The dense packing of the components is consistent with evidence from the thin sections suggesting that the samples suffered from physical compaction. The compaction caused shell fragmentation to produce medium to coarse-grained, moderately sorted sand. Most of the pores were classified as intraparticles and moldics, being the result of dissolution suffered by the samples. One can verify the similarities among them when integrating the results, which exhibited almost overlapping distribution peaks. Sample 162.50 contained more moldic pores, probably causing a larger pore volume region as compared to the intraparticle pores that dominated sample 102.55. Compared with RT3, the permeability reduction is the result of narrower throats and micropores sizes as verified by the PCA, probably reflected by physical compaction as evidenced by the thin sections. Even with the dissolution of shells and the formation of meso- and macropores, flow remained more difficult due to the narrow throat diameters,

causing permeabilities of 165.80 mD and 93.88 mD for samples 102.55 and 162.50, respectively.

- ***Group c*** - composed of samples 94.4 and 170.65 exhibiting the most distinct T_2 curves of the RT4 samples as marked by the dashed lines in Fig. 4.20. The NMR results showed that their pores varied between micropores and meso/macro (approximately 1 to 3000 ms). The PCA analysis placed these samples in the positive quadrant of the two principal components. Sample 94.4 was closest to the positive maxima of PC1, indicating an almost uniform influence of pores from micro to meso, while sample 170.65 was closest to the positive maxima of PC3, thus pointing to strong influence of micropores and meso- to macropores. The thin sections further helped to understand the previous results. Sample 94.4 is typical of siliciclastic rocks: a large amount of siliciclastic material, very fine to fine sand, rounded to subangular, well sorted. The shells are fragmented, very coarse sand to granule, well sorted. The pores mostly interparticle. All available information, including the NMR and PCA studies, suggest these samples to be siliciclastic with a relatively homogeneous pore-size distribution. Compared with RT3, the permeability reduction is due to the high fragmentation of the shells caused by diagenetic actions that reduced the pore throats. The presence of fragmented particles and very small siliciclastic minerals (very fine to fine sand size) directly impacted the flow through the pores. Sample 170.65 also exhibited siliciclastic rock characteristics, with a large amount of siliciclastic minerals, very coarse sand to granular, subangular to angular, and moderately sorted. On the other hand, the shells were completely fragmented and medium sand to coarse-grained. Mostly interparticle pores and vugs were observed. All information, including the NMR and PCA analyses, again points to siliciclastic rocks characteristics, just like the previous sample. However, the bimodal distribution observed in the NMR curve is directly linked to the two main types of pores that can be seen in the thin sections: interparticle pores associated with the peak of relaxation times in the mesopore region, and vugs associated with the distribution peak in the meso/ macropore region. Compared to RT3, RT4 showed a reduction in the permeability probably caused by an increase in tortuosity. Due to high fragmentation of the shells and the angularity of the siliciclastic grains, the flow paths became more distorted, directly impacting the permeability. Sample 170.65 still showed the

highest permeability (243.20 mD) and porosity (20.19%), probably a result of its loose packing.

The mineralogical composition as determined from the thin sections confirmed that most of the minerals were calcites; however, siliciclastic materials were also observed, similarly as in the other groups. Samples 94.4 and 170.65 showed more siliciclastic material, exhibiting siliciclastic rock morphology. For this reason, XRD experiments was used additionally to define and quantify the entire mineralogy of the samples.

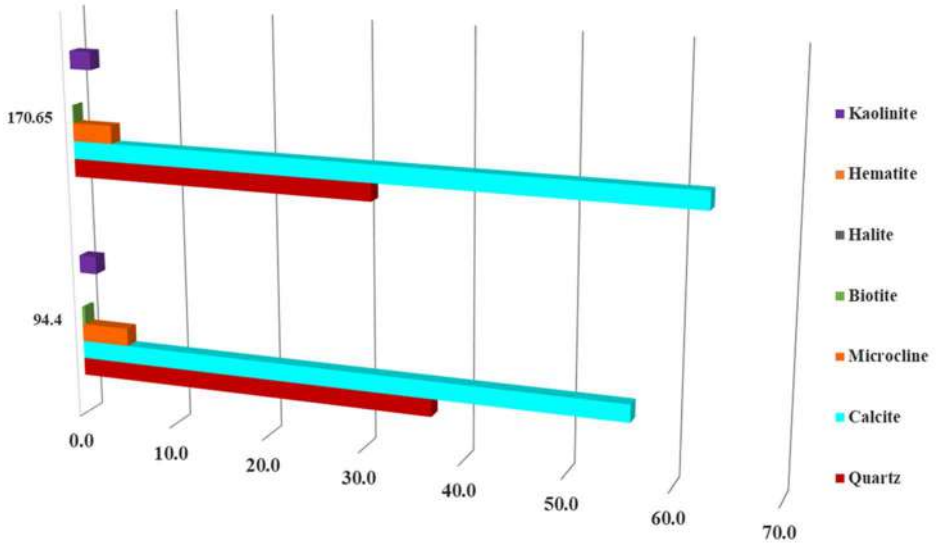

Figure 4-24 – Results of XRD from samples 94.40 and 170.65

Figure 4.25 shows the results of the XRD experiments, again using the Rietveld method. As with most cases before, samples 94.40 and 170.65 indicate a predominance of the mineral calcite, 56% in sample 94.4 and 63% in sample 170.65. Quartz was also present, 36% in sample 94.4 and 30% in sample 170.65. Another siliciclastic mineral, microcline, was also found, 4.8% in sample 94.4 and 4.5% in sample 170.65. Kaolinite clay was further present in the two samples (about 2.5%), caused by the alteration of siliciclastic minerals. Unlike with the other groups, these siliciclastic minerals changed the petrophysical characteristics, mainly in the pore-size distributions. However, the permeability remained similar as those of the other samples grouped in this rock type.

4.2.5 Characteristics of Rock Type 5 (RT5)

Rock type 5 represents the last group of samples with a relatively high permeability, as noted earlier. This rock type showed slightly lower permeabilities but higher priorities that rock types RT3 and RT4 (Fig. 4.3). For these reasons they were grouped together to clarify their specific petrophysical behavior in terms of influencing fluid flow in the system. Table 4.6 presents petrophysical information and petrographic characteristics of the two samples making up the RT5 group. The data in this table show that the two samples have the highest porosities of all samples that were studies, about 24%. The permeabilities of 84.4 mD and 152.96 mD and the $T_{2Logmean}$ times are close to or only slightly lower than those of the RT4 range.

Table 4-6 – Petrophysical and geological properties of Rock Type 5

Sample	Φ_{Rout} (%)	K (mD)	$T_{2Logmean}$ (ms)	Shells Frag. (%)	Silicic. Min. (%)	Pore Class.
71.3	24.7	152.9	210.3	30	30	Intraparticle (40%) Vug (30%)
99.5	24.9	84.1	105.7	100	50	Moldic (70%)

Similarly, as for the other groups, graphs of the NMR results were generated for the two RT5 samples. Figure 4.26 provides a plot of the T_2 distributions of samples 71.3 and 99.5. They show a clear predominance of pores in the hybrid meso/macroporosity region. The $T_{2Logmean}$ values (105.74 ms and 210.3 ms of samples 71.3 and 99.5) were still within the range of variation of the RT4 samples, but mostly lower than the RT3 values, which is consistent with the decrease in permeability when compared to RT3.

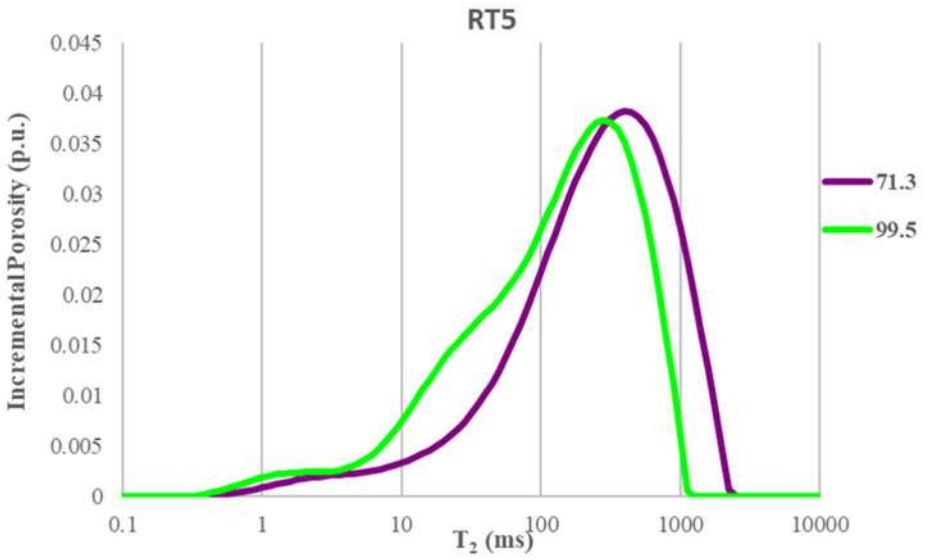

Figure 4-25 - Plot showing T_2 distributions curves for the RT5 samples

The NMR curves indicate that the samples have very similar pore-size distributions, which almost overlap at around 300ms. The shift in the curve to the left of sample curve 99.5 reflects a slight decrease in the pore sizes, as compared to sample 71.30. Still, the two curves are very similar, implying that the samples as such are very similar also. To ascertain this, multivariate statistical analysis was again applied using the bins resulting from the NMR. Figure 4.26 shows the graph of scores for the variables for the entire set of rock samples, with the RT5 samples identified in pink.

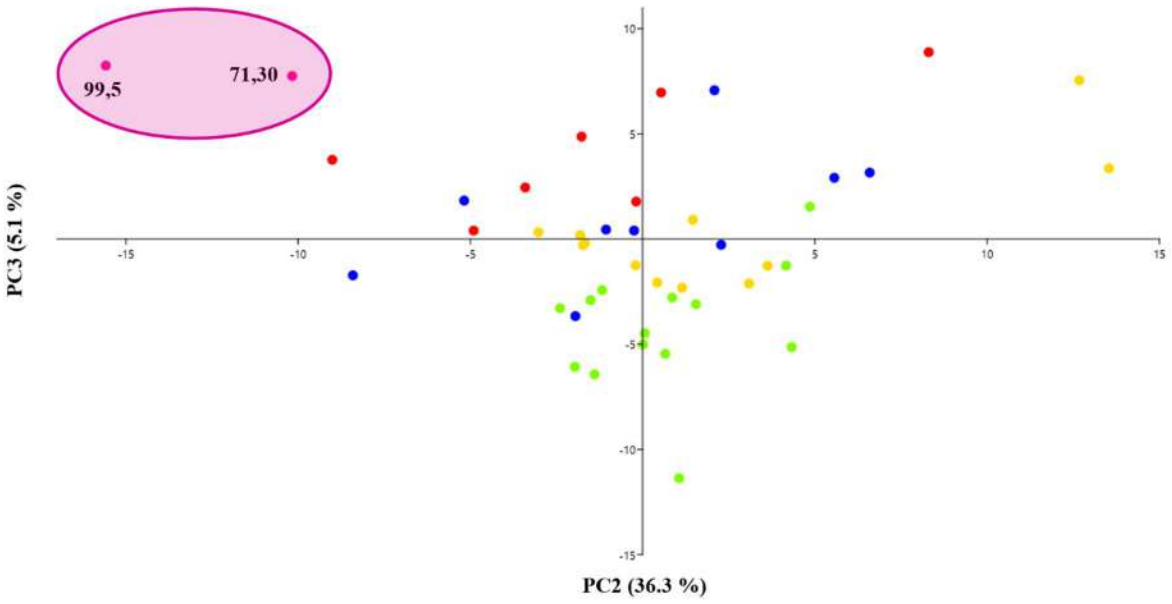

Figure 4-26 – Plot showing scores for all samples. The samples from RT5 are concentrating at - x axis (PC2) and + y axis (PC3)

As with the other rock types, the combination of principal components that best characterized the RT5 samples was evaluated. In this grouping, the PC2xPC3 graph was able to cluster the two samples together. The loadings graphs of the principal components were used to interpret the scores graph. Since the samples were close to each other in the upper left quadrant, but away from the two axes, the loadings graphs of the PCs were analyzed together to better interpret the statistical results of the two samples. The results are plotted in Fig. 4.27.

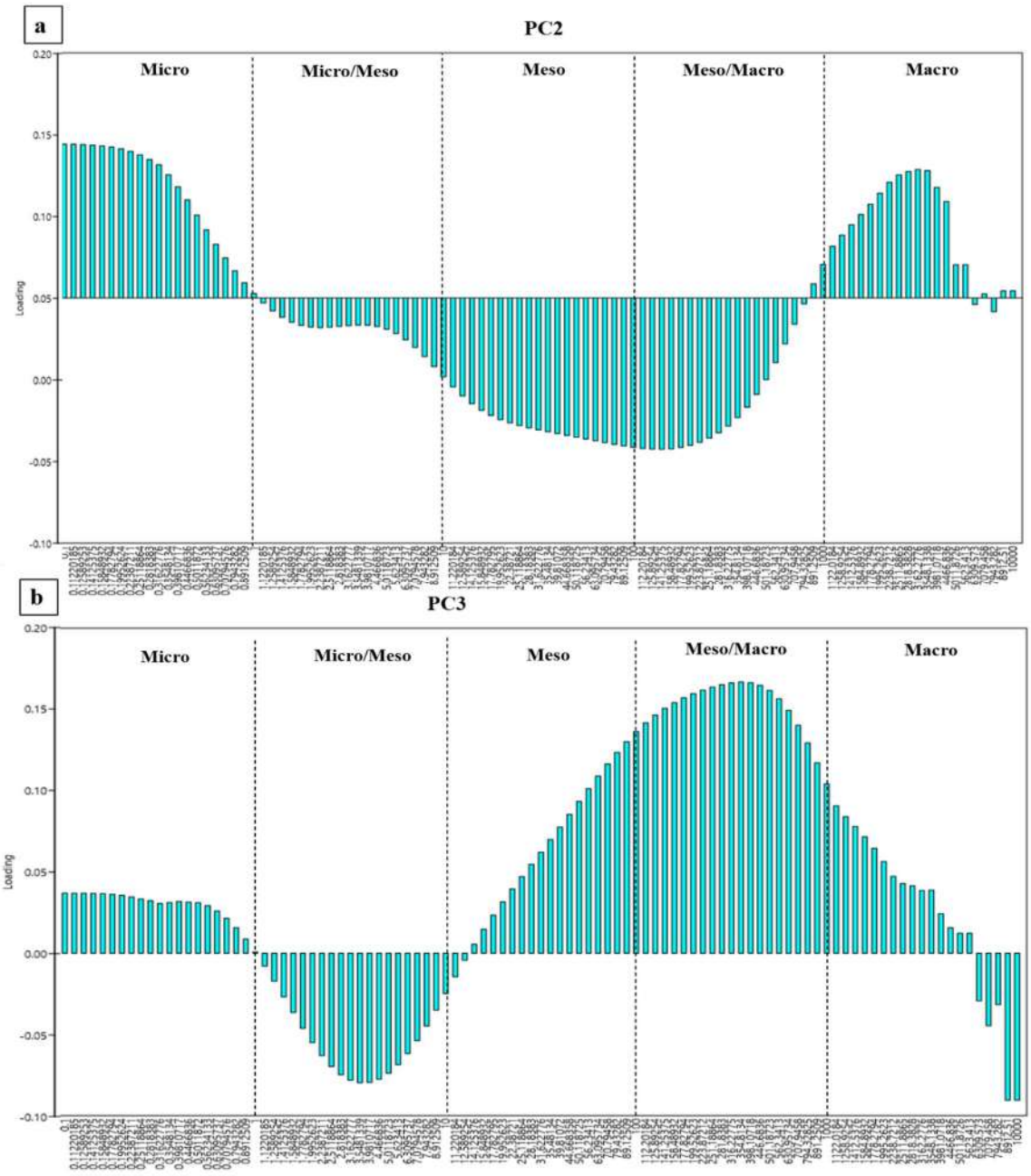

Figure 4-27 – Samples 71.30 and 99.50 are clustered in the negative PC2 and positive PC3 quadrant: a) at PC2 negative highs relative to micro/meso to meso/macro pore size zones; b) at PC3 positive highs relative to micropores and meso to macro pore size zones

The graphs of scores in Fig. 4.26 show that the samples are placed together in the negative quadrant of PC2 and in the positive quadrant of PC3. The component loadings graphs (Fig. 4.27) suggest that the high negatives of PC2 correspond to the mesopore to meso/macropore partitions (from 10 to 1000ms) manly. The PC3 principal component, on the other hand, indicates that the samples agglomerated in the positive quadrant have influence by micropores (0.1ms to 1ms) to meso/macropore (from 100ms to 1000ms) region manly.

Relating these responses to those acquired using NMR indicates that pores in the meso/macropore partition most influenced the two samples in terms of contributing to flow in the pore system. Since they presented the highest porosities of all samples in this study and are not associated with an increase in the permeability, petrographic analysis using thin sections becomes essential for understanding this unique characteristic. Figure 4.28 shows thin sections of the two RT5 samples in attempts to highlight some of the geologic characteristics that impact porosity and permeability, notably shell and pore morphology, mineralogical composition, and pore classification.

We noted earlier that sample 71.3 exhibited a T_2 curve in the hybrid meso/macropore region, with the influence of pores in the meso/macro transition region being identified by PCA (those pores were classified as intraparticle and vugular pores). The 99.5 sample also exhibited a T_2 curve in the hybrid meso/macropores region, and it was possible to identify this influence of the meso/macropore region using the PCA analysis, while the petrographic analysis classified them as mostly moldic. Both the action of dissolution, which caused the formation of most of the pores observed in the thin sections, and physical compaction, which caused the fragmentation of particles and grains, influenced the reduction in the permeability of the samples. The slight displacement of the relaxation peak of sample 99.5 was probably caused by the high rate of fragmentation (100%), which generated small particles and very angular grains and thus impacted the size of the pores formed. The increase in porosity with a decline in permeability can be directly linked to the connection of these larger pores, as verified in all of the techniques that were used. Even with an abundance of meso- and macropores, some microporosity was present, as reported by the PCA, which may have been responsible for the connectivity of the pore system. Hence, notwithstanding having many large but mostly isolated pores, their connection occurred through very small pores which still reduced the permeability. Another important aspect is the presence of grains and

angular particles in the rocks. Angulation of the rocky framework causes an increase in the tortuosity of the system, causing a decrease in flow.

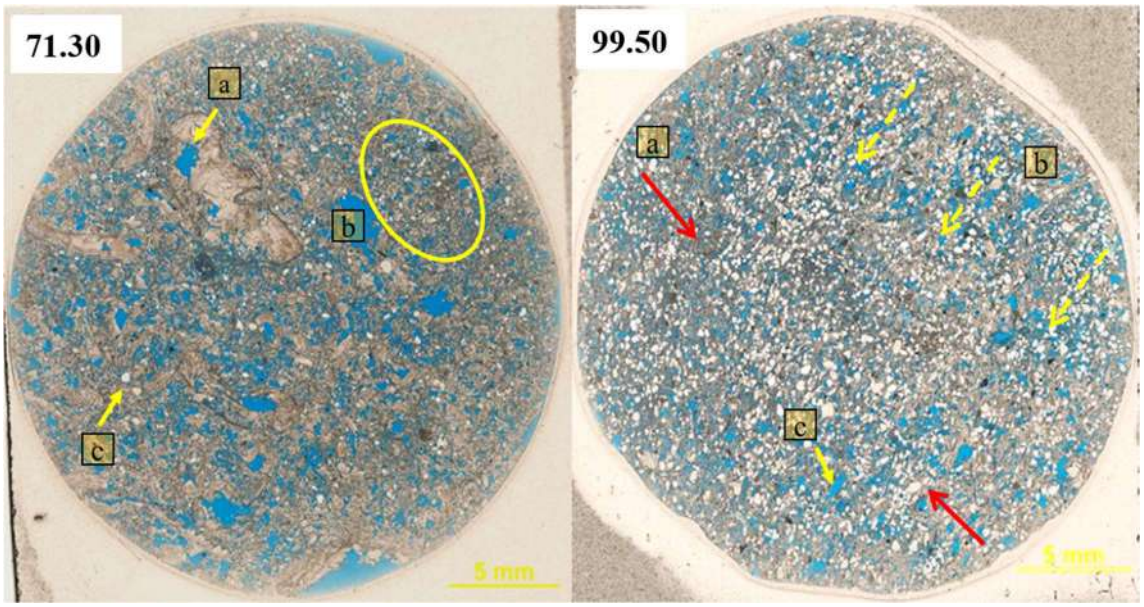

Figure 4-28 – Thin sections of the RT5 samples (parallel niçois). Some features are highlighted: 71.30 – a) intraparticle pore, b) fragmented shells and silicate minerals, c) quartz grain; 99.50 – a) compacted orientation (red arrow), b) grains orientation (yellow arrow), c) moldic pore. Scale bar – 5 mm

The analysis above indicates that the samples could be grouped successfully into their respective rock types, using a range of techniques, even though certain variations were observed, sometimes petrophysical, sometimes petrographic. Various aspects, such as the connectivity and pore size differences within the clusters, were evaluated better using other techniques in attempts to resolve remaining questions and to obtain accurate information for obtaining good estimated of the permeability.

With the rock types characterized, the next step in this research was to correlate the NMR generated pore-size distributions with the radii of the pore throats obtained using mercury injection capillary pressure (MICP) methods. From this integration, important information about the characteristics of the samples could be identified. A more comprehensively analysis was further made to study the connectivity of the pore system by quantifying the distribution of pore bodies and throat sizes and their impact on the relationship between porosity and permeability. The totality of results obtained using NMR and MICP is of very helpful for microtomography analyses by improving the quantitative description of porous media at the pore level and contributing to the simulation of fluid flow in the subsurface.

4.3 The Connectivity Of Pore Systems

This part of the research aims to estimate the permeability by adapting the main equations found in the scientific literature to coquinas. To improve these equations, the samples initially were separated into rock types to bring together rocks with similar petrophysical characteristics, thereby facilitating the quantification of possible flow processes in the set. Unfortunately, the high variation in pore geometry and the lack of correlation between pore body and pore throats make it difficult to accurately correlate porosity and permeability.

For the characterization of rock types, NMR experimental data offered one way of comparing samples in their respective groups. The results consisted of the distributions of the connected pore system of the samples, encompassing both the pore bodies and the pore throats, the latter being responsible for the connectivity within the porous medium. Even when showing certain similarities, several samples exhibited also contradictory details, which required complementary analyses to better group the various rock types. For example, petrographic analyses showed that samples with pores classified as intraparticle and moldic, with considerable sizes and well-marked T_2 curves, often did not have high permeability values. This finding contradicts the customary assumption that porous media made up of larger pores would allow easier fluid flow. One possible reason for the lower permeability of these rocks could be the narrowing of the pore throats that connect the large pore bodies formed by macropores, as discussed already in section 4.2. To study the pore throats of the samples more precisely, this section 4.3 focuses on capillary pressure-saturation curves as measured using mercury injection techniques.

4.3.1 Capillary pressure by mercury injection technique

Reliable knowledge of pore throats in a natural porous media is especially important for carbonate rocks, which often exhibiting heterogeneous multimodal pore systems. To study this problem, capillary pressure by mercury injection (MICP) techniques were used to determine the pore throats of the samples in the set. Since MICP is a destructive technique, its application to the entire set of samples was unfeasible and hence only a limited number of samples could be used to explore this problem. The porosity versus permeability plot of Fig. 4.3, which earlier formed a basis for the development of rock types, was used to create sample comparison trails that had the same

porosity but different permeabilities and vice versa. Figure 4.29 shows a plot of the rock types as well as of the trails developed for the comparisons to optimally select the samples for the MICP analyses. To have good representativeness of the set, samples from all groups were chosen to cover the different relationships that are possible between porosity and permeability.

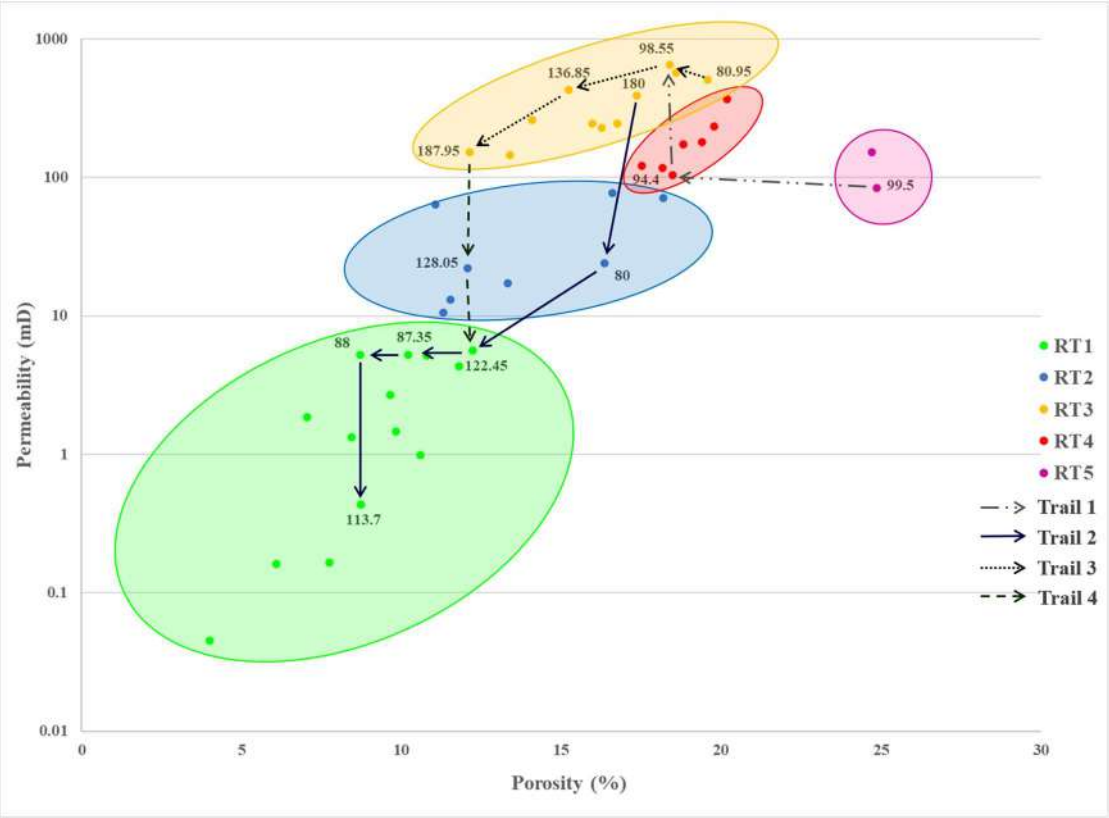

Figure 4-29 – Plot showing the rock types based on porosity and permeability from routine core analysis. The marked trails were used to select samples to understand the different relationships between porosity and permeability

Table 4.7 lists the routine core analysis data separated according to the trails that were selected. The data show that trail 1 was created to include the pore system showing increased permeabilities at lower porosities (within a group of samples having high permeabilities). For this, samples 99.5 (RT5), 94.4 (RT4) and 98.55 (RT3) were used. Trail 2 includes a larger number of samples to compare the those showing a decrease in the permeability (up to three orders of magnitude) at lower porosities. The samples chosen for this were 180 (RT3), 80 (RT2), 122.45, 87.35, 88 and 113.7 (RT1).

Trail 3 was designed to understand samples clustered in RT3, which had the highest permeability values. The chosen samples were 80.95, 98.55, 136.85, 187.95. And finally, trail 4 was created to better understand why samples with the same porosity could

have permeabilities varying by three orders of magnitude. For this analysis, samples of three different rock types were used, namely 187.95 (RT3), 128.05 (RT2) and 122.45 (RT1).

Table 4-7 – Details of trails constructed to understand different correlations between porosity and permeability

Trails	Samples	Φ_{Rout} (%)	K_{Rout} (mD)
1	99.5	24.9	84.0
	94..4	18.4	103.5
	98.55	18.4	649.9
2	180	16.8	245.1
	80	16.3	24.1
	122..45	12.23	5.7
	87.35	10.2	5.3
	88	8.7	5.2
	113.7	8.7	0.4
3	80.95	19.6	504.4
	98.55	18.4	649.9
	136.85	15.9	244.9
	187.95	12.1	152.4
4	187.95	12.1	152.4
	128.05	12.1	22.1
	122.45	12.2	5.7

By injecting mercury stepwise at incremental pressures into a rock medium, MICP techniques may be used to construct curves of the capillary pressure as a function of mercury saturation. The amount of mercury intrusion at the different pressures to which the samples are submitted detail how difficult it is to access the various pores, initially the larger pores but then increasingly the smaller pores of the rock sample. The resulting capillary pressure (Pc) – saturation (S) curves can be compared to assess differences in the pore systems of the samples.

Figure 4.30 shows the Pc-S curves of the samples along trail 1. As mentioned earlier, trail 1 was used to analyze samples with large changes in the permeability with only small porosity variations. According to Table 4.7, sample 98.55 had the highest permeability of the group (649.91 mD at a porosity of 18.4%), followed by sample 94.4 (103.49 mD at 18.48% porosity), and sample 99.5 (84.04 mD at 24.8% porosity). The

curves in Fig. 4.31, plotted in the sequence as they appeared along trail 1 in Fig. 4.30, show an increase in capillary pressure consistent with the entry of mercury into pores having smaller diameters. Sample 98.55 required less pressure than the other samples to access the various pores. Following the order of the curves, mercury intrusion into sample 99.5 required a higher pressure, which may be interpreted as resulting from a reduction in the openings of the pore throats of this rock. The third curve, for sample 94.4, shows a relatively large difference in the pressure when mercury begins to intrude the medium, thus suggestion lots of very small pores (the pore throats).

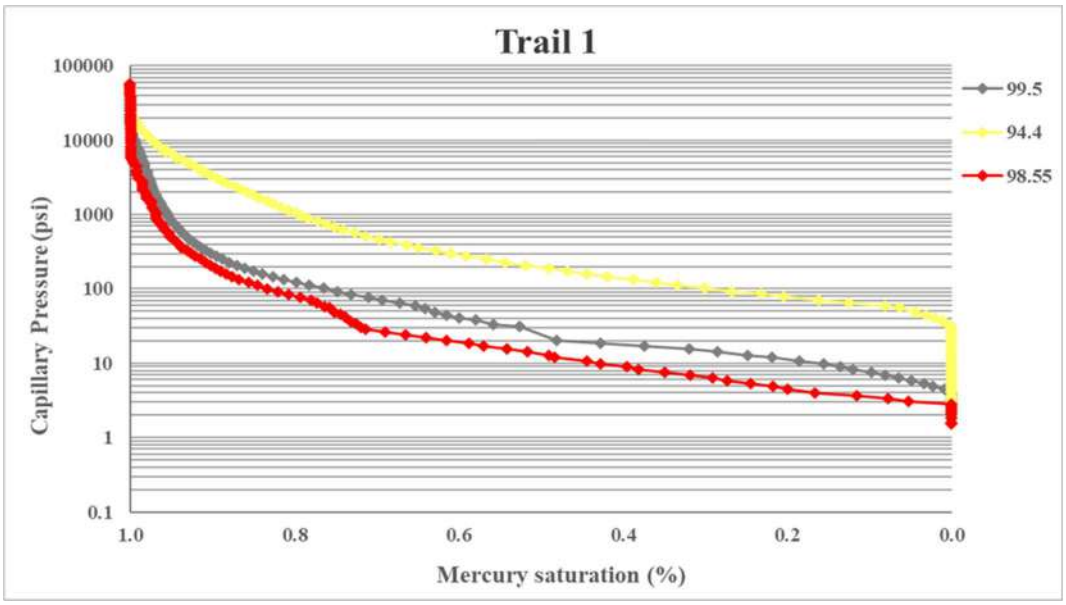

Figure 4-30 – MICP-generatde capillary pressure curves as a function of mercury saturation for the samples along trail 1. Notice the differences in pressure when mercury intrudes the pores at similar saturations. Sample 98.55 had a higher permeability than the other samples.

The characterization of sample 98.55 in section 4.2.3 showed that NMR provided a mean T_2 value of 398 ms, while the PCA statistic indicated a strong predominance of meso/macropores. Analysis of the thin section also showed relatively large pores, classified as vugs, due to strong diagenetic actions endured by this rock. The MICP results confirm that dissolution favored fluid flow within the sample by increasing the diameters of the pore throats.

The analysis of the RT4 samples in section 4.2.4 indicated that sample 94.4 had different characteristics from the others in the grouping in terms of the combined NMR, PCA and thin section results. Sample 94.4 was found to be different because of a reduction in the granulometry of the grains and particles, leading to a reduction in the pore throats, a fact confirmed by the MICP data. It is noteworthy that sandstones, in their

majority, present a more simplified petrophysical response regarding reservoir productivity. This because well-distributed grains lead to more homogeneous pore system, thereby facilitating the percolation of fluids. This concept holds for sample 94.4 in that the relative uniformity of the pore space of this sample improves hydraulic behavior and maintains a high permeability.

Sample 99.5 exhibited similar MICP behavior as sample 98.55, with only a small difference regarding the required pressure and the initial point of intrusion. The analysis in section 4.2.5 indicated a predominance of pores in the hybrid region of meso/macropores, classified mostly as moldic. The analysis then also indicated near-total fragmentation of the shells, leading to small angular particles that increased the tortuosity of the pore system. The MICP results revealed initial intrusion at a pressure value of about 5 psi, with pressure increments compatible with the narrowing of the pore throats, while also showing a significant rise in the curve at 80 psi, when about 70% of the pores were already filled.

As shown here for trail 1, one may conclude that rocks made up of small pores, which require an increase in the capillary pressure to enable the percolation of fluids, not always lead to a low permeability. Mercury intrusion in sample 98.55 started at 3 psi, while a slight increase in pressure to about 28 psi already caused about 70% of the pores to be accessed, thus confirming the presence of larger pore bodies and pore throats within the system. Intrusion in sample 99.5 started at 5psi, and caused a slightly greater slope in the curve as compared to sample 99.5 in that about 70% of the pores were already accessed with pressures up to 80 psi, thus demonstrating a reduction of the pore throats of this sample. Intrusion in sample 94.4 started at 34 psi, much higher than those of the other samples, while also requiring much larger pressures (about 500 psi) to saturate 70% of the pores. This confirms the presence of much smaller pore throats.

The analysis above indicates that the differences in permeability are related to the widths of pore throats, the tortuosity, and the connectivity of the pore system, but not necessarily to the amount or total volume of pores in the system. Regardless of the size of the pore bodies in the samples, when there is a reduction in the width of the pore throats, the impact on the permeability is inevitable. The decrease in permeability can also be seen when the sample contains more angular grains, which cause a more twirling porous network that hinders the passage of fluid. However, when the rock system is more homogenous by containing pores with similar sizes, fluid flow increases.

Contrary to the samples of trail 1, the samples along trail 2 show a rapid decrease in permeability with only modest reductions in the porosity. Fig. 4.31 shows the capillary pressure curves for the trail 2 samples. The curves show an increase in capillary pressure as the smaller pores are being intruded by mercury. The data in Table 4.7 indicated that sample 180 had the highest values of porosity and permeability of trail 2. This is reflected also by the capillary pressure curve of this sample, which showed the initial intrusion to occur at 2 psi, while about 80% of the pores were saturated with pressures up to 85 psi. As noted in section 4.2.3, RT3 sample 180 showed a predominance of macropores and a relatively high value of $T_{2Logmean}$, with pores classified as vugs, mostly due to dissolution. The MICP results support the finding here that the diagenetic process of dissolution caused an increase in the diameter of the pore throats, and hence a relatively high permeability.

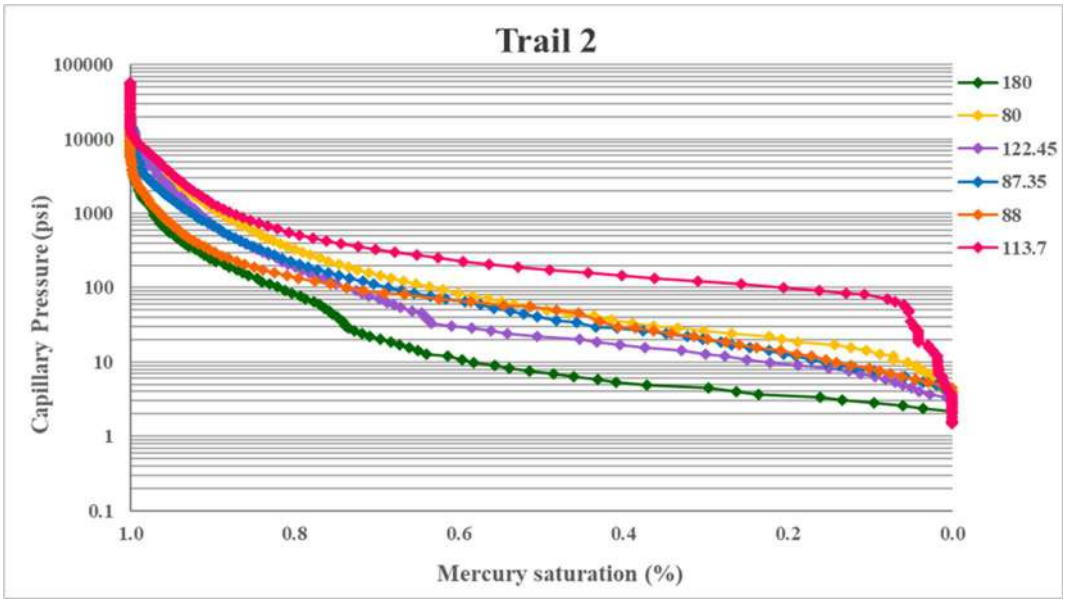

Figure 4-31 – MICP-generated capillary pressure curves as a function of mercury saturation for samples from trail 2. Can be noted the difference between intrude pressures into the pores. Sample 180 has higher permeability and 113.7 has the lower permeability compared to the other samples

The next sample on trail 2 is sample 80 (Fig. 4.29). This sample has a very similar porosity (16%) as sample 180, but a much lower permeability (22.93 mD) as shown by the petrophysical data in Table 4.7. According to the capillary pressure curve, mercury started to intrude the pores of sample 80 at about 4 psi, after which saturation increased smoothly with increasing pressures until reaching a saturation of 80% at a pressure of about 300 psi. Notice the considerable shift in the curve as compared to sample 180, thus confirming a significant reduction in the pore throats of this sample. In section 4.2.2,

where the RT2 samples were characterized, the pore system of sample 80 was found to have the lowest mean of $T_{2Logmean}$ in the group, with a predominance of moldic pores resulting from the dissolution of particles and the fragmentation of 80% of the shells due to compaction suffered by this sample. These characteristics caused a major reduction in the pore throats. The MICP results confirm this finding that shell fragmentation will lead to much smaller particles and micritization of the original rock structure to considerably reduce the permeability.

The next sample on trail 2 is sample 122.45. This sample had a slight lower porosity compared with the others, and a permeability of 5.65 mD (an order of magnitude lower). Fig. 4.31 shows that the capillary pressure curves in sample 122.45 is positioned just above the curve of sample 180. The intrusion of mercury started at 3 psi, while 80% of the pores are filled at a pressure of 200 psi, much higher than with sample 180, which reflects a reduction in the opening of throats. Sample 122.45 was part of RT1, characterized as having a bimodal pore size distribution with the pore relaxation peaks in the hybrid micro/meso region and the hybrid meso/macro region. Its relaxation averages are lower than those of sample 180, but greater than sample 80. These findings indicate a strong influence of pores from the meso/macro region, with a predominance of whole shells, granules to fine pebbles, and strongly compacted. Compaction helped to reduce the pore sizes, which is confirmed by the MICP results. Comparing these data with those of the other samples, especially sample 80, confirms that physical compaction without much fragmentation of the shells, impairs flow through the pore network and reduces the permeability.

The next two samples along trail 2 (87.35 and 88) belong to RT1. Similarly, as sample 122.45, these samples have permeabilities of about 5 mD, but differ in their porosity: 12.23%, 10.27% and 8.7% for samples 122.45, 87.35 and 88, respectively. Samples 87.35 and 88 previously (in section 4.2.1) showed bimodal pore-size distributions with a strong influence of mesopores between 10 – 100 ms. The reduction in porosity between samples 122.45 and 87.35 may be due to the presence of small fragments and large shells, which reduced the pore space. A detailed view of sample 88 further revealed an abundance (60%) of whole shells having granule to fine pebble sizes. A first phase of diagenesis was identified, involving the cementation of shells, while physical compaction later created interparticle pores. From the comparison of samples 87.35 and 88, one may conclude that compaction associated with cementation was primarily responsible for the reduction in porosity, while the re-orientation and

fragmentation of large shells had lesser effect on the permeability. The pressure-saturation curves of the two samples closely overlapped at low mercury saturations, with an initial pressure of 4 psi, until about 80% of the pores are filled. From there, the curves started to separate, with sample 87.35 exhibiting a greater pressure increase as 30% of its pores had smaller diameters.

The last sample analyzed on trail 2 was sample 113.70, which had a porosity of 8.72%, the same as sample 88, but a much lower permeability, 0.43 mD versus 5.21 mD. The difference between the pressure curves in Fig. 4.31 is evident: while intrusion started at 3psi, an abrupt increase in pressure occurred, with the sample requiring about 80 psi to intrude only 10% of the sample. Sample 113.7 was characterized in section 4.2.1, showing a unimodal pore distribution, with whole shells oriented and fine pebbles which made up 30% of the visual total. Shell fragments were also found, coarse to medium sand, and fine siliciclastic grains, medium to fine sand, with physical compaction shaping the shells. Most of the pores were classified as interparticle. The most noticeable characteristic of the pore system of this sample was the compaction of shells, and the presence of smaller fragments of grains and particles, leading to less connectivity and more complex flow paths. These effects cause an increase in the tortuosity and narrower pore throats, thereby impacting the permeability.

The next trail considered is trail 3. This trail, composed of samples having very high permeabilities, was used to better understand differences between the samples that make up RT3. Figure 4.32 shows the capillary pressure curves of the trail 3 samples, while Table 4.7 lists the basic petrophysical properties. The trail initiated with sample 80.95 sample, which has 19.57% porosity and 504.37 mD permeability. The capillary pressure curves of this sample show that pore intrusion started at 3 psi, while 10% of the pores were intruded with mercury using a pressure of 10 psi and 80% of the pores at a pressure just below 272 psi. The NMR results of sample 80.95 in section 4.2.3 showed a pore system consisting mostly of macropores, as confirmed also by the PCA statistics. The pores were classified as moldic and vugular, with fragments of shells and mineral grains, and containing fine to medium sand between the whole shells. The main diagenesis of the sample is dissolution, an effect that benefits the enlargement of the pore system and increases the permeability.

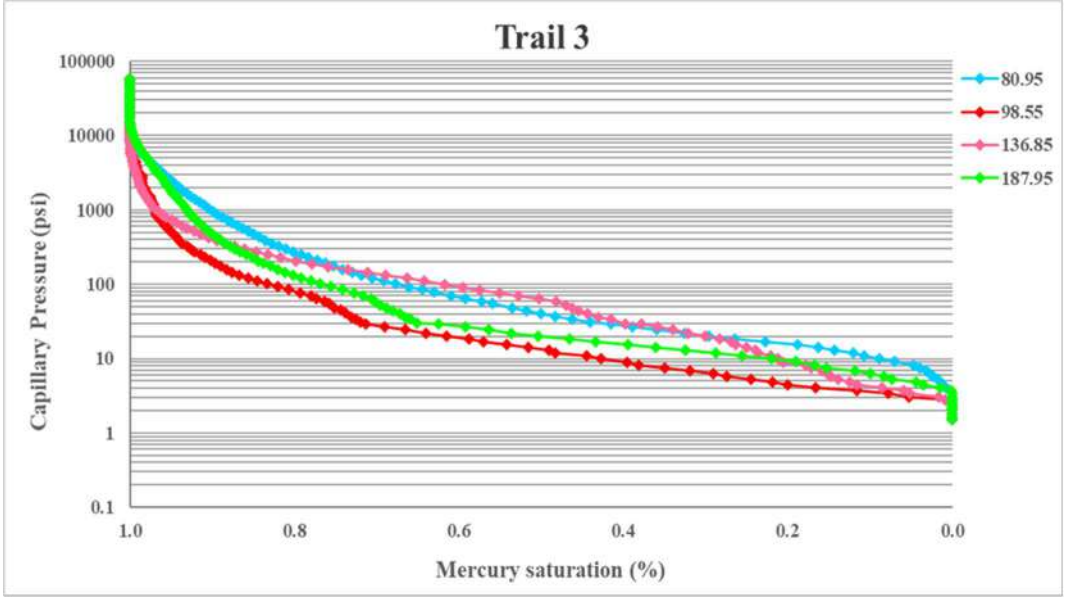

Figure 4-32 – MICP-generated capillary pressure curves as a function of mercury saturation for samples from trail 3. The surves show differences among the intruded pressures into the pores. Sample 80.95 has a higher permeability and 187.95 has the lower permeability compared to the other samples

Sample 98.55 along trail 3 was examined next. Its petrophysical data indicated a reduction of 1% in porosity, and an increase of approximately 25% in the permeability as compared to sample 80.95. Sample 98.55 contained a predominance of macropores, similarly as sample 80.95. Sample 98.55 consisted for 90% of preserved whole shells, granules to fine pebbles without orientation, and a few percentages of fragmented material and very coarse sand. As for sample 80.95, dissolution was very strong, being the most striking diagenetic process in the thin section, leading to an increase in the percentage of vugular pores. This indicates that low fragmentation of the sample constituents, as well as the increase in pore size, enhanced the connectivity of the system, and increased its permeability. This difference is reflected also by the sample's capillary pressure curve. Sample 98.55 required a very pressure for initial intrusion, thus reinforcing the notion that its pore throats are larger than those of the other samples. Moreover, 80% of the pores were filled with mercury at pressures just below 84 psi, which further explains the increase in permeability.

The next sample on trail 3 was sample 136.85, having a porosity of 15.97% and a permeability of 244.97 mD. Both parameters were lower as compared to sample 98.55. The capillary pressure curve showed evidence that the sample consisted of pores with smaller diameters in that 80% of the pores had been accessed with a pressure of about 226 psi. The characterization of RT3 sample 136.85 in section 4.2.3 indicated an

abundance of macropores, with some contributions of micropores. The petrographic properties showed a reduction in the amount of whole shells (65%), and granules to fine pebbles with concordant orientation. The remainder (35%) consisted of fragmented shells, medium to coarse-grained sand, as well as siliciclastic material, fine to very coarse sand, had low selection and angulation. Blocky cementation was identified as fill of the moldic pores, as well as poikilotopic calcite cementation, which cemented various grains and fragments. The vug pores were formed mostly by shell dissolution and shell fragmentation. A comparing of samples 136.85 and 98.55 suggests that the reduction in the throat diameters of sample 136.85 was due to more effective cementation, leading to smaller pores as compared with sample 98.55, and hence a lower permeability.

The last sample of trail 3 was sample 187.95, with had a lower porosity (12.14%) as well as a lower permeability (152.43 mD) compared to the other trail 3 samples. The MICP graph in Fig. 4.3 shows that pore intrusion started at about 3 psi, and that 80% of the pores were filled at pressures of 110 psi, less than the previous sample. The petrophysical characterization in section 4.2.3 indicated a predominance of macropores, while shells in the thin sections remained intact, with also showing granules to fine pebbles. The pores, mostly classified as vugular, were a result of dissolution, as with the other RT3 samples. The difference involves physical compaction and cementation, which are the most impactful diagenetic processes of sample 187.95. These different phenomena all contributed together to cause a decrease in the connectivity between pores and narrowing of the pore throats. One may conclude that the high permeability of all RT3 samples is due to dissolution processes, which increased the pore body and pore throats radii and facilitated more flow. Still, an increase in cementation and compaction may narrow some of the pore throats and lower the connectivity.

The last trail (trail 4) was created to better understand the behavior of the samples of three different rock types in terms of major reductions in the permeability (three orders of magnitude), while maintaining the same porosity values. Fig. 4.33 compares the capillary pressure curves of the three samples (187.95, 128.05 and 122.45) making up this trail. They showed an increase in capillary pressure as smaller pores were being intruded by mercury. Sample 187.95 had the highest permeability, 152.43 mD. In section 4.2.3, this sample was characterized as having a unimodal pore distribution, with a predominance of macropores. The sample is made up of whole shells, granules to fine pebbles. The pores were classified as vugular, mostly as a result of dissolution. Some evidence of cementation and physical compaction was also present

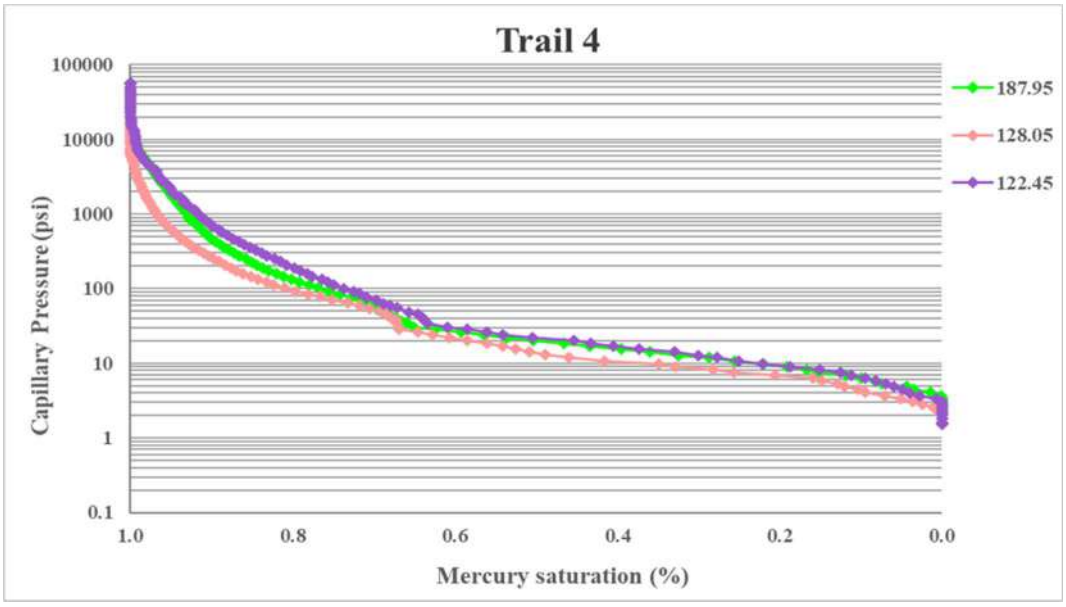

Figure 4-33 – MICP-generated capillary pressure curves as a function of mercury saturation for samples from trail 4. The surves show differences among the intruded pressures into the pores. Sample 187.95 has a higher permeability and the 122.45 has a the lower permeability, compared to the other samples

Sample 128.05 had the same porosity value as sample 187.95, but one order of magnitude lower permeability. Sample 128.05 showed a slightly bimodal pore-size distribution, indicating a predominance of pores in the meso/macro hybrid region, but with far fewer macropores than sample 187.95. Sample 128.05 consisted of whole shells, granules to fine pebbles, and very micritized medium-sand sized shell fragments. The shells were compacted, leading to a narrowing of the pore throats, increased tortuosity within the pore system and less connectivity between the pores, and consequently a lower permeability.

The last sample analyzed was 122.45, which had the same porosity (about 12%) as samples 128.05 and 187.95, but with a marked decrease in permeability. The T_2 curve was bimodal with relaxation peaks in the hybrid micro/meso and hybrid meso/macro regions. The PCA indicated a strong influence of pores in the meso/macro region. Sample 122.45 contained a predominance of whole shells, granules to fine pebbles, strongly compacted. The reduction in permeability was again caused by compaction by reducing the pore connections, narrowing of the pore throats and increasing the tortuosity of the pore system.

The capillary pressure curves showed no significant differences in the pressures needed for mercury intrusion. Up to 70% of the pores of the samples could be filled with mercury at a pressure of about 50 psi to 187.95 and 128.05 samples, and 70 psi to 122.45

sample. From that point on, there was a gradual increase in pressures needed to fill the smaller pore throats, with sample 122.45 showing slightly narrower openings, followed by samples 187.95 and 128.05. The impact of tortuosity and smaller pore throat diameters was well evidenced for sample 122.45, which had the lowest permeability value of trail 4. Poor pore connectivity appeared to be the main reason for sample 128.05 to have a lower permeability than sample 187.95.

After the analysis using the four trails, the next step was to study the connectivity of the pore system of the various samples by means of microtomographic images. For this, the pore-size distributions obtained using NMR were integrated with the results of pore throats provided by MICP, to facilitate the segmentation of micro-CT images. The integration and the results obtained are discussed in the next section.

4.3.2 Integration of NMR and MICP

A methodology widely used for determining the surface relaxivity (ρ_2) is through adjustment of the pore-size distribution obtained using NMR, and pore throats determined using MICP. The relaxivity is a property of the relaxation mechanisms involving both the saturating fluid and the porous surface. According to KLEINBERG *et al*., (1994), ρ_2 is a function of the density of the paramagnetic centers present on the surface of the pores and the residence time of fluid molecules that are subject to action by the magnetic centers.

As stated in chapter 3, ρ_2 may be used to convert relaxation times into pore radii. Some relation is essential for transforming the T_2 dimensions into pore sizes using the assumption that pores have a cylindrical geometry (SOUZA, 2012). Knowing that rocks respond differently to ρ_2 (e.g., carbonate rocks have lower values than sandstones), this constant is essential for a more accurate analysis of the pore network when using microtomographic images. For the integration of NMR and MICP, six samples were used, namely 87.35, 88, 122.45, 136.85, 180 and 187.95.

The NMR and MICP distributions of the six samples are shown in Fig. 4.34. The parameter ρ_2 in Eq. (3.3) was adjusted until the peaks of the NMR and MICP distributions were very close. Samples 87.35, 88, 122.45, 180 and 187.95 generated reasonable adjustments for the overlapping of NMR and MICP curves by showing visual similarities between their distributions. The MICP curves suggest that the pore throats, derived using the WASHBURN equation (Eq. 3.2), describe the pore-size distributions that are

responsible for the connectivity, and hence are the main flow channels of the pore system (BASAN *et al*., 1997).

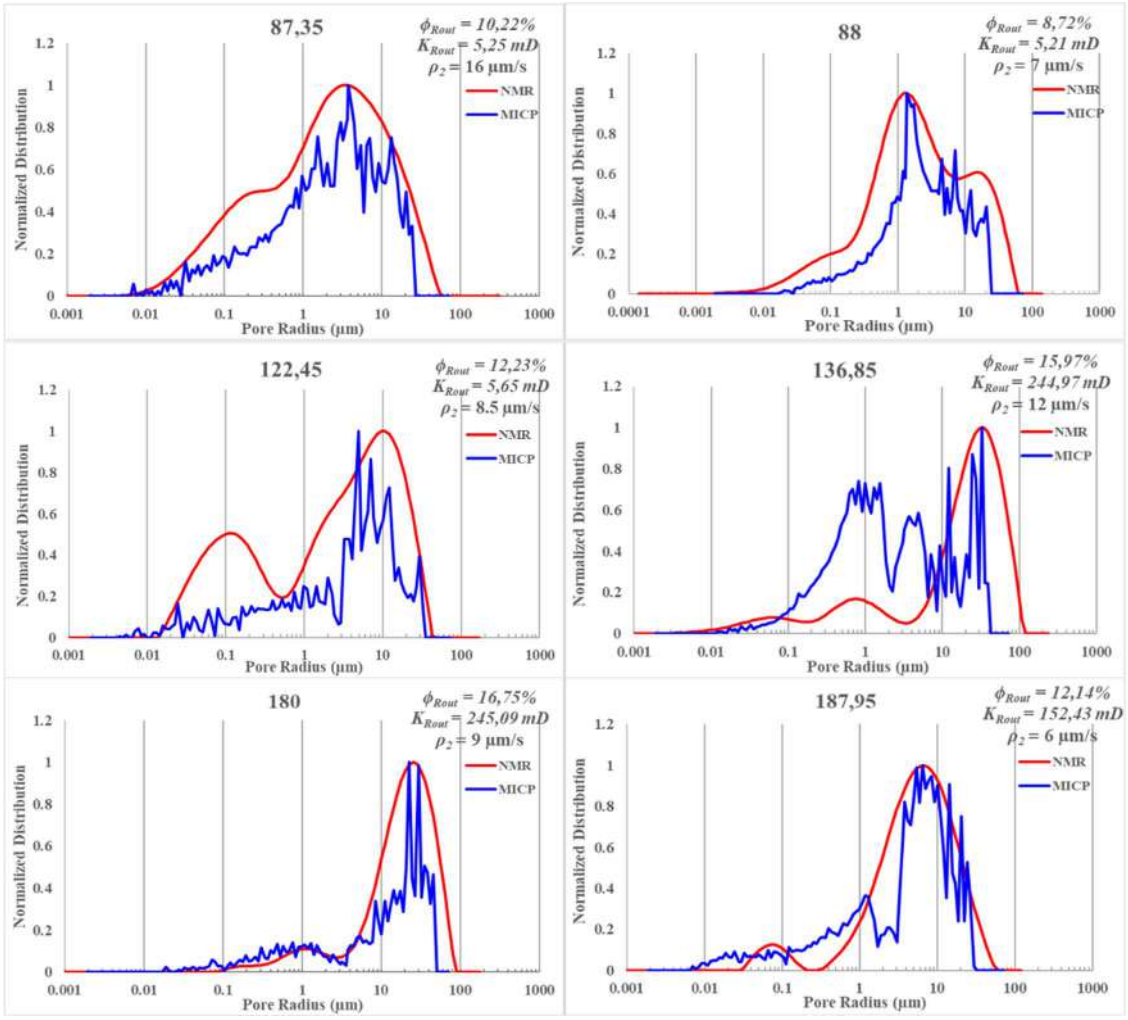

Figure 4-34 – MICP and optimized NMR curves of six carbonate rock samples

Sample 136.85 showed important differences between the two curves. The NMR curve exhibited a triple porosity system, with the larger pores dominating. A somewhat similar shape was obtained with MICP, but with far more smaller pores in the micro/meso hybrid region. Knowing that MICP is more sensitive to throats, and NMR to the entire porous space, this result reflects the limitations of mercury techniques in determining the actual diameters of large pores, when preceded by small pores. During mercury intrusion, pressure increments are required to access the smaller pores. During injection at a given pressure, mercury can enter connected larger pores only after entering the smaller pores that blocked the larger pores. When the acquisition data are processed, the pore volume intruded by mercury is actually measured at a given pressure. The assumption is then made that all pores making up that volume have the same size. In this way, the larger

pores end up being transformed into countless smaller pores with the same diameter, thus increasing their percentage. This effect may explain the significant increase in pores in the micro/meso region shown by the MICP curve. This complexity shown by sample 136.85 is a common feature of carbonate rocks.

Sample 122.45 is also interesting in that the NMR curve shows a higher percentage of pores in the micropore and mesopore regions as compared to the throats of the MICP curve. Pores of this sample hence must be connected by wider throats compared to samples 87.35 and 88, but still have the same permeability. This comparison suggests that the reduction in connectivity contributed to the reduced porosity. Samples 122.45 and 87.35 have the same permeability values (about 5 mD), with most pore throats in the mesoporous region.

As for samples 180 and 187.95, they have similar curves. The MICP and NMR curves show that most pores are concentrated in the hybrid meso/macro region, which explains their relatively permeability values. Figure 4.34 also contains information on surface relaxivity, ranging from 6 to 16 μm/s, typical values of carbonate rocks.

From the ρ_2 values, microCT images were generated to study the pore space connectivity. With the 3D images, the internal structures of the samples could be visualized, such as the orientation of shells, the mineral arrangement, as well as the distribution of pores at the specific resolution being used. The main results obtained by using this technique are analyzed next.

4.3.3 Pore network modeling

This section presents results obtained using X-ray microtomography and pore network modeling of samples 87.35, 88, 122.45, 136.85, 180 and 187.95 discussed in the previous section (Fig. 4.34). Processing and interpretation of data from the reconstructed images was performed using the software Avizo® 9.5.

Porosities were determined from the entire sample volume. As a tool to aid visual segmentation, the NMR comparative method was used (HOERLLE *et al*., 2018), based on the idea that the pore space of an image can be identified from the NMR-measured data. This method allows pores to be identified at the specific resolution that was used. Segmentation of the images was based on the separation of the mineral framework from the pore system and transforming from grayscale into binary image. Initially, pores were

selected visually by characterizing tones closest to 0 in the gray-tone histogram as pores. Figure 4.35 shows the microCT scan of sample 88.

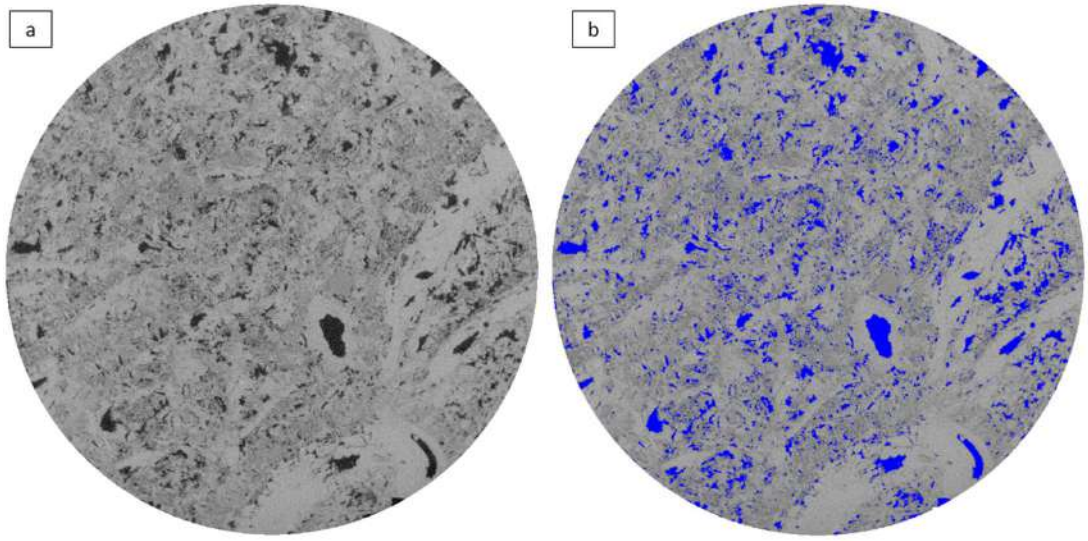

Figure 4-35 – MicroCT slice of sample 88 with a pixel size of 14 µm (pore radius 7 µm): a) Gray scale image, with pores in black and gray being the rocky framework; b) Gray scale images with segmented pores (blue)

This separation of the two populations in the medium in terms of black and gray make it is possible to distinguish pores of solid materials present in a given sample. This separation is a method based on the choice of threshold obtained from the grayscale distribution histogram from the obtained images.

The final determination of the threshold between the rock framework and the pores is then obtained by summing the incremental porosities provided by NMR, based on the percentage relative to the radius of the smallest pore visible at the invoked resolution (e.g. 7 µm). This methodology allows porosity values to be estimated from the images based on the calibration of porosities from the pore radii obtained through integration of the RMN and MICP data. Fig. 4.36 shows a plot of the pore-size distribution of sample 136.85, with the blue area under the curve representing the unresolved porosity from the microCT image.

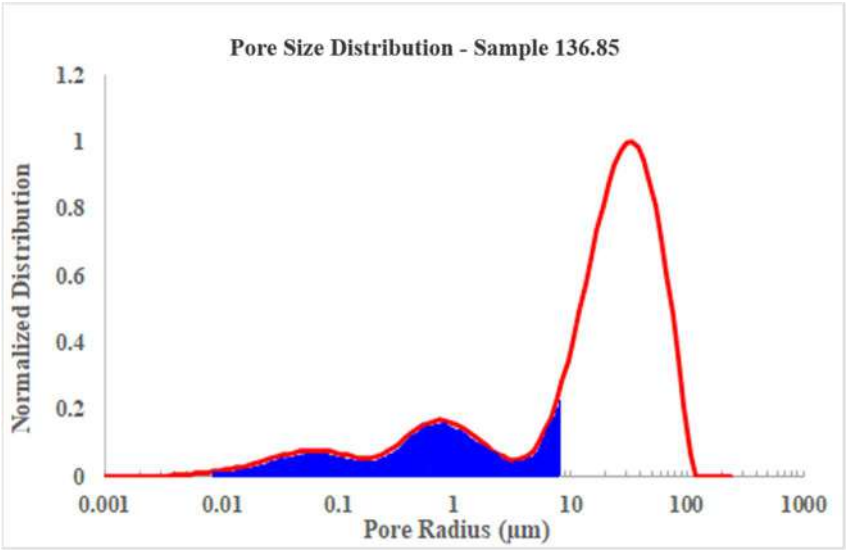

Figure 4-36 – a) Plot showing the pore size distribution of sample 136.85.The blue area under the curve shows unresolved porosity from the microCT images

After segmentation of the pores, data must be prepared for pore network modeling step. Still using the Avizo® 9.5 software, the connected components tool was used to select the cluster of pores connected within a sample. This would create an image with only the clusters, while removing all isolated pores. The autoskeleton tool was used next to transform the pore throats in this new image into cylindrical tubes (by forming in effect a sequence of connected spheres) and the pore bodies into equivalent spheres, a process known as skeletonization (PUDNEY, 1998). Fig. 4.37 summarizes this data extraction process for modeling at the pore scale.

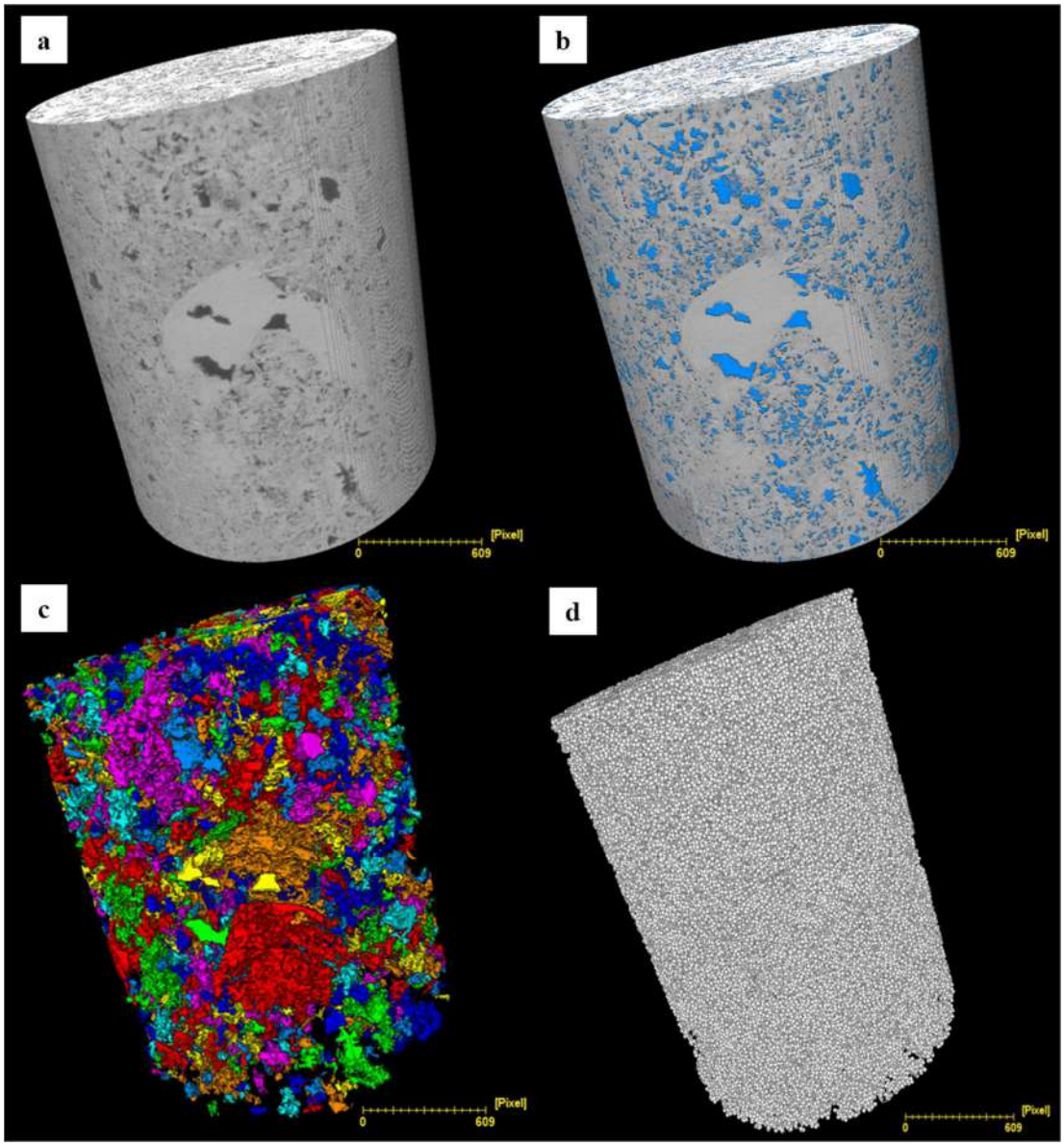

Figure 4-37 – MicroCT images of sample 88 showing the data extraction process for modeling at the pore level: a) cylinder with pores in darker gray tones; b) cylinder with segmented pores (blue); c) cylinder with connected pores of the sample, with different colors demonstrating different connected systems; d) skeletonized connected pores that transform the pore throats into cylindrical tubes and the pore bodies into spheres using the autoskeleton tool

The skeletonization process leads to a series of nodal points and nodes composing the segments. These data subsequently are analyzed and transformed into input data for the porosity and permeability calculations using the PoreFlow software (RAOOF *et al*., 2013). The results obtained through the PoreFlow software showed good correlations when compared with routine core analysis, as shown by the data in Table 4.8. The porosities obtained with PoreFlow were always lower than those obtained by routine petrophysics, but the calculated permeabilities and measurements were very similar for

most samples. One may therefore conclude that the resolution used for imaging the samples was effective in that the pore system responsible for flow within the samples could be identified.

Table 4-8 – Comparison of routine core analysis and Poreflow modeling results

Samples Core depth (m)	$\phi_{routine}$ **(%)**	$\phi_{PoreFlow}$ **(%)**	$K_{routine}$ **(mD)**	$K_{PoreFlow}$ ***(mD)***
87.35	10.2	8.1	4.6	4.6
88	8.7	6.1	5.2	4.4
122.45	12.3	4.2	5.7	3.7
136.85	16.7	13.2	245	249.2
180	16.7	10.8	245.1	236.7
187.95	12.2	6.8	152.4	138.9

Figure 4.38 shows the correlation between the routine permeability measurements and those obtained through simulation. Good agreement was achieved between the permeability predictions obtained with the PoreFlow software and the routine petrophysical measurements. Table 4.8 shows that samples 122.45 and 187.95 had the same porosity (12%), but different permeability values (5.65 mD and 152.40 mD, respectively). One major advantage of using microCT images is the possibility to further investigate the internal structure of a sample. Modeling with PoreFlow then enables one to estimate in a non-destructive way the connected pore system by identifying the pore bodies and pore throats that contribute to storage and fluid flow within the system. Thus, the study of connectivity becomes very effective when performed through microtomography and pore network modeling.

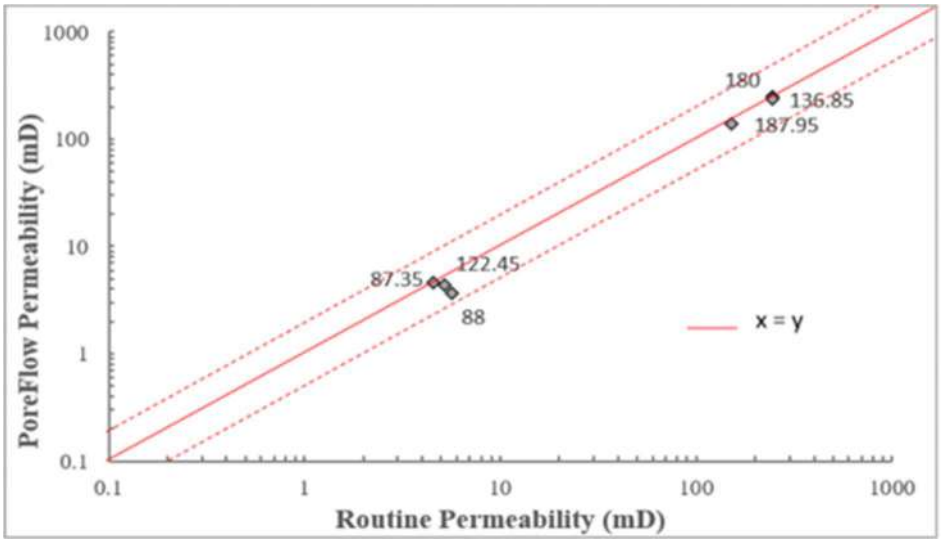

Figure 4-38 – Plot showing good correlation between the routine permeability of six samples, and permeability obtained using pore network modeling

Because of the close agreement between the routine petrophysical measurements and the pore network modeling results as shown in Fig. 4.38, a more detailed analysis of the PoreFlow output data of samples 122.45 and 187.95 was carried out. Main objective was to better understand how the connectivity of the pore systems would lead to the differences in permeability. Using the Paraview software (AYACHIT, 2015), the pore system of the samples was visualized to identifying the pore bodies and throats that are most connective with the pore system. This would quantify the connected pore groups, in addition to allowing visualization of the main cluster connecting the base and the top of the samples. The resulting percolation route would be most responsible for flow in the system.

Figure 4.39 shows the images of sample 122.45 and 187.95 as obtained using Paraview. The images show the pore arrangement, the connected pore groupings, and the main group responsible for the permeability in the samples. Figure 4.39a shows the pores of sample 122.45, with the smaller pores in blue and the larger pores in red. In Fig 4.39b, the clusters of connected pores are visualized, showing different colors for each connected group, with a total of 1748 recognized pore groups being quantified. Fig. 4.39c further shows the main pore grouping responsible for flow. Since pore network modeling produced a very similar value of the permeability as the routine petrophysical experiments, one may conclude that the cluster shown in Fig. 4.39c is mostly responsible for the conductivity of fluids within the pore system. Fig. 4.39d shows the pores of sample of 187.95, with the size of the cylindrical pores again differentiated by color. In Fig. 4.39e, all pore clusters in the sample are visualized; a total of 724 distinct groups were

recognized (i.e., those that were separate from each other), forming the most connected pore network in the sample. Figure 4.39f shows the main pore cluster of sample 187.95 responsible for fluid flow within the system.

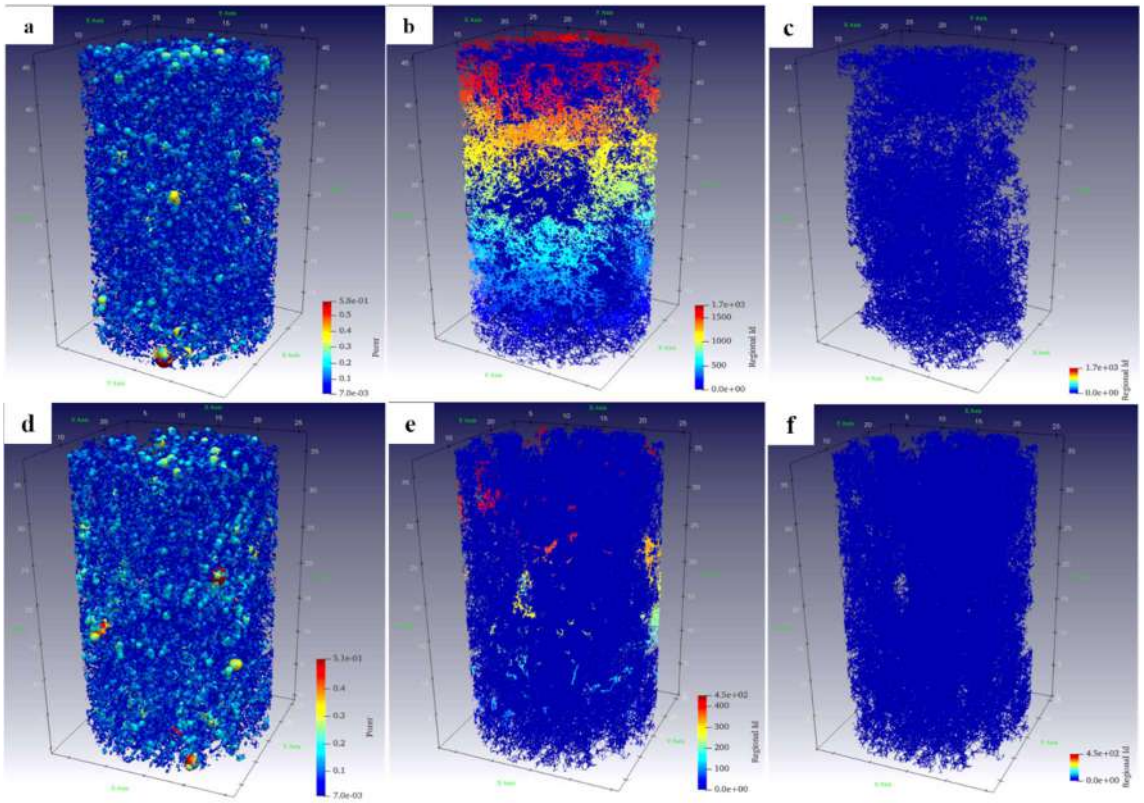

Figure 4-39 – Pore system distribution of two rock samples: a) all pores connected in sample 122.45: red spheres (e.g., the bottom) correspond to the biggest pores in the sample; b) all pore clusters of sample 122.45, with each cluster corresponding to a different color (the scale bar identifies the clusters); c) the main pore cluster responsible for flow through the sample and its permeability; d) all pores connected in sample 187.95; e) all pore clusters of same sample 187.95; and f) the main pore cluster. This figure explains why sample 187.95 with a similar porosity as sample 122.45 has a much higher permeability. Scal bar in mm

The compositional differences of connected pores in the pore groups responsible for most of the percolation (Figs. 4.39c and 4.39f) reflect the distinct volumes of connected pores of the two samples, and explain the differences in permeability: sample 122.45 contained a main cluster with fewer connected pores and, consequently, a lower permeability, while sample 187.95 had a much larger volume of connected pores belonging to the main cluster, thus leading to a higher permeability. The large amount of non-percolating agglomerates in sample 122.45 (Fig. 4.39b) is responsible for the difference between the NMR and MICP curves of samples 122.45 and 187.95, as shown in Fig. 4.35. While NMR captures the entire pore system, MICP measurements are mostly

affected by the presence of clusters of complex non-percolating pores; this since MICP is based on the flow of mercury into the sample. Similar correlations for other images were found to be useful in explaining why certain samples with similar total porosity gave different permeability values. As explained well by LUCIA (1999), diagenesis normally reduces porosity, redistributes pore space, and changes permeability and the capillary characteristics. The changes caused by this effect may have affected most or all of the permeability changes by increasing the complexity of the pores of the samples.

To obtain a more complete understanding of connectivity and its impact on permeability, some statistical analyses were carried out with the data obtained from the images of the two samples. Initially, the coordination numbers were analyzed. These numbers, also called pore connectivity, represent the average number of pore bodies that are connected to adjacent pores (SAHIMI *et al*., 2012). They are a fundamental characteristic of pore networks and have a real impact on the hydraulic conductance calculations of porous rocks (CHEN *et al*., 2003; VASILYEV *et al*., 2012).

Frequency histograms were created to compare the distribution of the coordination numbers of samples 122.45 and 187.95. The results in Fig. 4.40 show that sample 187.95 has far more connections (counts) between the pore bodies, especially those with coordination number 3. This implies that RT3 sample 187.95 has much better pore interconnections, and hence a higher permeability, than RT1 sample 122.45, even if they were to have similar throat radii.

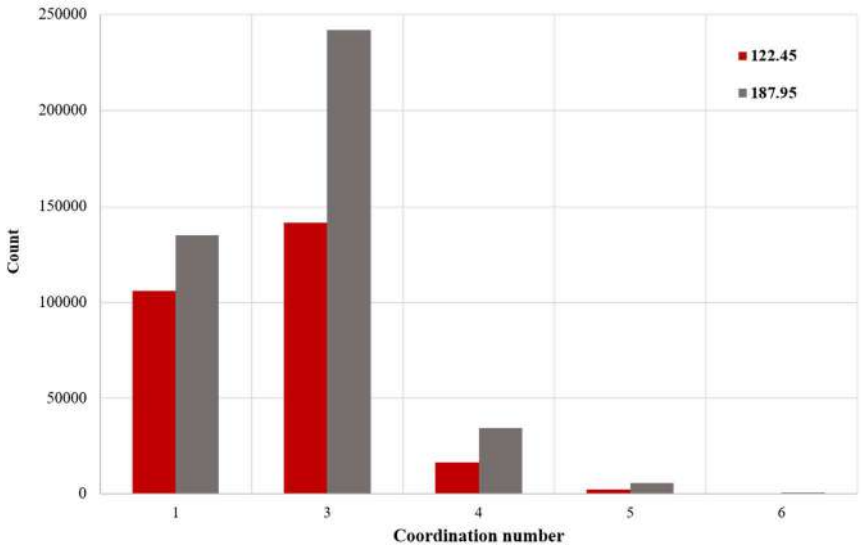

Figure 4-40 – Comparison of the distribution of coordination numbers for samples 122.45 and 187.95

An alternative way to explain the differences in permeability between samples is an analysis of their pore bodies and throats. Using the information extracted from the skeletonized images, one can quantify the volume and size of the pore bodies and pore throats. These two parameters in their entirety, should reflect the complexity of the pore system of a sample. Such an analysis was applied to samples 122.45 and 187.95.

Figure 4.41 presents the distribution of pore bodies (Fig. 4.41a) and pore throats (Fig. 4.41c) of samples 122.45 and 187.95. The plots show that sample 187.95 (gray lines) has higher volumes of both pore bodies and pore throats, which is consistent with its higher permeability as compared with sample 122.45 (red lines). The pore sizes obtained from the skeletonized images are larger than those estimated from the NMR and MICP data. Comparing these techniques assumes equivalence of the pore bodies and pore throats sizes, which may not be appropriate for carbonate rocks, which can be very heterogeneous. Still, using this conversion, the permeabilities estimated from the images agreed well with the direct measurements, thus confirming the applicability of the proposed workflow in section 1.3. Figs. 4.41b and 4.41d show the differences in the accumulated porosity of both the pore bodies and pore throats of samples 122.45 and 187.95. Sample 187.95 displayed a considerable difference in the accumulated volumes when compared to the elements of sample 122.45, a finding that helps to understand the difference in permeability between them.

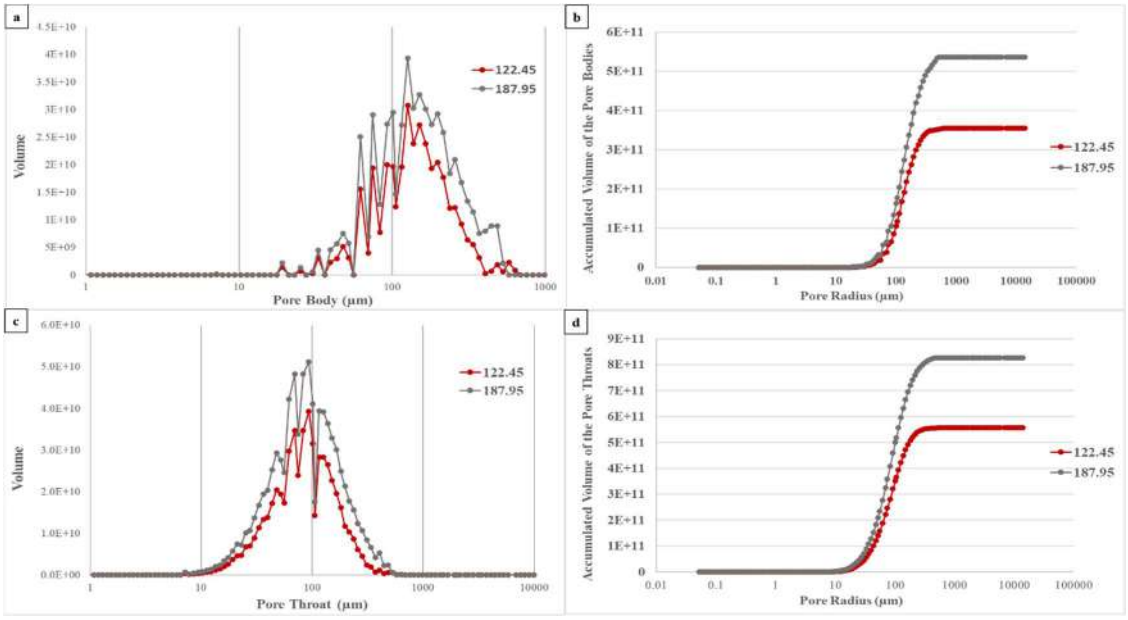

Figure 4-41 – Plots comparing the pore structure of samples 122.45 and 187.95 in terms of a) actual pore body volumes; b) cumulative pore body volumes, c) actual pore throat volumes, and d) cumulative pore throat volumes.

Fig. 4.41b also shows that the microCT estimates of the pore throats are higher than those determined using MICP. As mentioned earlier, the MICP results are based on the Washburn equation, which approximates the porous medium as a bundle of cylindrical tubes. When analyzing carbonate rocks (especially coquinas), the heterogeneity of the pore systems in terms of different pore formats must be taken into account. These differences are exemplified in Fig. 4.42 using the microCT slices of samples 122.45 and 187.97. The figure illustrates the differences between the pore systems of these two samples. Although the images are in two dimensions (microCT XY slices), it is possible to recognize that the moldic pores (e.g., arrow a) and interparticle pores (arrow b) of sample 122.45 differ greatly from the vug pores (arrow c) of sample 187.95. However, due to the resolution used, it was not possible to detect other differences in and between the samples, which would require a better resolution for this study.

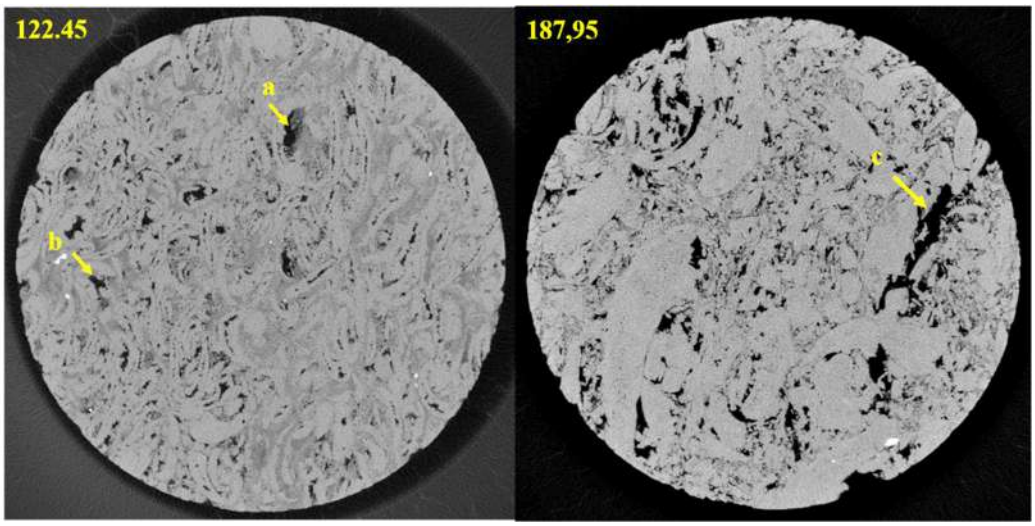

Figure 4-42 - 2D microCT slices highlighting different pore types for samples 122.45 (left) with moldic (arrow a) and interparticle (arrow b) pores, and sample 187.95 (right) with many intraparticle vugular pores (arrow c)

Some aspects are known to impact studies using NMR. One concerns uncertainties in the measurements of the surface relaxivity (ρ_2). Since ρ_2 does not have an exact form to be calculated, being mostly approximated by means of different equations, this parameter may cause errors when converting relaxation times into pore radii. Another factor that also influences NMR results is the bulk effect of the larger pores. Above 2.5 s (the relaxation time of a sample saturated with fluid), the spins do not completely collide with the pore walls within the sample, which can make the measured relaxation time less reliable (KENYON, 1997). This in turn causes uncertainty in the size of pores, especially of the larger pores.

4.4 Permeability estimation based on NMR results

As the main focus of this research, the permeability (k) is an essential parameter in petrophysical studies. Accurate estimates of this parameter will improve the design of hydrocarbon production strategies with a view to more efficiently manage reservoirs. One specific objective of this study is the application of classical permeability models to coquinas, a carbonate rock that is present in the Brazilian pre-salt reservoirs. With their complex characteristics, studies of the permeability of coquinas should give insight also about the use of classical permeability models to improve the accuracy of estimates made from well logging data.

This section presents permeability estimates obtained with the main models frequented in the oil industry. After obtaining the necessary parameters for the models described in section 2.3.1, the permeability of the samples was estimated. This section provides an analysis of the measured permeability data in terms of two models, the Kenyon model (k_{Sdr}) and the Timur Coates model (k_{Tim}), both using available NMR results.

4.4.1 Kenyon Model (k_{Sdr})

As mentioned earlier, one of the great virtues of NMR techniques is the possibility of estimating the permeability from well logging data. Accurate permeability data are critical to defining the potential production of an oil and gas reservoir. As discussed in section 2.3.1, one of the most popular models for the permeability is the classical Kenyon model, often referred to as k_{Sdr} after the **S**chlumberger-**D**oll **R**esearch center where the model was developed. As shown by Eq. (2.7) in section 2.3.1, and restated here, the Kenyon model is based on the logarithmic mean ($T_{2Logmean}$) of T_2 distribution data, as well as on the porosity:

$$\boldsymbol{k_{sdr} = c\ \phi^a\, T^b_{2Logmean}} \qquad (4.1)$$

in which, a, b and c are empirical constants. The equation has been widely used in both research and for various field applications. KENYON *et al*. (1988) obtained values of 4, 2 and 4.5 for a, b and c, respectively. The constant $\boldsymbol{c}$ is strongly influenced by the lithology of the rock formation.

Equation (4.1) with the above constants obtained by KENYON *et al*. (1988), was first tested against the routine core permeability measurements obtained in this study. Fig. 4.43 shows the correlation between the predicted (k_{Sdr}) values and the routine core data ($k_{routine}$). Using the classic constants in the Kenyon equation underestimated the true values since the majority of the predicted points are located below the 1:1 line (X = Y).

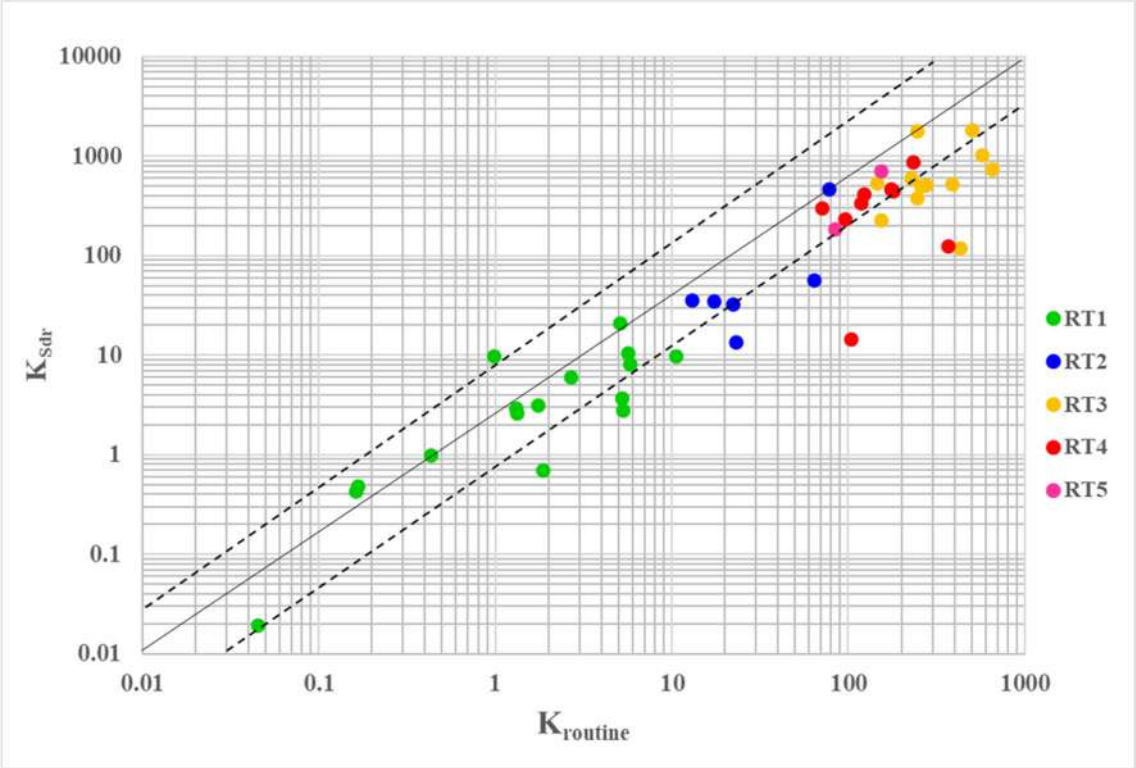

Figure 4-43 – Plot comparing permeabilities from routine core measurements with those predicted with the Kenyon equation using literature values for the parameters in Eq. (4.1). The measures data are shown by rock type.

To improve the permeability estimates, Eq. (4.1) was used again, but now with optimized constants *a*, *b* and c, obtained using multiple linear regression (MLR). The main objective of MLR is to the estimate unknown parameters of a given model from measured data (COELHO-BARROS *et al*., 2008). Application of this technique to the available routine permeability data produced the following optimized values for the parameters in the Kenyon equation: a = 4.88, b = 0.727, and c = 9.51. The optimized value of the constant c (9.51) was found to be considerable larger than the classic literature value (4.5). Carbonate rocks generally have lower surface relaxivity values than sandstone rocks (KENYON, 1997), which should be taken into account. This likely caused an difference in the c value for the coquina samples of this study. The classic

constant hence required some adjustment when the Kenyon equation is applied to coquinas.

The constant *a* for the coquina samples was not much different, showing that the dependence of *k* on porosity is quite stable. However, the constant *b* for our samples (0.727) showed a reduction in value compared to the classic model (2.0). This can be explained by the heterogenous nature of the pore system of many coquinas, which causes the average relaxation times of rocks not to be very representative. Because coquinas often contain large pores (e.g. vugs and moldics), as well as sometimes narrower throats, the pore body to pore throat ratio can be unusually large, thus requiring a reassessment of the impact of the average relaxation time on the permeability. Linear regression caused the exponent *b* to decrease from its classical value of 2.0 to a value of 0.727 for the coquinas, which implies a slightly lower effect of the average relaxation time on the permeability.

Recalculating the permeability with Eq. (4.1) using the optimized parameters improved the comparison between the predicted and measured permeabilities, as shown by the results in Fig. 4.44. Permeability predictions improved for almost all samples. However, some samples did not show satisfactory agreement. The predicted values for some samples overestimated the measured values (such as for RT1 samples 141 and 151.15 and RT5 samples 71.3 and 99.5), while in other cases they underestimated the measurements (such as for RT3 sample 90.95). As demonstrated earlier in section 4.2 when characterizing the various rock types, those five samples differed from the other samples in their groupings, which implies that not necessarily the same values of the constants *a*, *b* and *c* should be used.

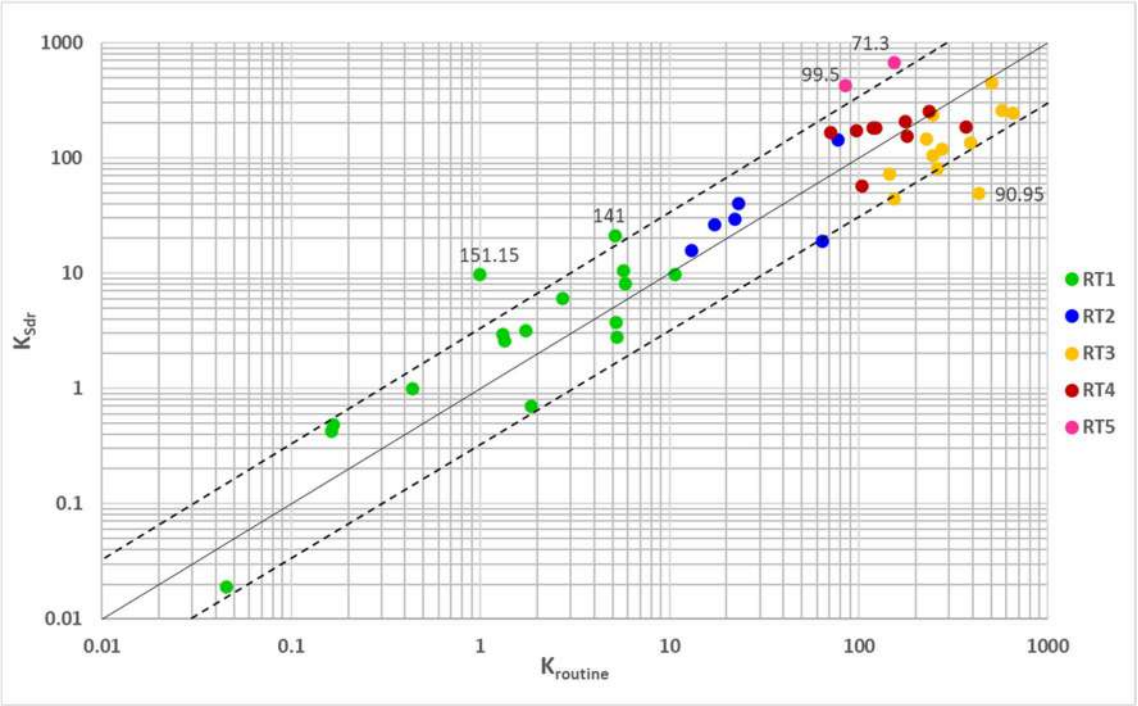

Figure 4-44 – Plot comparing permeabilities from routine core measurements with those predicted with the Kenyon equation (k_{Sdr}) using optimized values of the parameters in Eq. (4.1). Measured data are shown by rock type. Notice that samples 151.15 and 141 of RT1, 90.95 of RT3, and 71.30 and 99.5 of RT5 are situated outside the dashed lines

To further improve the predictions, Eq. (4.1) was applied next to each rock type separately. This would lead to constants that are more customized to the separate samples, mostly in terms of their permeability values. Another advantage of this approach would be to account for the possible effects of the two variables (porosity and $T_{2logmean}$) in Eq. (4.1) on the permeability predictions of the different rock types. Table 4.9 shows the MLR optimized values obtained for the constants, with Fig. 4.45 comparing the measured and newly calculated permeabilities.

Table 4-9 – Multiple linear regression estimates of the parameters a, b and c in Eq. (4.1) for the different rock types.

Rock types	*a*	*b*	*c*
RT1	4.38	0.32	9.53
RT2	2.83	0.90	4.28
RT3	3.82	0.89	16.51
RT4	4.47	0.30	14.55
RT5	2.83	0.90	4.28

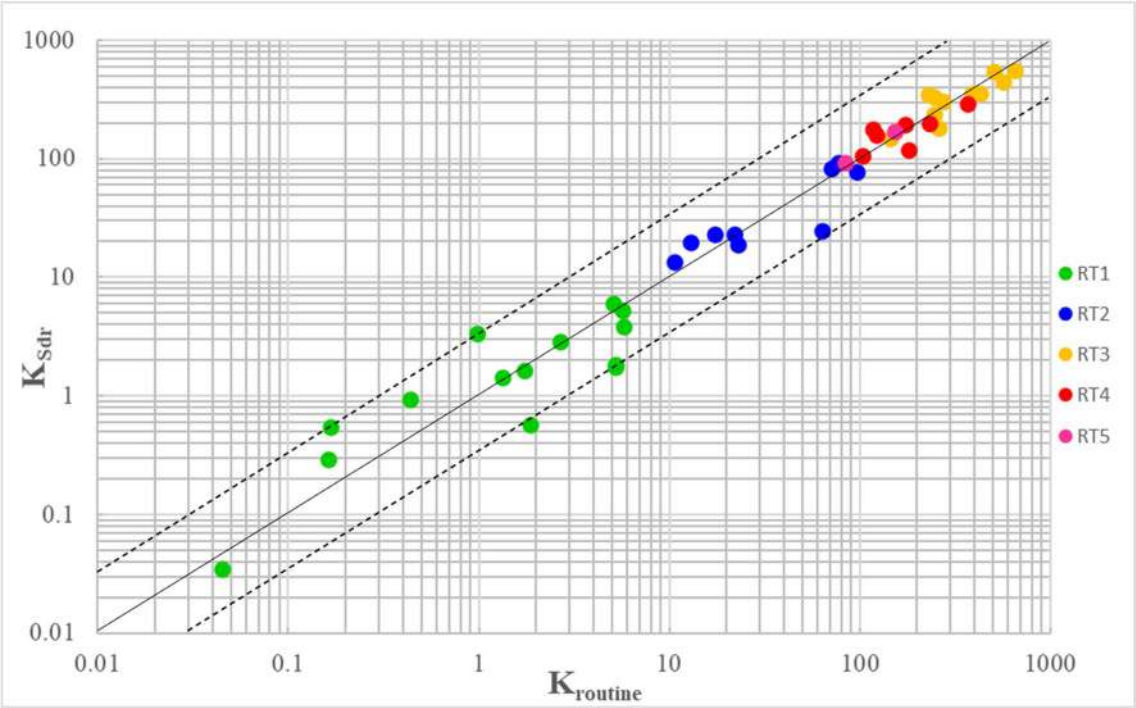

Figure 4-45 – Plot comparing permeabilities from routine core measurements with those predicted with the Kenyon equation (k_{Sdr}) using optimized values of the parameters in Eq. (4.1) for each rock type separately. The MLR optimized values of *a*, *b* and *c* are listed in Table 4.9

The entries in Table 4.9 show that the constants *a*, *b* and *c* deviated from the classical values, as well as varied markedly among themselves. The constant *b* remained relatively low, presumably because of carbonate rock heterogeneity as noted earlier. The lithological constant *c*, however, varied widely, with much higher values for the RT3 and RT4 rock types. Since they are clusters formed by samples with the highest permeability and as noted earlier, predominated by vug pores, the lower values of *b* and the considerable increase in *c* appear to mathematically compensate each other. The low contribution of $T_{2Logmean}$, due to heterogeneity of the porous medium, may be offset by the increase in *c*, a realistic finding for the coquinas tested in this research. Still, this result should be tested on other samples, including on well logging data with know lithology.

Figure 4.45 indicates close correlation between the calculated and measured permeabilities. According to BROOKS & BARCIKOWSKI (2012), using a very small number of samples to validate regression models can cause statistical errors. PEDHAZUR & SCHMELKIN (2013) recommended that equations determined using multiple linear regression should only be considered representative of a data set when the ratio of data size and number of variables is at least 30:1, with MILLER & KUNCE (1973) earlier suggesting a ratio of 10:1. The values obtained for the constants *a*, *b* and *c* in this study

are considered quite promising since the increasing and decreasing trends in the MLR estimated values of the constants were very consistent.

The regression could not be applied to RT5 since this rock type contained only two samples. Because of this, the constants of the other clusters were tested to see if they could be applied to RT5 samples. The results for the RT2 cluster successfully estimated the permeability of the two RT5 samples. Characterization of RT2 and RT5 rock types earlier demonstrated that they showed similarities only in their petrophysical parameters (porosity and permeability), but not in many petrographic properties. RT2 was classified as a transition group, while RT5, grouped samples that were in the high permeability range, with porosities above those of the RT3 and RT4 groups. For these reasons we conclude that the two rock types can be considered to be transitional groups by containing samples that did not fit into the other clusters, while being similar in terms of their heterogeneity. The lithological constant *c* of RT5 was not modified much, being similar to the value used for sandstone rocks. The exponents *a* and *b* (for porosity and $T_{2Logmean}$) decreased only slightly from the original Kenyon values, thus reinforcing the low representativeness of these two parameters for predicting the permeability, *k*.

The above results for the Kenyon model us indicate that permeability predictions using the classical values of the Kenyon constants *a*, *b* and *c* produced relatively poor results. Some improvements were possible when adjusting the constants for all of the samples used in this study. MLR optimization of the constants for each rock type separately further improved the predictions such that all estimated permeability values closely approached the measured values. Using only the measured porosity and measured pore size distribution did not lead to acceptable results for several of the samples. One may conclude that in addition to connectivity, other factors such as the mean pore throats radii and throat constrictions need to be better evaluated since they can have a great impact on fluid flow and better explain observed permeabilities, especially of carbonate rocks.

4.4.2 Timur-Coates Model (K_{Tim})

Permeabilities of the various samples in this thesis were also analyzed in terms the Timur-Coates model (k_{Tim}), given by Eq. (2.12) of section 2.5.1 and restated here:

$$\boldsymbol{k_{Tim} = c \left(\frac{\phi}{100}\right)^{a} \left(\frac{FFI}{BVI}\right)^{b}} \qquad (4.2)$$

where ϕ is porosity as before, *FFI* is the free fluid index, *BFI* is the bulk fluid index, the latter representing fluid adsorbed by clay minerals and trapped by capillarity, and *a*, *b* and *c* are empirical constants, with c again being a mostly lithological parameter. Values of the constants most commonly used in the oil industry are those for sandstone: $a = 4$, $b = 2$, and $c = 100$. The biggest difference between the Kenyon and Timur-Coats equations is the change of the $T_{2Logmean}$ parameter for the ratio *FFI*/*BFI*, which aims to improve predictions by using $T_{2cutoff}$, a separation factor between immobile fluid (*BFI*) trapped by capillarity and in clay minerals, and free fluid (*FFI*), which has a mobility and can be produced. This ratio is usually evaluated at some relaxation time between 90 and 100 ms, being the threshold of the mesoporosity region (in this study 100 ms is used).

In the same way as for the Kenyon model, initially literature values of the constants *a*, *b* and *c* were used to evaluate their ability of Eq. (4.1) to predict the measured permeabilities (*k*) of the coquinas. The plot of measured (k_{rot}) versus predicted (k_{Tim}) in Fig. 4.46 shows that the use of classical values did not lead to accurate permeability estimates, with the predicted values being dispersed in the figure. About 30% of the samples were outside of the considered error ranges, which suggests that the $T_{2cutoff}$ values and/or the constants needed to be reevaluated.

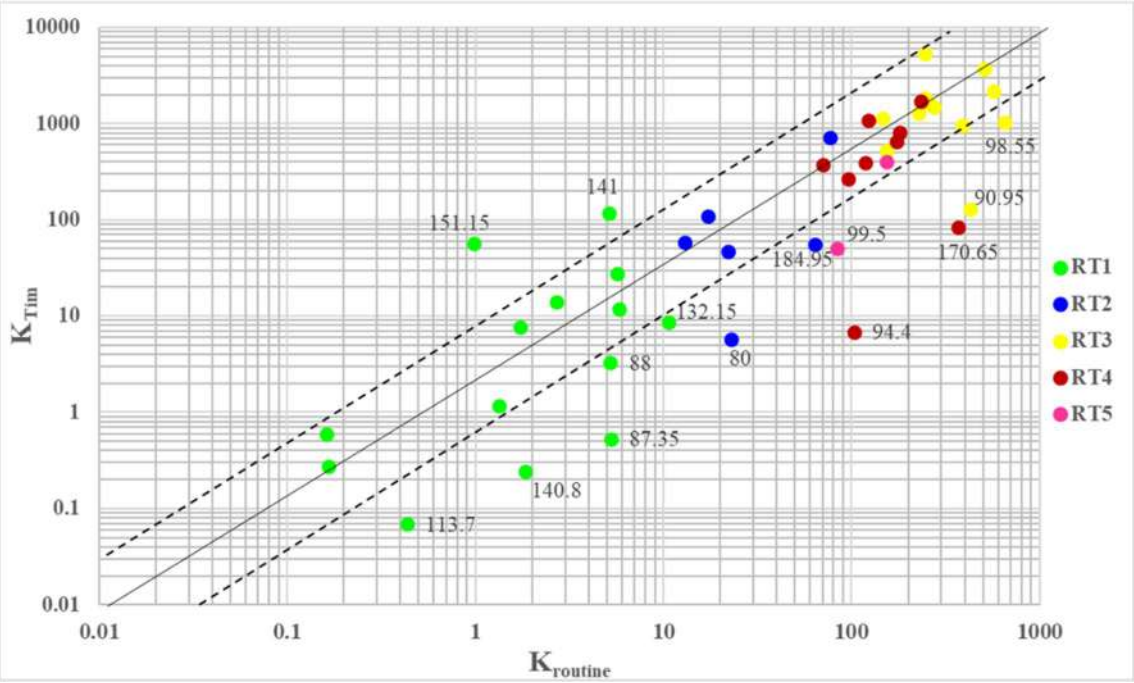

Figure 4-46 – Plot comparing permeabilities from routine core measurements with those predicted with the Timur-Coates equation using literature values for the parameters *a*, *b* and *c* in Eq. (4.2). The measurements were separated by rock type

The RT1 samples in Fig. 4.46 were the most poorly predicted, probably because a high value of $T_{2cutoff}$ was used for samples having relatively small pore sizes compared to the other groups. To verify if the *FFI*/*BFI* ratios were correct, it is necessary to determine the irreducible saturation of the samples, which can be carried out either by centrifugation or using porous plates. Initially, some samples considered to be representative for each rock type were taken to define S_{wi} for subsequent evaluation of $T_{2cutoff}$. Unfortunately, the use of only a few samples was not sufficient to more accurately evaluate this parameter, thus we fixed the cutoff at 100 ms and used multiple linear regression (MLR) to determine the constants for the samples.

A first attempt was made to optimize the constants for all of the samples combined, leading to Fig. 4.47. The MLR analysis produced the values $a = 4.02$, $b = 1.13$ and $c = 409$. Note that the optimized values of these constants showed similarities with those determined for the Kenyon equation. Again, the lithological constant varied the most, thus reinforcing the premise that the response is associated with a change in the surface relaxivity of the samples. The constant *a* linked to porosity did not change much this parameter showing more stability between permeability and porosity as was the case for the Kenyon model. The constant *b* was lower than classic value, which can be justified by the inappropriate value of $T_{2cutoff}$, which is difficult to determine for rocks as heterogeneous as the coquinas.

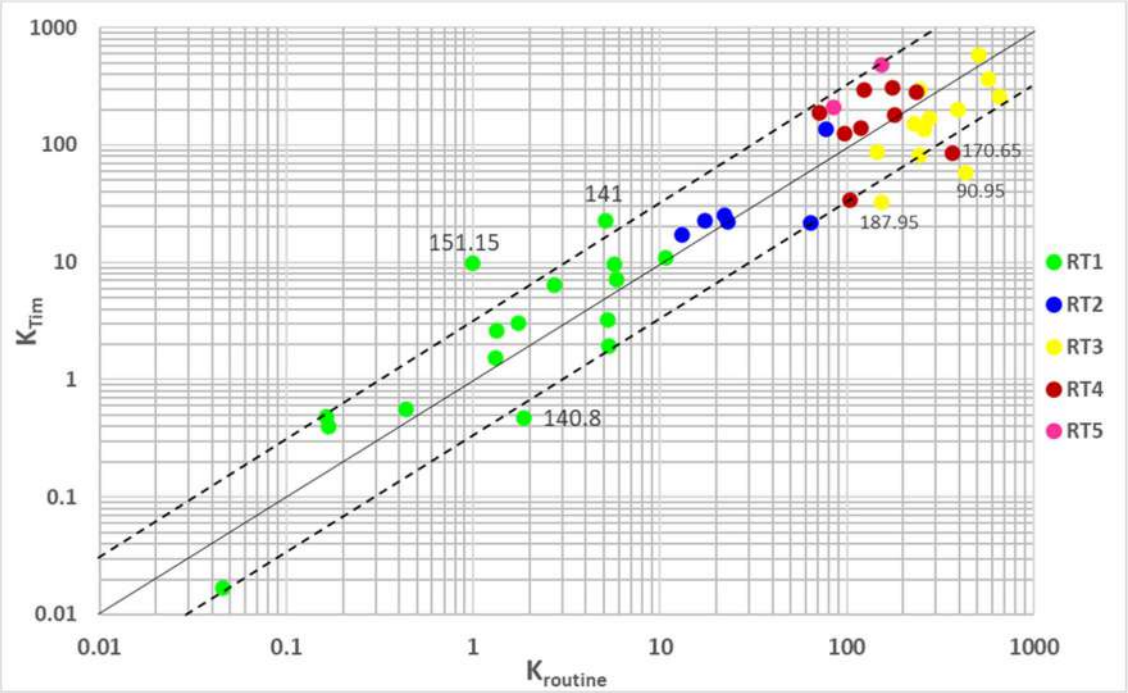

Figure 4-47 – Plot comparing permeabilities from routine core measurements with those predicted with the Timur-Coates equation (k_{Tim}) using optimized values of the parameters in Eq. (4.2). Measured data are shown by rock type. Notice that samples 140.8, 141 and 151.15 (RT1), 90.95 and 187.95 (RT3) and 170.65 (RT4) are situated outside the dashed lines

Figure 4.47 shows that MLR optimization of the constants *a*, *b* and *c* in Eq. (4.2) did lead to a better prediction of the measured permeabilities. Success was achieved for about 90% of the samples, reflecting a better correlation between the estimated and measured values. However, some samples still did not present satisfactory values, involving underestimated values for samples 140.8 (RT1), 90.95 and 187.95 (RT3) and 170.65 (RT4) and overestimated values in the cases of samples 141 and 151.15 (RT1). These samples, with the exception of 187.95, showed differences with the other samples of their rock type groupings, as noted earlier for the Kenyon analysis in section 4.4.1.

Improved correlations were again possible by applying the MLR analysis separately to each rock type, with the additional advantage that the effects of the porosity and the *FFI*/*BFI* ratio on the permeability became more clearly defined. Table 4.10 shows the different values obtained for the constants, while Fig. 4.48 compares the estimated permeabilities with the measured values.

Table 4-10 – Multiple linear regression estimates of the parameters *a*, *b* and *c* in Eq. (4.2) for the different rock types

Rock types	*a*	*b*	*c*
RT1	3.84	0.56	1712
RT2	2.12	0.95	999
RT3	2.98	0.22	11592
RT4	6.62	0.22	94567
RT5	2.12	0.95	999

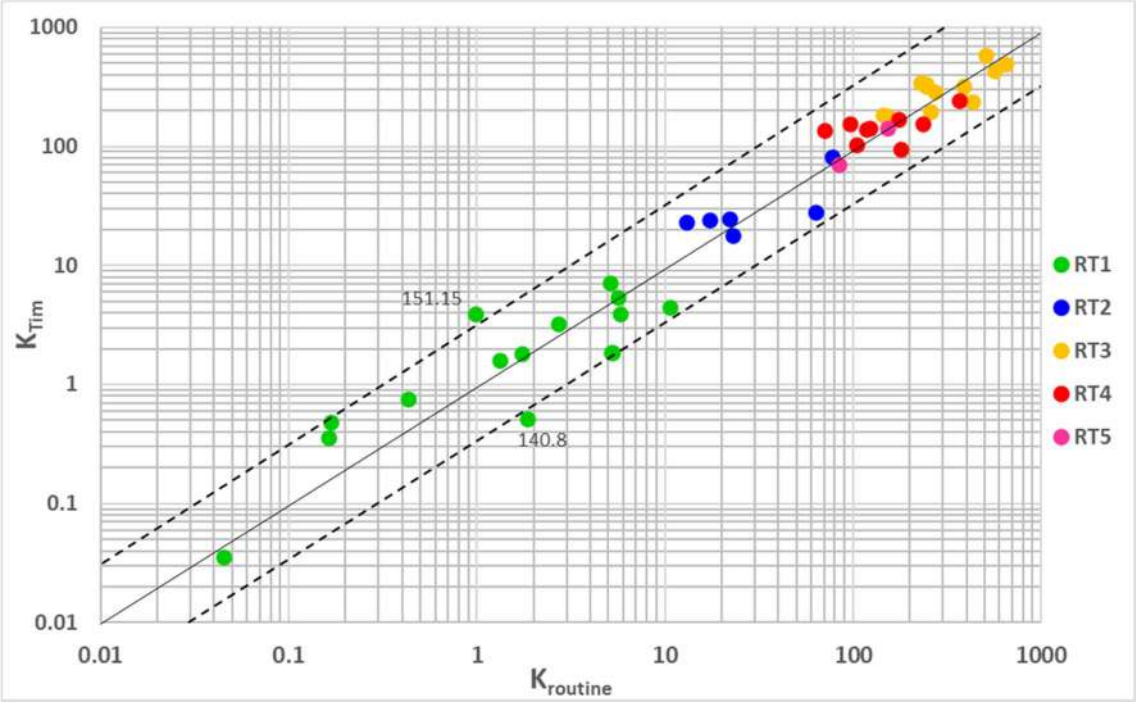

Figure 4-48 – Plot comparing permeabilities from routine core measurements with those predicted with the Timur-Coates equation (k_{Tim}) using optimized values of the parameters in Eq. (4.1) for each rock type separately. The MLR optimized values of *a*, *b* and *c* are listed in Table 4.10

The data in Table 4.10 show some interesting differences with the classical values of the constants *a*, *b* and *c* in Eq. (4.2). The value of the lithological constant *c* increased for all rock types, possibly related to differences in the surface relaxivity of the samples. The RT3 and RT4 samples exhibited higher values of *c*, probably because of their higher permeability, which compensated for the low value of the constant *b* associated with pore size. The $T_{2cutoff}$ value used for these groupings may have required better adjustment, which should be explored in future studies. The porosity constant *a* showed only slight

variations, mostly since this porosity terms does not affect *k* predictions as much as the NMR contribution. The constant *b* was lower that the classical value of 2, similarly as in the Kenyon model. Because this parameter is directly associated with the pore size distribution, the considerable heterogeneity of the coquina samples forces the parameters *c* to increase to mathematically compensate for the relatively lower contribution of the *FFI*/*BFI* term. While the MLR generated values of the constants *a*, *b* and *c* improved the permeability predictions, it is important to emphasize that the generality of the results here should be tested on other samples, including on well logging data of this lithology.

As mentioned previously, the RT5 samples could not be used for the MLR optimization because of the low number of samples of this rock type (only samples 71.3 and 99.5). The RT2 constants were used again successfully for predicting the permeability of these two samples. Similarly as before, the two clusters can be considered transitional since they did not fit in any of the other clusters. The analyzed samples showed an increase in the value of the lithological constant *c* and a reduction in the porosity constant *a*. Exponent *b* of the *FFI*/*BFI* term showed a decrease in its value, which may be associated with the poor representativeness of this parameter in the permeability predictions, and/or the need to improve the $T_{2cutoff}$ value.

Figure 4.48 still shows two samples that were not completely resolved by the optimized constants. Unlike with the Kenyon model, the use of the *FFI*/*BFI* ratio for these samples did not benefit the predictions. Thus, *k* predictions for these two complex samples could benefit from a more detailed careful analysis of both the pore throats and pore bodies as inevitably the connectivity of pore system has the major effect on the permeability. From the permeability predictions above, one may conclude that the classical constants in the Timur-Coates model provided less accurate results by showing a far more dispersed range of *k* values. Improvements could be obtained by optimizing the parameters, either by using all available samples together, or analyzing them separately according to rock type.

The Kenyon and Timur-Coates were compared further by comparing the constants determined by the regressions. Two correlation parameters were used: the coefficient of multiple determination (R^2) and the multiple R (R). From the R^2 it is possible to identify how well a multiple regression equation fits the sample data, with its values ranging from 0 to 1, where 1 represents a perfect correlation with no differences between the real and estimated values. R^2 is widely used in dispersion plots, such as for the porosity and permeability in petrophysics, but its value can be affected by the number of variables

being used (DAVIES & FEARN, 2006). Using only this parameter can generate for this reason doubtful results, making it necessary to use one more comparative parameter, in this case the multiple R. This parameter demonstrates the degree of linear correlation between the dependent variable and the set of independent variables. Specifically, R measures how closely they are correlated, with the highest value being the best model.

Table 4.11 lists the values of R^2 and R for both the Kenyon and Timur-Coates models. The data in this table allow comparisons of the two models, with optimized values of *a*, *b* and *c* in their respective formulations, as applied to the whole set of samples and separated by rock type. The Kenyon model applied to the entire set of samples produced very acceptable values of R^2 and R (0.79 and 0.89, respectively). When the results were plotted on a comparative plot (Fig. 4.44), only five samples fell outside of the permeability trend ranges. When the samples were separated by rock type, the correlation parameters were also quite satisfactory, with the correlations providing permeability values within the trend ranges (Fig. 4.45). Both options (with and without separating the rock types) hence showed good correlations, validating the use of both.

Table 4-11 – Correlation parameters from the regression

	Kenyon Model		***Timur - Coates Model***	
Samples	***R²***	***Multiple R***	***R²***	***Multiple R***
All samples	0.78	0.89	0.88	0.94
RT1	0.76	0.87	0.74	0.86
RT2	0.77	0.88	0.54	0.74
RT3	0.79	0.89	0.59	0.77
RT4	0.58	0.76	0.29	0.54
RT5	0.68	0.87	0.54	0.74

Regarding the correlative parameters of the Timur-Coates model, they showed also better results when the entire set of samples is used, compared to when the statistical analysis is carried out for each rock type separately. With an $R^2 = 0.87$ and a multiple R = 0.94, the Timur-Coates was superior when using all samples simultaneously, notwithstanding more samples being outside of the permeability trend lines (Fig 4.47). The correlation results were less when the constants were optimized separately for each rock type, especially for RT4 with a value of 0.29 for R^2. For this cluster, all constants

varied greatly as compared to using the classic values of *a*, *b* and *c*. This may be a sign that not only porosity and *FFI*/*BFI* contribute to permeability, but other factors may need to be considered and possibly should be incorporated also in the predicted permeability equations. As pointed out previously, the constants determined in this research are well suited for the samples studied here, but their effectiveness still needs to be evaluated with more samples.

5 CONCLUSIONS

Through the application of different petrophysical techniques, this research aimed to obtain a more complete understanding of carbonate rocks samples contained in core 02-SMC-2-AL of the Morro do Chaves Formation. These rocks are a challenge due to the high compositional complexity and heterogeneity of the pore space, their understanding being of great importance for the challenging oil scenario of the Brazilian pre-salt.

Rock types were developed from 44 coquina samples, in order to understand how pore size and shape contribute to permeability. Initially, the samples were separated by permeability ranges, while confirming their similarties through the T_2 curves. PCA statistics was applied to confirm which pore size partitions have the most influence on each cluster. Petrographic interpretation was also performed to identify geological factors that explain similarities among the groups of samples. As a complementary tool, XRD was used to classify and quantify the minerals contained in the rocks. The integration of all techniques helped to better understand the petrophysics and petrography of the samples.

A connectivity study was carried out in the development of this research. Based on the pore size distributions determined by NMR and the pore throats radius distributions provided by MICP, the surface relaxation was defined. This parameter is of great importance for transforming the relaxation times into pore radius, in order to assist the pore segmentation of the microCT images. From the pore segmentation, it was possible to transform the pore throats and pore bodies into tubes and spheres, respectively, a technique known as skeletonization. With this information modeling at the pore network level was performed and the permeability estimated, achieving good results. Based on this information, it was possible to understand how connectivity influences flow into the pore system. We could verify that samples with similar porosities but different permeabilities possess different interconnection of the pore system favors the flow within the pores.

The permeability was also estimated using NMR-based equations. The Kenyon and Timur-Coates equations are the most used in the literature to estimate this parameter in the field. This research aimed to determine the most suitable constants for the coquinas. Multiple linear regression (MLR) was used from the entire set of samples and also separated by rock type. As a result, the two models provided good results for the application, but the Kenyon model performed better for samples separated by rock type.

Normally, standard values for the constants are used by the oil industry, but this research could show that optimization of the constants through MLR improved the predictions, reaching values close to those of the laboratory.

Another point considered in this research was to verify how different techniques with their different results can contribute to a better understanding of complex rocks. The results obtained by routine core analysis are important once they provide a calibration for other techniques. NMR provides exceptionally good results for porosity and pore size distribution, in addition to have the versatility of its application during logging, making it possible to estimate the permeability of the reservoir "in situ". If measurements could be done in a well and in the laboratory, this would become the preferred method in petrophysics, but this is not always possible in the oil industry. MICP can provide the pore throat distribution obtained according to the boundary conditions imposed. The microCT images permit one to perform numerical simulations in order to determine porosity and permeability of a sample. In this case, the resolution will guide all the results to be obtained. The most powerful spect of microCT coupled with PNM techniques is its ability to carefully observe the pore system while the other tools provide more global values, without direct visualization.

Finally, we concluded that different available techniques are potentially important to obtain relevant information about a specific rock formation. Also, it was possible verify that in order to understand and to obtain good estimates of porosity and permeability, one needs to combine different techniques and extract the more reliable measurements. The integration of the various techniques and their results can improve our understanding of complex pore systems, giving better guidance for upscaling the petrophysics to fields conditions.

5.1 Further Studies

From the results and discussions presented along this work, some points are presented that could guide future research in order to improve knowledge in coquinas:

I. In the development of this work, important constants were determined to estimate permeability using NMR data. These constants were adequate for the set of samples used in this research, but it is still necessary to test their applicability in other samples;
II. The samples studied in this research were imaged with 14 μm of resolution. In general, this resolution iss considered adequate for most samples. However, in some

cases, it was not possible to visualize the sample connections, as these are made by subresolution pores. Therefore, new images with better resolution can contribute to identify unresolved pore throats and understand their contribution to flow in the pore system;

III. The *k* prediction results showed that the optimized constants did not agree with accepted literature values. Hence, their permeability values were not compatible with the experimental ones. Initially, one could assume that information about the pore distribution and porosity is enough to determine the permeability. However, additional studies of these samples can present interesting results, demonstrating that in addition to connectivity, other factors such as mean radius and throat constriction can impact the flow in highly heterogeneous samples such as carbonate rocks;

IV. The flow of fluid in a rocky interior is affected by porosity, permeability, tortuosity and the pore-size distribution of the rock (BEAR, 1972). These parameters are macroscopic consequences of the pore structure, which integrates geometry (pore size and shape, pore size distribution) and topology (pore connectivity) (DULLIEN, 1992). Sometimes, the topological factors are more important than the more well-known geometric factors (EWING and HORTON, 2002; HU *et al*., 2002; HUNT, 2004), especially when pore connectivity is low. However, the prevalence of low pore connectivity in rocks and their impact on the flow of fluids is poorly documented and understood, being a topic of great importance to be addressed in futher studies.

6 BIBLIOGRAPHY

AHMED, T. **Reservoir Engineering handbook**, 4th Ed. Burlington, MA: Gulf Professional Publishing. 2010

AHR, W. M. **Geology of Carbonate Reservoirs: The Identification, Description, and Characterization of Hydrocarbon in Carbonate Rocks**, First edition. Wiley, New Jersey, U.S.A., 2008.

AIRD, E. G. A. **Basic physics for medical imaging**. Butterworth-Heinemann. 1988.

AL-ANSI, N., GHARBI, O., RAEINI, A. Q., YANG, J., IGLAUER, S., BLUNT, M. J. "Influence of Micro-Computed Tomography Image Resolution on the Predictions of Petrophysical Properties". In: **International Petroleum Technology Conference 2013**, Beijing, China, 26–28 Março, 2013.

ALBERTS, L., BAKKE, S., BHATTAD, P., CARNERUP, A., KNACKSTEDT, M., ØREN, P., SOK, R., VARSLOT, T., YOUNG, B. "Characterization of Unconventional Reservoir Core at Multiple Scales". In: **Unconventional Resources Technology Conference**, Denver, Colorado – U.S.A., 12-14 agosto, 2013. SPE paper 168934 / URTeC paper 1619973.

ALBUQUERQUE, M. R., ELER, F. M., CAMARGO, H. V. R., COMPAN, A. L. M., CRUZ, D. A., PEDREIRA, C. E. 2018. "Estimation of Capillary Pressure Curves from Centrifuge Measurements Using Inverse Methods". In: **Rio Oil & Gas Expo and Conference**, Rio de Janeiro – Brasil, 24-27 setembro, 2018.

AL-RAOUSH, R. I., WILLSON, C. S. "A pore-scale investigation of a multiphase porous media system". In: **Journal of Contaminant Hydrology 77**, 67–89. Elsevier. 2005.

ALVES, R. A. B. R. **Desenvolvimento de um Algoritmo Computacional para Reconstrução da Microporosidade Utilizando a Técnica de Pore Network Model**. 79p. Monografia, Engenharia de Petróleo – Politécnica (POLI) – Universidade Federal do Rio de Janeiro.

ANDERSON, W.G.: "Wettability Literature Survey – Part 1: Rock/Oil/Brine Interactions and the Effects of Core Handling on Wettability", **Journal of Petroleum Technology 38**, pp. 1125–1144, Out. 1986.

ANP – Agência Nacional do Petróleo, Gás Natural e Biocombustíveis. 2018. **Anuário estatístico brasileiro do petróleo, gás natural e biocombustíveis: 2018**. Disponível em: <http://www.anp.gov.br/publicacoes/anuario-estatistico/anuario-estatistico-2018>. Access at November, 2018.

ARNS, C. H., A. SAKELLARIOU, T. J. SENDEN, A. P. SHEPPARD, R. SOK, W. V. PINCZEWSKI, M. A. KNACKSTEDT. "Digital core laboratory: Reservoir core analysis from 3D images". **Petrophysics 46(4)**: 260-277. 2005.

ARNS, C.H. “A comparison of pore size distributions derived by NMR and X-ray-CT techniques”. **Phys A 339**:159–165. 2004.

ARNS, J., ARNS, C. H., SHEPPARD, A. P., SOK, R. M., KNACKSTEDT, M. A., PINCZEWSKI, W. V. “Relative permeability from tomographic images; effect of correlated heterogeneity”. In: **Journal of Petroleum Science and Engineering**, 39, pp. 247 – 259. 2003.

AVIZO. **Reference Manual**. Version 9.5. January 2018.

AYACHIT, U. **The ParaView Guide: A Parallel Visualization Application**. Kitware. 2015.

AZAMBUJA, N.C.; ARIENTI, L.M. “Guidebook to the Rift-Drift Sergipe-Alagoas, Passive Margin Basin, Brazil”. **The 1998 American Association of Petroleum Geologists International Conference and Exhibition**. p.113, 1998.

AZZAM, M. I. S., DULLIEN, F. A. L. “Flow in tubes with periodic step changes in diameter: a numerical solution”. **Chem. Eng. Sci**. 32, 1445–1455. 1977.

BEAR, J. **Dynamics of Fluid in Porous Media**, Dover Publications inc., pp. 151–173. 1972.

BEHROOZMAND, A. A., KEATING, K., AUKEN, E. “A Review of the Principles and Applications of the NMR Technique for Near-Surface Characterization”. In: **Surv Geophys**, Elsevier, 2014. DOI 10.1007/s10712-014-9304-0

BELTRÃO, R. L. C., SOMBRA, C. L., LAGE, A. C. V. M., FAGUNDES NETTO, J. R., HENRIQUES, C. C. D. “Challenges and New Technologies for the Development of the Pre-Salt Cluster, Santos Basin, Brazil”. In: **2009 Offshore Technology Conference**, Houston, Texas – USA, 4-7 May, 2009. OTC Paper 19880.

BERNSEN J. ‘‘Dynamic limiaring of gray level images’’ **ICPR 86: Proc. Intl. Conf. Patt. Recog.**, pp. 1251–1255. 1986.

BIENIECKI, W., GRABOWSKI, S. “Multi-pass approach to adaptive limiaring based image segmentation”. In: **CADSM’2005**, 23-26 fevereiro, Lviv-Slavske, Ucrânia. 2005.

BIRD, R. B., STEWART, W. E., LIGHTFOOT, E. N. **Transport Phenomena**, John Wiley & Sons, New York. 1960.

BLUNT, M. J. “Flow in porous media — pore-network models and multiphase flow”. **Curr. Opin. Colloid Interface Sci**. 6, 197–207. 2001

BLUNT, M. J., JACKSON, M. D., PIRI, M., VALVATNE, P. H. “Detailed physics, predictive capabilities and macroscopic consequences for pore-network models of multiphase flow”. In: **Advances in Water Resources, 25**, 1069–1089. 2002.

BOGGS Jr., S. **Principles of Sedimentology and Stratigraphy**, Fourth edition. Pearson Prentice Hall, New Jersey, U.S.A., 2006.

BOHLING, G. C. **Introduction to Geostatistics**. Kansas Geological Survey Open File Report no 26 (2007), 50. 2007.

BROWN, R.J.S., FATT, I.: "Measurements of Fractional Wettability of Oilfield Rocks by the Nuclear Magnetic Relaxation Method", **Transactions, AIME 207**: 262–264, 1956.

BUADES, A., COLL, B., MOREL, J. M. A non local algorithm for image denoising, in Proc. **Int. Conf. Computer Vision and Pattern Recognition** (CVPR) 2005, vol. 2, pp. 60-65. 2005.

BULTREYS, T., DE BOEVER, W., CNUDDE, V. "Imaging and image-based fluid transport modeling at the pore scale geological materials: A practical introduction to the current state-of-the-art". **Earth-Science Reviews** 155: 93-128. 2016.

BULTREYS, T., BOONE, M. A., BOONE, M. N., DE SCHRYVER, T., MASCHAELLE, B., VAN HOOREBEKE, L., CNUDDE, V. "Fast laboratory-based micro-computed tomography for pore-scale research: Illustrative experiments and perspectives on the future". **Advances in Water Resources** 95: 341–351. 2015.

BUSH, J. W. M. Surface Tension Module. Department of mathematics, Massachusetts Institute of Technology – MIT. Notas de aula. www.web.nit.edu. Accessed at May 2017.

BUTT, H. J.; GRAF, K.; KAPPL, M. 2006. **Physics and Chemistry of Interfaces**. Berlin, Germany: WILEY-VCH Verlag GmbH & Co.

CÂMARA, R. N. 2013. **Caracterização Petrofísica de Coquinas da Formação Morro do Chaves (Barremiano/Aptiano), Intervalo Pré-sal da Bacia de Sergipe-Alagoas**. Dissertação de Mestrado, Programa de Pós-graduação em Geologia /UFRJ, Rio de Janeiro, Brasil.

CARBONELL, R. G., WHITAKER, S. Heat and Mass Transfer in Porous Media**. Fundamentals of Transport Phenomena in Porous Media**. Martinus Nijhoff Publishers, 1984.

CARMINATTI, M., DIAS, J. L., WOLFF, B. "From Turbidites to Carbonates: Breaking Paradigms in Deep Waters". In: **2009 Offshore Technology Conference**, Houston, Texas – USA, 4-7 May, OTC Paper 20124.

CHAN, T. F., VESE, L. A. "Active Contours Without Edges". In: **IEEE Transactions on Image Processing, Vol. 10, No. 2**. 2001.

CNUDDE, V., BOONE, M. N. "High-resolution X-ray computed tomography in geosciences: A review of the current technology and applications". In: **Earth-Science Reviews 123 (2013)**: 1–17. Elsevier. 2013.

CNUDDE, V., MASSCHAELE, B., DIERICK, M., VLASSENVROECK, J., HOOREBEKE, L.V., JACOBS, P. “Recent progress in X-ray CT as a geosciences tool”. In: **Applied Geochemistry**, 21: 826-832, 2006.

COATES, G.R., XIAO. L., PRAMMER, G. **NMR logging principles and applications**. Halliburton Energy Services, Houston. 1999.

COENEN, J., TCHOUPAROVA, E., JING, X. “Measurement Parameters and Resolution Aspects of Micro X-ray Tomogrraphy for Advanced Core Analysis”. In: **International Symposium of Society of Core Analysts**, Abu Dhabi, UAE. 2004.

CONSTANTINIDES, G.N., PAYATAKES, A.C. Network simulation of steady-state two-phase flow in consolidated porous media. **AIChE J**. 42, 369–382. 1996.

CORBETT, P. W. M. **Integration of static and dynamic models. Petroleum geoengineering**. SEG/EAGE Distinguished Instructor Series, vol. 12, pp. 100–190. 2009.

CORBETT, P. W. M., ANGGRAENI, S., BOWDEN, D. “The use of the probe permeameter in carbonates-addressing the problems of permeability support and stationarity”. In: **Log Anal. 40 (5)**, 316–326. 1999.

CORBETT, P. W. M., BORGHI, L. “Lacustrine Carbonates – for the purpose of reservoir characterisation are they different?”. In: **2013 Offshore Technology Conference Brasil**, Rio de Janeiro – Brazil, 29-31 October, 2013. OTC Paper 24482.

CRAIG, F.F. JR.: The Reservoir Engineering Aspects of Waterflooding, **Monograph series, SPE**, Richardson, TX, 1971.

DE VRIES, E. T., RAOOF, A., VAN GENUCHTEN, M. T. “Multiscale modelling of dual-porosity media: a computational pore-scale study flow and solute transport”. **Advances in Water Resources** 105: 82-95. 2017.

DEDAVID, B. A., GOMES, C. I., MACHADO, G. **Microscopia Eletrônica de Varredura: Aplicações e preparação de amostras: materiais poliméricos, metálicos e semicondutores**. Porto Alegre, RS. EDIPUCRS, 2007.

DEUTSCH, C. V. **Geostatistical reservoir modeling**. Oxford University Press. 2002.

DIGGLE, P. J. and RIBEIRO JR, P. J. **Model-based Geostatistics**. New York: Springer. 2007.

DONALDSON, E. C., ALAM, W. **Wettability**. Houston, TX: Gulf Publishing Company. 2008

DOS SANTOS, E., AYRES, H., PEREIRA, A., MACHÍN, J., TRITLLÁ, J., LEITE, K., SILVA, E. “Santos Microbial Carbonate Reservoirs: A Challenge”. In: **2013 Offshore Technology Conference Brasil**, Rio de Janeiro – Brazil, 29-31 October, 2013. OTC Paper 24446.

DREXLER, S**. Study of the fluid-fluid and rock-fluid interactions: Impact of dissolved CO_2 on interfacial tension and wettability for the Brazilian Pre-salt scenario**. 2018. 234f. Tese de doutorado, Programa de Pós- Graduação em Engenharia Civil – COPPE, Universidade Federal do Rio de Janeiro – UFRJ. Rio de Janeiro, RJ – Brasil.

DREXLER, S., SOUZA, F. P., CORREIA, E. L., SILVEIRA, T. M. G., COUTO, P. 2018. Statistical Analysis to Evaluate the key Parameters Affecting Wettability of a Brazilian Pre-Salt Crude and Brine on Different Mineral Rocks. **Rio Oil & Gas Conference 2018**. Rio de Janeiro, Brazil: IBP.

DUNN, K. J., BERGMAN, D. J., LATORRACA, G. A. **Nuclear magnetic resonance—petrophysical and logging applications**. Elsevier, Amsterdam. 2002a.

DUNN, K. J., BERGMAN, D. J., LATORRACA, G. A. **Nuclear magnetic resonance—petrophysical and logging applications**. Elsevier Science, Kidligton, pp 1–30. 2002b.

DUNSMUIR, J. H., FERGUSON, S. R., D'AMICO, K. L., STOKES, J. P. "X-ray Microtomography: a New Tool for the Characterization of Porous Media". In **SPE Annual Technical Conference and Exhibition**, 1991.

ENGELHARDT, M., BAUMANN, J. "Determination of size and intensity distribution of the focal spot of a microfocus X-ray tube using image processing". In: **Proc. ECNDT 2006**, Th 2.5.4., pp 1-13, Berlin, Set 2006.

ESTRELLA, R. R. 2015. **Variação da Porosidade e da Permeabilidade em Coquinas da Formação Morro do Chaves (Andar Jiquiá), Bacia Sergipe-Alagoas**. 84p. Monografia, Geologia – Instituto de Geologia (IGEO) – Universidade Federal do Rio de Janeiro.

FACANHA, J. M. F. 2017. **Fundamentals of Wettability Applied to Brazilian Pre-Salt Reservoirs and Wettability Alteration Evaluation in Low Salinity Water Injection**. [s.l.] Heriot-Watt University. Edinburgh – UK.

FAERSTEIN, M. **Impactos da Molhabilidade da Rocha na Produção e Recuperação de Petróleo**. 2010. 190f. Dissertação de mestrado, Programa de Pós-Graduação em Engenharia Civil – COPPE, Universidade Federal do Rio de Janeiro – UFRJ. Rio de Janeiro, RJ – Brasil.

FATT, I. "The network model of porous media". **Transactions of the American Institute of Mining Metallurgical Petroleum Engineers** 207,144–181. 1956.

FÄY-GOMORD, O., SOETE, J., DAVY, C. A., JANSSENS N., TROADEC, D., CAZAUX, F., CALINE, B., SWENNEN, R. "Tight chalk: Characterization of the 3D pore network by FIB-SEM, towards the understanding of fluid transport". **Journal of Petroleum Science and Engineering 156**: 67-74. 2017.

FEIJÓ, F.J.; PEREIRA, M.J. Bacia de Santos. **Boletim de Geociências da Petrobrás**, Rio de Janeiro, v.8, n.1, p.219-234, 1994.

FERNANDES J. S., APPOLONI C. R., MOREIRA A. C., FERNANDES C. P. "Porosity and pore size distribution determination of tumblagooda formation sandstone by X-Ray Microtomography". In: **International Nuclear Atlantic Conference INAC 2007**. 2007.

FERNANDES, J. S., APPOLONI, C. R., MARQUES, L. C., FERNANDES, C. P. "Microstructure Parameters Evaluation of Botucatu Formation Sandstone By X-Ray Microtomography". In: **2009 International Nuclear Atlantic Conference - INAC 2009**, Rio de Janeiro, Brasil, 27 setembro – 02 outubro, 2009.

FIORELLI, G. L. **Caracterização de coquinas e dolomitos integrando três metodologias distintas: resistividade elétrica, ressonância magnética nuclear (RMN) e porosimetria por intrusão de mercúrio (MICP)**. 2015 129f. Dissertação de Mestrado, Faculdade de Engenharia Mecânica e Instituto de Geociências da Universidade Estadual de Campinas.

FORBES, P. 1994. Simple and Accurate Methods for Converting Centrifuge Data Into Drainage and Imbibition Capillary Pressure Curves. **The Log Analyst**.

FORMIGLI, J. M., PINTO, A. C. C., ALMEIDA, A. S. "Santos Basin's Pre-Salt Reservoirs Development – The Way Ahead". In: **2009 Offshore Technology Conference**, Houston, Texas – USA, 4-7 May, OTC Paper 19953.

GHARAHBAGH, A. E., FAKHIMI, A. "Numerical Determination of Representative Volume Element of Rock". In: **44th US Rock Mechanics Symposium and 5th U.S.-Canada Rock Mechanics Symposium**, Salt Lake City, UT – U.S.A. Junho 27–30, 2010. ARMA paper 10-131. 2010.

GLOTIN, G.; GENET, J.; KLEIN, P. 1990. "Computation of Drainage and Imbibition Capillary Pressure Curves from Centrifuge Experiments". **Proceedings of SPE Annual Technical Conference and Exhibition**.

GOMES, O. F. M. **Microscopia co-localizada: novas possibilidades na caracterização de minérios**. 2007. 105f. Tese de Doutorado. Pontifícia Universidade Católica do Rio de Janeiro.

HAMAMMATSU PHOTONICS. "**130 kV Microfocus X-RaySource L9181-2**". Iwata, Japão: 2012a, pp 1-4.

HASSLER, G. L., BRUNNER, E. 1945. Measurement of Capillary Pressures in Small Core Samples. **Petroleum Transactions of AIME**, v. 160, n. 1, p. 114–123.

HAYASHI. F. Y. D., 2014. **Avaliação do Volume Representativo Elementar (REV) em estromatólito de Lagoa Salgada**. Trabalho Final de Curso. Geologia/UFRJ. Rio de Janeiro, RJ – Brasil.

HOERLLE, F. O. 2018. **Estudo da Heterogeneidade, Anisotropia e Conectividade do Sistema Poroso das Coquinas da Formação Morro do Chaves (Bacia de Sergipe-Alagoas)**. Dissertação de Mestrado, COPPE/UFRJ, Rio de Janeiro, Brasil.

HOERLLE, F. O. L., RIOS, E. H., SILVA, W. G. A. L., PONTEDEIRO, E. M. B. D., LIMA, M. C. O., CORBETT, P. W. M., ALVES, J. L. D., COUTO, P. "Nuclear Magnetic Resonance to Characterize the Pore System of Coquinas from Morro do Chaves Formation, Sergipe-Alagoas Basin, Brazil.". **Brazilian Journal of Geophysics**. 36 (3): 1-8. 2018.

HOORFAR, M.; KURZ, M. A.; NEUMANN, A. W. 2005. Evaluation of the surface tension measurement of axisymmetric drop shape analysis (ADSA) using a shape parameter. **Colloids and Surfaces A: Physicochemical and Engineering Aspects**, v. 260, n. 1–3, p. 277–285.

HORNAPOUR, M., KOEDERITZ, L., HARVERY, A. H. **Relative Permeabilities of Petroleum Reservoirs**. Boca Raton, FL: CRC Press, Inc. 1990

HOUSTON, A. N., SCHMIDT, S., TARQUIS, A. M., OTTEN, W., BAVEYE, P. C., HAPCA, S. M. "Effect of scanning and image reconstruction settings in X-ray computed microtomography on quality and segmentation of 3D soil images". In: **Geoderma 207-208**: 154-165. Elsevier. 2013.

HUTTON, D. **Fundamentals of Finite Element Analysis**, New York: McGraw-Hill. 2004.

IZZO JR., J., JOSHI, A., GREW, K., CHIU, W., TKACHUK A., WANG, S., YUN, W. "Nondestructive Reconstruction and Analysis of SOFC Anodes Using X-ray Computed. Tomography at Sub-50 nm Resolution". In: J. **Electrochem. Soc. 155 (5)**, pp. B504-B508. 2008.

JOEKAR-NIASAR, V. **The Immiscibles Capillarity Effects in Porous Media: Pore-Network Modelling**. Utrecht University – Geosciences Faculty – Earth Sciences Department. 2010.

JOEKAR-NIASAR, V., HASSANIZADEH, S. J. "Effects of fluids properties on non-equilibrium capillarity effects: dynamic pore-network modeling". **International Journal of Multiphase Flow** 37: 198-214. 2011.

JOHNSON, C. **Numerical Solutions of Partial Differential Equations by the Finite Element method**, Cambridge University Press. 1987.

JONES, C. M., CHAVES, H. A. F. "Assessment of Yet-To-Find Oil in the Brazilian Pre-Salt Region". In: **2011 Brasil Offshore Conference**, Macaé – Brazil, 14-17 June. SPE paper 143911.

KACZMARCZYK, J., DOHNALIK, M., ZALEWSKA, J, CNUDDE, V. "The interpretation of X-ray Computed Microtomography images of rocks as an application of volume image processing and analysis". In: **WSCG 2010 Communication papers**. 2010.

KACZMARCZYK, J., DOHNALIK, M., ZALEWSKA, J. “Three-dimensional Pore Scale Fluid Flow Simulation Based on Computed Microtomography Carbonate Rocks’ Images”. In: **V European Conference on Computational Fluid Dynamic**, ECCOMAS CFD 2010, 14-17 junho, 2010.

KANIT, T., FOREST, S., GALLIET, I., MOUNOURY, V., JEULIN, D. “Determination of the size of the representative volume element for random composites: statistical and numerical approach”. In: **International Journal of Solids and Structures, Volume 40, Issues 13–14**, 3647–3679, Junho/Julho. 2003.

KEEHM, Y., MUKERJI, T. “Permeability and Relative Permeability from Digital Rocks: Issues on Grid Resolution and Representative Elementary Volume”. In: **SEG Int'l Exposition and 74th Annual Meeting**, Denver, Colorado – U.S.A. 10-15 October. 2004.

KITTLER, J., ILLINGWORTH, J. “Minimum Error Thresholding” In: **Pattern Recognition, Vol.19, No.1**, pp. 41-47, Great Britain. 1986.

KNACKSTEDT, M., GOLAB, A., RIEPE, L. “Petrophysical characterization of unconventional reservoir core at multiple scales”. In: **SPWLA 53rd Annual Logging Symposium**. Cartagena, Colômbia, 16-20 junho, 2012.

LEACH, R. O., WAGNER, O. R., WOOD, H. W., HARPLE, C. F. A laboratory study and field study of wettability adjustment in waterflooding. **Journal of Petroleum Technology, 14 (2)**, 206 – 212. SPE Paper 119-PA. 1962.

LEVITT, M. H. **Spin dynamics: basics of nuclear magnetic resonance**. Wiley, Chichester. 2006.

LINDQUIST, W., VENKATARANGAN, A., DUNSMUIR, J., WONG, T. 2000. Pore and throat size distributions measured from synchrotron x-ray tomographic images of fontainebleau sandstones. Journal of Geophysical Research – All Series – 105 (B9), 21. 2000.

LINDQUIST, W. B., VENKATARANGAN, A. “Investigating 3D geometry of porous media from high resolution images”. **Phys. Chem. Earth Solid Earth Geod**. 24, 593–599. 1999.

LINDQUIST, W. B., LEE, S., COKER, D. A., JONES, K. W., SPANNE, P. “Medial axis analysis of void structure in three-dimensional tomographic images of porous media”. **J. Geophys. Res.** 101, 8297. 1996.

LIU, J., PEREIRA, G. G., LIU, Q., LIEB-REGENAUER, K. “Computational challenges in the analyses of petrophysics using microtomography and upscaling: A review”. **Computers & Geosciences** 89, pp. 107-117, 2016.

LIU, J., PEREIRA, G. G., LIEB-REGENAUER, K. “From characterisation of pore-structures to simulations of pore-scale fluid flow and the upscaling of permeability using microtomography: A case study of heterogeneous carbonates”. In: **Journal of Geochemical Exploration 144**, pp. 84-96, 2014.

LIU, Y., HARDING, A., ABRIEL, W., STREBELLE, S. “Multiple-point simulation integrating wells, three-dimensional seismic data, and geology”. **AAPG bulletin**. 88 (7), 905–921. 2004.

LØNØY A. Making sense of carbonate pore systems. **AAPG bulletin**, 90(9): 1381–1405. 2006.

LUCIA, F. J. **Carbonate reservoir characterization: an integrated approach**. Springer Science & Business Media, 2007.

LUNA, J. L., PEROSI, F. A., RIBEIRO, M. G. S., SOUZA, A, BOYD, A., BORGHI, L. F., CORBETT, P. W. M. “Petrophysical Rock Typing of Coquinas from the Morro do Chaves Formation, Sergipe-Alagoas Basin (northeast brazil)”. **Brazilian Journal of Geophysics**. 34 (4). 2016.

ŁYDŻBA, D., RÓŻAŃSK, A. “On the minimum size of Representative Volume Element: An n-point probability approach”. In: **Harmonising Rock Engineering and the Environment – Qian & Zhou (eds)**, Taylor & Francis Group, London, ISBN 978-0-415-80444-8. 2012.

MA, S., MASON, G., MORROW, N. R. “Effect of contact angle on drainage and imbibition in regular polygonal tubes”. **Colloids Surfaces A** 117, 273–291. 1996.

MALISKA, A. M. **Microscopia Eletrônica de Varredura**. Notas de Aula. Universidade Federal de Santa Catarina – UFSC. 2013.

MALVERN, L. E. **Introduction to the Mechanics of a Continuous Media**, Prentice-Hall. 1969.

MARLE, C. M. “On macroscopic equations governing multiphase ow with dffusion and chemical reactions in porous media”**. Int. J. Engng. Sci**., 50: 643-662, 1982.

MEES, F., SWENNEN, R., GEET, M.V., JACOBS, P. “Aplications of x-ray computed tomography in geosciences”. In: **Geological Society Special Publications**, London, pp1-6, 2003.

MELLO, M. R., BENDER, A. A., AZAMBUJA FILHO, N. C., DE MIO, E. “Giant Sub-Salt Hydrocarbon Province of the Greater Campos Basin, Brazil”. In: **2011 Offshore Technology Conference Brasil**, Rio de Janeiro – Brazil, 4-6 October, 2011. OTC Paper 22818.

MUMFORD D., SHAH J. “Optimal approximation by piecewise smooth functions and associated variational problems”. In: **Commun. Pure Appl. Math, vol. 42**, pp. 577–685. 1989.

NARSILIO, G., BUZZI, O., FITYUS, S., YUN, T. S., SMITH, D. W. “Upscaling of Navier–Stokes equations in porous media: Theoretical, numerical and experimental approach”. In: **Computers and Geotechnics 36**, 7: 1200–1206. Elsevier. 2009.

NETO, J. M. R., FIORI, A. P., LOPES, A. P., MARCHESE, C., PINTO-COELHO, C. V., VASCONCELLOS, E. M. G., SILVA, G. F., SECCHI, R. “A microtomografia computadorizada de raios x integrada à petrografia no estudo tridimensional de porosidade em rochas”. In: **Revista Brasileira de Geociências 41 (3)**: 498-508, Setembro, 2011.

NIBLACK W. **An Introduction to Image Processing**. Prentice-Hall, Englewood Cliffs, NJ – U.S.A. pp. 115–116. 1986.

NORDAHL, K., RINGROSE, P. S. “Identifying the Representative Elementary Volume for Permeability in Heterolithic Deposits Using Numerical Rock Models”. In: **Math Geosci 40**: 753–771. International Association for Mathematical Geology. 2008.

OKABE, H., BLUNT, M. J. “Pore space reconstruction of vuggy carbonates using microtomography and multiple-point statistics”. In: **Water Resources Research, Vol. 43**, W12S02. 2007.

OKABE, H., BLUNT, M. J. “Pore space reconstruction using multiple-point statistics”. In: **Journal of Petroleum Science and Engineering, 46**, 121–137. 2005.

OKABE, H., BLUNT, M. J. “Prediction of permeability for porous media reconstructed using multiple-point statistics”. In: **Phys. Rev. E., 70, 066135**. 2004.

OKASHA, T.M., FUNK, J.J., Al-RASHIDI, H.N.: “Fifty Years of Wettability Measurements in the Arab-D Carbonate Reservoir”, SPE 105114, **15th SPE Middle East Oil & Gas Show and Conference**, Bahrain, Mar. 2007.

OLI Studio. **A Guide to Use OLI Studio**. Version 9.6. 2018.

OLIVEIRA R., PEPIN, A. H., CARVALHO, M. S. “Estimation for Representative Element Area of a Coquinas Analogue Using Statistical and Numerical Methods”. In: **SPE Latin American and Caribbean Petroleum Engineering Conference**, Maracaibo, Venezuela, 21-23 Maio. 2014.

OREN, P., BAKKE, S., ARNTZEN, O. “Extending predictive capabilities to network models”. **SPE Journal** 3 (4): 324–336. 1998.

OTSU, N. ‘‘A Limiar Selection Method from Gray-Level Histograms”. In: **IEEE Transactions on Systems, Man, and Cybernetics**, SMC-9, 62–66. 1979.

PADGETT, R., KOTRE, C. J. “Assessment of the effects of pixel loss on image quality in direct digital radiography”. **Physics in Medicine and Biology**, v. 49, pp 977-986. 2004.

PETERS, E. J. **Advanced Petrophysics: Dispersion, interfacial phenomena, wettability, capillarity, capillary pressure, relative permeability**. Live Oak. 2012.

PÉNELOUX, A.; RAUZY, E.; FRÉZE, R. 1982. A consistent correction for Redlich-Kwong-Soave volumes. **Fluid Phase Equilibria**, v. 8, n. 1, p. 7–23, januray.

PINHEIRO, R.S., SANTOS, A. R, MARQUES, M., SCHNITZLER, E., SIGNORINI, D., TOMITA, R. A. "Well Construction Challenges In The Pre-Salt Development Projects". In: **2015 Offshore Technology Conference**, Houston, Texas – USA, 4-7 May, OTC Paper 25888.

PIZARRO, J. O. S., BRANCO, C. C. M. "Challenges in Implementing an EOR Project in the Pre-Salt Province in Deep Offshore Brasil" In: **2012 SPE EOR Conference at Oil and Gas West Asia**, Muscat – Oman, 16-18 April. 2012. SPE paper 155665.

RADKE, C.J., KOVSCEK, A.R., WONG, H.: "A Pore-Level Scenario for the Development of Mixed Wettability in Oil Reservoirs", **American Institute of Chemical Engineers Journal 39**, 6: 1072–1085, Jun. 1993.

RAMIASA, M., RALSTON, J., FETZER, R., SEDEV, R. "The influence of topography on dynamic wetting". **Advances in Colloid and Interface Science**, v.206, p. 275-293. 2014.

RANSOHOFF, T.C., RADKE, C.J. "Laminar flow of a wetting liquid along the corners of a predominantly gas-occupied noncircular pore". **J. Colloid Interface Sci**. 121, 392–401. 1988.

RAOOF, A. **Reactive/Adsorptive Transport in (Partially-) Saturated Porous Media: from pore scale to core scale**. Utrecht University – Geosciences Faculty – Earth Sciences Department. 2011.

RAOOF, A., HASSANIZADEH, S. M. "A new method for generating pore-network models of porous media". **Transport in Porous Media** 81 (3), 391–407. 2009.

RAOOF, A., NICK, H. M., HASSANIZADEH, S. M., SPIERS, C. J. "PoreFlow: A complex pore-network model for simulation of reactive transport in variably saturated porous media". **Computers & Geosciences** 61: 160-174. 2013.

RAZA, S.H., TREIBER, L.E., ARCHER, D.L.: "Wettability of Reservoir Rocks and its Evaluation", **Prod. Monthly 32**, No. 4, 2-7, Abr. 1968.

REKTORYS, K. **Variational Methods in Mathematics, Science and Engineering**, D. Reidel Publishing Company. 1977.

RIDLER, T. W., CALVARD, S. "Picture Limiaring Using an Iterative Selection Method". In: **IEEE Transactions on Systems, Man, and Cybernetics, Vol. sMC-8, No. 8**. 1978.

ROSA, A. J., CARVALHO, R. S., XAVIER, J. A. D. **Engenharia de Reservatórios de Petróleo**. Editora Interciência Ltda., Rio de Janeiro, RJ, Brasil, 2006.

RUDIN, W. **Principles of Mathematical Analysis**, McGraw-Hill. 1976.

SALATHIEL, R. A. Oil Recovery by Surface Film Drainage in Mixed-Wettability Rocks. **Journal of Petroleum Technology**, 25 (10), 1216 – 1224. SPE Paper 4104-PA. 1973.

SCANIP, +FE, +NURBS and +CAD. **Reference Guide**. Version 6.0. 2013. Simpleware Ltd. http://www.simpleware.com

SCHOLLE, P. A., ULMER-SCHOLLE, D. S. "A Color Guide to the Petrography of Carbonate Rocks: Grains, textures, porosity, diagenesis". **American Association of Petroleum Geologists Memoir 77**, 474 p. 2003.

SCHÄFER, W. **Ecology and Paleoecology of Marine Environments**. Chicago: The University of Chicago Press, 568p, 1972.

SEEVERS, D.O. "A nuclear magnetic method for determining the permeability of sandstones". In **33rd annual logging symposium**, society of professional well log analysts, transactions, paper L. 1966.

SEGERLIND, L. J. **Aplied Finite Element Analysis**, New York: John Wiley. 1984.
SELLEY, R. C. **Applied Sedimentology**, Second edition. Academic Press, California, U.S.A. 1984.

SERVIDONI, A. P. S. 2012. **Análise de Porosidade e o Potencial como Rocha Reservatório em Estromatólito do Recente da Lagoa Salgada, Litoral Fluminense – RJ** / Dissertação de Mestrado, Programa de Pós Graduação em Geologia, Setor de Ciências da Terra – UFPR. Curitiba, PR – Brasil.

SEZGIN, M., SANKUR, B. "Survey over image limiaring techniques and quantitative performance evaluation". In: **Journal of Electronic Imaging 13(1)**, 146–165. 2004.

SHEPPARD, A., LATHAM, S., MIDDLETON, J., KINGSTON, A., MYERS, G., VARSLOT, T., FOGDEN, A., SAWKINS, T., CRUIKSHANK, R., SAADATFAR, M., FRANCOIS, N., ARNS, C., SENDEN, T. "Techniques in helical scanning, dynamic imaging and image segmentation for improved quantitative analysis with X-ray micro-CT". In: **Nuclear Instruments and Methods in Physics Research B**. Elsevier, 2014. http://dx.doi.org/10.1016/j.nimb.2013.08.072

SILVA, P.N., GONÇALVES, E.C., RIOS, E.H., MUHAMMAD, A., MOSS, A., PRITCHARD, T., GLASSBORROW, B., PLASTINO, A. 2015. **Atomatic classification of carbonate rocks permeability from ^{1}H NMR relaxation data**. Expert Systems with Applications. http://dx.doi.org/10.1016/j.eswa.2015.01.034

SILVEIRA FILHO, O. T. 2003. **Dispersão Térmica em Meios Porosos Periódicos. Um Estudo Numérico**. 2003. 152f. Tese de doutorado, Modelagem Computacional, Universidade do Estado do Rio de Janeiro – UERJ, Rio de Janeiro.

SOARES, A. P. J. 2016. **Influência da molhabilidade da rocha na recuperação de petróleo de reservatórios carbonáticos**. 131f. Tese de doutorado, Programa de Pós-Graduação em Engenharia Química, Universidade Federal do Rio Grande do Norte – UFRN. Natal, RN – Brasil.

SOUZA, A., CARNEIRO, G., ZIELINSKI, L., POLINSKI, R., SCHWARTZ, L., H¨URLIMANN, M. D., BOYD, A., RIOS, E. H., SANTOS B. C. C., TREVIZAN W. A., MACHADO, V. F., AZEREDO, R. B. V. Permeability Prediction Improvement using 2D NMR Diffusion-T2 Maps. **SPWLA 54th Annual Logging Symposium**, New Orleans, Louisiana, June 22-26. 2013.

STRALEY, C., ROSSINI, D., VINEGAR, H., TUTUNJIAN, P., MORRISS, C. "Core analysis by low-field NMR". **Log Anal 38**:84–93. 1997.

STROEVEN, M., ASKES H., SLUYS L.J. "Numerical determination of representative volumes for granular materials". In: **Comput. Methods Appl. Mech. Engrg. 193**, 3221-3238. 2004.

TAVARES, A. C. G. **Fácies diagenéticas em coquinas da Formação Morro do Chaves (Barremiano-Aptiano, Bacia de Sergipe-Alagoas)**. 2014. 192f. Dissertação (Mestrado em Geologia) - Programa de Pós-graduação em Geologia, Instituto de Geociências, Universidade Federal do Rio de Janeiro, Rio de Janeiro.

TELES, A. P. **Aplicação da Microtomografia Computadorizada de Raios X por Dupla-Energia na Caracterização de Materiais Porosos.** 2016. 113f. Tese de Doutorado, Programa de Pós-Graduação em Engenharia Nuclear – COPPE/UFRJ. Rio de Janeiro, RJ – Brasil.

TIMUR, A. "Producible porosity and permeability of sandstones investigated through nuclear magnetic resonance principles". **Long Anal** 10:3-11. 1969.

THOMPSON, K.E. "Pore-scale modeling of fluid transport in disordered fibrous materials". **AIChE J.** 48, 1369–1389. 2002.

TOUATI, M., SUICMEZ, S., FUNK, J., CINAR, Y., KNACKSTEDT, M. "Pore Network Modeling of Saudi Aramco Rocks: A Comparative Study". **Society of Petroleum Engineers**. 2009.

TREIBER, L.E., ARCHER, D.L., OWENS. W. W.: "Laboratory Evaluation of the Wettability of Fifty Oil-Producing Reservoirs", **SPEJ**, 12, 531-40, Dez. 1971.

VIK, B., BASTESEN, E., SKAUGE, A. "Evaluation of representative elementary volume for a vuggy carbonate rock – Part I: Porosity, permeability, and dispersivity". In: **Journal of Petroleum Science and Engineering**, 112, pp. 36-47, 2013.

VIK, B., BASTESEN, E., SKAUGE, A. “Evaluation of representative elementary volume for a vuggy carbonate rock – Part II: Two-phase flow”. In: **Journal of Petroleum Science and Engineering**, 112, pp. 48-60, 2013.

VIK, B., DJURHUUS, K., SPILDO, K., SKAUGE, A. “Characterisation of Vuggy Carbonates”. In: **2007 SPE/EAGE Reservoir Characterization and Simulation**, Abu Dhabi, U.A.E., 28–31 October, 2007. SPE paper 111434.

VILCÁEZ, J., MORAD, S., SHIKAZONO, N. “Pore-scale simulation of transport properties of carbonates rocks using FIB-SEM 3D microstructure: Implications for field scale solute transport simulations”. **Journal of Natural Gas and Engineering 42**, 13-22. 2017.

VIRGONE, A., BROUCKE, O., HELD, A., LOPEZ, B., SEARD, C., CAMOIN, G., SWENNEN, R., FOUBERT, A., ROUCHY, J., PABIAN-GOYHENECHE, C., GUO, L. “Continental Carbonates Reservoirs: The Importance of Analogues to Understand Presalt Discoveries”. In: **2013 International Petroleum Technology Conference**, Beijing – China, 26-28 March. IPTC paper 17013.

WITHJACK, E. M. “Computed Tomography for Rock-Property Determination and Fluid-Flow Visualization”. In: **SPE Formation Evaluation**, pp: 606-704, Dezembro, 1988. Paper original SPE 16951.

WILDENSCHILD, D., VAZ, C. M. P., RIVERS, M. L., RIKARD, D., CHRISTENSEN, B. S. B. “Using X-ray Computed Tomography in Hydrology: Systems, Resolutions, and Limitations”. In: **Journal of Hydrology 267(3)**: 285-297. 2002.

XIONG, Q., BAYCHEV, T. G., JIVKOV, A. P. “Review of pore network modelling of porous media: Experimental characterisations, network constructions and applications to reactive transport”. **Journal of Contaminant Hydrology** 192: 101-117. 2016.

YEONG, C. L. Y., TORQUATO, S. “Reconstructing random media”. In: **Phys. Rev. E., 57**, 495–506. 1998a.

YEONG, C. L. Y., TORQUATO, S. “Reconstructing random media. II. Three-dimensional media from two-dimensional cuts”. In: **Phys. Rev. E., 58**, 224–233. 1998b.

YAKHSHI-TAFTI, E.; KUMAR, R.; CHO, H. J. 2011. Measurement of Surface Interfacial Tension as a Function of Temperature Using Pendant Drop Images. **International Journal of Optomechatronics**, v. 5, n. 4, p. 393–403.

YIN, S., DE VRIES, E. T., RAOOF, A. Computational codes for solute transport in porous media. **Class notes**. Utrecht University – The Netherlands. May, 2017.

YOUSSEF, S., ROSENBERG, E., GLAND, N., KENTER, J. A. M., SKALINSKI, M., VIZIKA, O. “High Resolution CT and Pore-Network Models to Assess Petrophysical Properties of Homogeneous and Heterogeneous Carbonates”. In: **2007 SPE/EAGE Reservoir Characterization and Simulation Conference**, Abu Dhabi, UAE, 28-31 outubro, 2007.SPE paper 111427.

ZHAO, H. Q., MACDONALD, I. F., KWIECIEN, M. J. “Multi-orientation scanning: a necessity in the identification of pore necks in porous media by 3-D computer reconstruction from serial section data”. **J. Colloid Interface Sci**. 162, 390–401. 1994.

ZHOU, D., BLUNT, M. J., ORR, F. M. “Hydrocarbon drainage along corners of noncircular capillaries”. **J. Colloid Interface Sci**. 187, 11–21. 1997.

ZHOU, D., DILLARD L. A., BLUNT M. J. “A physically based model of dissolution of nonaqueous phase liquids in the saturated zone”. **Transp. Porous Media**, 39(2), 227–255. 2000.